HÁSKÓLINN Í REYKJAVÍK
REYKJAVIK UNIVERSITY

Molecular Dynamics and Sensing with Low-Cost Organic-Inorganic Nanostructures

Rachel Elizabeth Brophy

Thesis of 180 ECTS credits submitted to the Department of Applied Science at Reykjavík University in partial fulfillment of the requirements for the degree of Doctor of Applied Science-Material Science

21 November 2024

Thesis Committee:

Andrei Manolescu, Supervisor
Professor, Reykjavík University, Iceland

Halldór Guðfinnur Svavarsson, Co-Supervisor
Professor, Reykjavík University, Iceland

Muhammad Taha Sultan, Committee member
Research Specialist, Reykjavík University, Iceland

George Alexandru Nemnes, committee member
Professor, University of Bucharest, Romania

István Csarnovics, Examiner
Professor, University of Debrecen, Hungary

ISSN 978-9935-539-49-6
ISBN 978-9935-539-48-9 Copyright © 2025 Rachel Elizabeth Brophy

This work is licensed under the Creative Commons Attribution-NonCommercial-NoDerivatives 4.0 International License (`http://creativecommons.org/licenses/by-nc-nd/4.0/`). You may copy and redistribute the material in any medium or format, provide appropriate credit, link to the license and indicate what changes you made. You may do so in any reasonable manner, but not in any way that suggests the licensor endorses you or your use. You may not use the material for commercial purposes. If you remix, transform or build upon the material, you may not distribute the modified material. The images or other third party material in this thesis are included in the book's Creative Commons license, unless indicated otherwise in a credit line to the material. If material is not included in the book's Creative Commons license and your intended use is not permitted by statutory regulation or exceeds the permitted use, you will need to obtain permission directly from the copyright holder. The use of general descriptive names, registered names, trademarks, service marks, etc. in this publication does not imply, even in the absence of a specific statement that such names are exempt from the relevant protective laws and regulations and therefore free for general use.

Contents

List of Figures

Molecular Dynamics and Sensing with Low-Cost Organic-Inorganic Nanostructures

Rachel Elizabeth Brophy

21 November 2024

Abstract

The organic-inorganic methylammonium lead iodide (MAPI) perovskite has become a prominent research topic as a low-cost solution for solar cell technology. However, this material has yet to be commercialized due to its limiting factor of a high degradation rate. One major cause of this degradation is ionic migration. In the first part of this thesis, the migration process is simulated using molecular dynamics. We find that the dominant diffusion corresponds to the migration of iodide vacancies. Our simulations indicate two ways to reduce the degradation rate of the MAPI perovskite due to this migration. The first is adding a compressive strain, which we prove causes the diffusion coefficient to decrease significantly. The second is adding a hydroxyl group (OH-) into the crystal structure, which replaces the iodide vacancy and stops the migration. Each mediating factor is tested on a perfect crystal structure and a grain boundary-infused structure.

Combining the MAPI material with silicon nanowires (SiNWs) prepared at our Nanophysics Center at Reykjavik University is an attempt to stabilize the MAPI material and boost the photovoltaic effect experimentally. This thesis demonstrates an excellent physical matching of such a hybrid structure. However, during this research, we found that the behavior of the silicon nanowires is more complex than expected. The second part of the thesis is dedicated to that, specifically to the detection of organic molecules with silicon nanowires.

SiNWs contain unique and versatile capabilities mainly due to their large surface-to-volume ratio and high sensitivity of current-voltage characteristics. These wires can enhance performance and miniaturization in various fields, ranging from only a few tens of nanometers in diameter. Using a form of wet chemistry, so-called metal-assisted chemical etching (MACE) process, allows for low-cost and highly repeatable fabrication of SiNWs. In the utilization of this structure, we were able to create an ultra-sensitive NO_2 gas sensor. Unlike many commercially available gas sensors, our SiNW-based sensors can operate under high relative humidity concentrations and can experimentally detect 20 parts per billion of NO_2 gas through chemisorption.

Acknowledgments

I am grateful to my excellent supervisors, Andrei Manolescu and Halldór Guðfinnur Svavarsson, for guiding me over the past several years. Their mentorship has allowed me to grow as a researcher, and they recognized my potential from the beginning. I would also like to thank my close collaborators, Mavaffaq Kateb and Kristinn Torfason, for their assistance with the LAMMPS software and DFT calculations. Special thanks to Elham Fakhri, Hákon Örn Árnason, and Muhammad Taha Sultan, who worked closely with me on the fabrication and testing of the SiNWs. I am thankful to Benjamin Junker and Nicolae Barsan from Tübingen University for their assistance and expertise in gas sensors and gas mixing systems.

I am equally thankful to our international collaborators, particularly Ioana Pintillie from the National Institute of Material Physics in Romania and George Alexandru Nemnes from the Research Institute of the University of Bucharest, for their expertise and invaluable contributions.

Thank you, my family and friends, for your support and love throughout my graduate studies; I would not have reached this point without you.

Finally, I dedicate this dissertation to Kristján Högni Kristjánsson, my loving partner, who has always believed in me, even when I struggled to believe in myself.

This work was funded by: the EEA project EEA-RO-NO-2018-0106 “Towards perovskite large area photovoltaics” (PERLA-PV), Landsvirkjun, via the Sustainability Institute Forum of Reykjavik University as the PhD grant “Atomistic studies of organo-halide materials for photovoltaics”, the Reykjavik University Research fund, and the Icelandic Research Fund PhD grant “Atomistic approach to organo-halide materials for photovoltaics (ATOMAP)” 2410684-051.

Part I

Background

Chapter 1

Photovoltaic Effects and Solar Cells

The photovoltaic (PV) effect refers to the generation of an electric voltage between two electrodes attached to a material when exposed to light. In cases where the light source is sunlight, such photovoltaic devices are usually referred to as solar cells. The first photovoltaic device was developed in 1839 by Edmond Becquerel, who observed the effect during electrolysis experiments. While understanding this effect was limited then, Becquerel's discovery marked the beginning of solar cell technology. It took, however, several decades before converting sunlight into electricity became a well-defined field of research. The use of solar cells as a community energy source did not emerge until the 1970s, and even then, they were primarily limited to emergency power and off-grid applications.

By 2000, research into solar cell technology had significantly advanced, and solar cells began seeing broader commercialized applications. Today, they are primarily used to offset grid energy demands during peak hours and offer an alternative to fossil fuels.

Silicon-based solar cells represent the majority of solar cells on the market today. This is due to their high stability, the abundance of silicon in nature, and their non-toxicity. However, silicon-based solar cells are costly, and their average efficiency is still below 20%. Although this number has constantly been rising, it is foreseen that it is reaching its theoretical limit, which is somewhere below 30% [1].

Due to this, other types of solar cells that are not silicon-based have been gaining in popularity over the last decade. This thesis discusses the fabrication and characterization of a new and emerging type of solar cell, the so-called perovskite solar cell, which is not based on silicon. This can be seen through the yellow dots in Figure 1.1. Over the past decade, the efficiency of the perovskite solar cell has increased from 12% to 25% efficiency, making them one of the fastest-growing photovoltaic in terms of efficiency. Additionally, perovskite-based solar cells are cost-effective and have a relatively simple manufacturing process. Despite these advantages, the perovskite material degrades over time under operational conditions, making it unsuitable for commercialization.

This research aims to investigate iodine migration through defects in the perovskite material and develop strategies to suppress or reduce this degradation process.

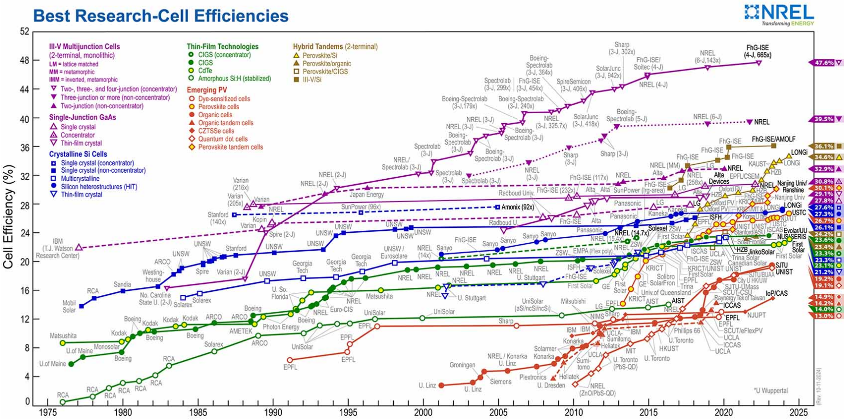

Figure 1.1: Graphical representation of the efficiency growth rates over time for all types of solar cells [2].

1.1 Working Principle of Solar Cells

As mentioned above, the photovoltaic effect enables the conversion of light into electricity. Within a semiconductor, typically of insulator type, is a valence and conduction band. The valence band refers to the outer layer of the atomic shell, implying that the electrons are loosely bound to their core [3]. Meanwhile, the conduction band has unoccupied states in which the electrons from the valence band can excite to. For the electron to enter into the conduction band it must have the minimum energy required to pass through the bandgap. The bandgap can be visualized as the distance between the two bands, as seen in Figure 1.2. In the case of silicon, the bandgap is typically between 1.1-1.4 eVs. [3]

Once the electrons have enough energy to pass through the bandgap they are dislocated from their atomic orbital, creating a vacancy, or ”hole” in the electron’s original position. The combination of a free electron and its corresponding hole is referred to as an exciton [4]. Since an electron carries a negative electric charge, the hole it leaves behind is positively charged. Under typical conditions, the elec-

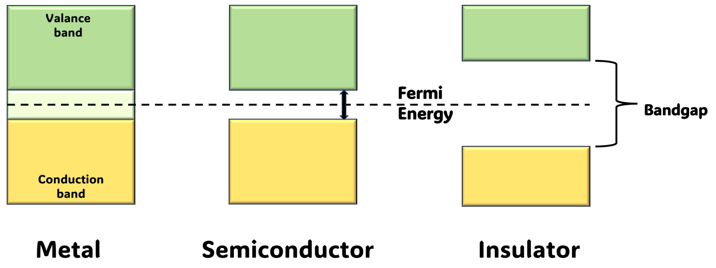

Figure 1.2: Schematic of the variation in bandgaps sizes for metal, semiconductor, and insulator materials.

tron and hole will recombine, preventing the accumulation of electrical charge. However, an electric current may form when the electron and hole are kept apart preventing recombination. Once separated, the electron moves toward the positive electrode and the hole toward the negative electrode, generating an electric current in the external circuit [5].

In most solar cell materials, this separation does not occur spontaneously. To facilitate the generation of electric current, at least two layers of materials must be put together. These layers may form a junction or a multi-junction, directing the electron and the hole toward their respective electrodes. In the following section, the process occurring at the junctions and the junction types will be discussed.

1.1.1 Potential Bias

Junctions create a potential difference within the solar cell material. As the electron is released, it passes through the potential difference forming a photo-excited electrical current. The current can then be harnessed through an external circuit [4].

The most common type of solar cell material is a silicon-based semiconducting material. For clarity, this section will focus solely on the junction properties of solar cells based on this semiconductor. However, it is essential to note that other semiconductor materials also use junctions to fabricate solar cells.

Two primary models are used to describe the electrical properties of silicon-based semiconductors: the band and bond models.

The bond model explains the behavior of semiconductors through covalent bonds holding the silicon atoms together [4]. This process can be visualized as a domino effect; when one electron fills a hole, another hole is generated and this cycle continues allowing the hole to travel through the material until it reaches the negatively charged electrode.

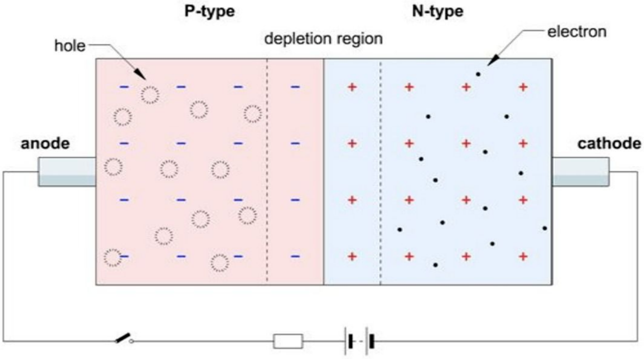

Figure 1.3: Schematic of the p-n junction, showing the vacancy (hole) abundance in the p-type semiconductor and the increase of electrons in the n-type semiconductor [6].

Conversely, the band model describes the silicon's behavior by referring to energy levels between the valence and conduction bands. When the semiconducting material absorbs a photon with sufficient energy, an electron is excited, breaking free from the covalent bonds. The electron then ”jumps” to the conduction band, where it is free to move and conduct a current. The remaining hole stays in the valence band where it can move in the opposite direction [4], pushed by the electric field associated with the potential bias.

The most common type of junction used in solar cells is the p-n junction, shown in Figure:1.3. The junction is created through a process called doping, where several atoms are substituted within the silicon crystal lattice to transform it into either p-type (positive) or n-type (negative) material. For example, silicon can be doped with boron to produce p-type silicon. Doping, therefore, alters the energy states within the material. In p-doped silicon the impurities create states in the energy gap, close to the valence band, where some electrons taken from silicon atoms are blocked, resulting in the formation of holes in the valence band that can move freely. [4]. Similarly, in the n-doped material the electron donor impurities cause a population of electrons in the conduction band [4].

When the p- and n-type materials form a junction, the electron and holes migrate across the junction, forming an electric field. At equilibrium, the Fermi levels of the p-type and n-type materials align. In the presence of an external voltage, this electric field at the junction will either decrease (forward bias) or increase (reverse bias) depending on the direction of the applied voltage [3].

1.2 Types of Solar Cells

Solar cells available on the market today can be broadly categorized into five main types: crystalline silicon cells, multi-junction cells, thin-film technologies, emerging PVs, such as the perovskite solar cells, and hybrid tandem cells [2]. Each category includes a variety of subtypes, which may differ in terms of the semiconductor materials or cell configuration. A fundamental understanding of these categories is essential for a comprehensive understanding of solar cell technology. The following sections will discuss each category's most commonly used solar cell types.

1.2.1 Generation I

Crystalline Solar Cells

As previously mentioned, silicon is the most widely used semiconductor material in solar cells due to its reliability, abundance in nature, and predictable behavior [4]. Silicon is typically found in either mono-crystalline or poly-crystalline form. Mono-crystalline silicon has a uniform crystal structure resulting in higher-quality wafers and lower degradation rates. However, producing pure silicon can be costly and slows down the manufacturing process [4]. A more economical alternative is poly-crystalline silicon, which contains structural defects in the form of grain boundaries [7]. Although this leads to a lower-quality wafer, it does not highly affect the solar cell's overall efficiency.

The average efficiency of crystalline solar cells experimentally is 16%, though theoretical studies have indicated that the efficiency could reach 29%. The gap between experimental and theoretical efficiency is primarily due to bandgap limitations, optical factors, recombination, and electrical resistance losses [3].

The most straightforward design for crystalline solar cells, shown in Figure:1.4, is the single-junction cell. It comprises a p-n junction formed by sandwiching p-type and n-type silicon with an anti-reflective coating on the top [4]. This coating enhances light absorption, increasing the overall energy output. Electrical contacts are placed on the front and back of the cell to complete the circuit.

1.2.2 Generation II

Multi-Junction Solar Cells

Multi-junction solar cells consist of stacking three to five semiconductor junctions in series [9]. This configuration enables the absorption of a broader range of the solar spectrum, with the bandgap energies increasing from the bottom to the top of the stack [10]. Light enters through the top layer where the semiconducting material with the highest bandgap absorbs photons with energies equal

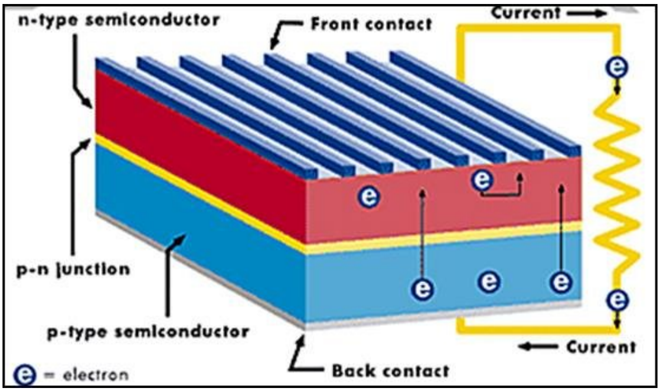

Figure 1.4: Schematic a of single Junction crystalline solar cell[8].

to or greater than its bandgap. Photons with lower energies pass through to the next layer where a material with a lower bandgap absorbs them [9]. This process continues through each layer until the last junction is reached.

A tunneling junction is located between each semiconductor material allowing the electrons of the lower energy conduction band to recombine with the holes from the higher energy valence band. This enhances the photon absorption and reduces energy loss [9].

Multi-junction solar cells typically use III-V semiconductor materials. An example of a three-junction cell is shown in Figure 1.5, where germanium (Ge), indium gallium arsenide (Ga(In)As, and indium gallium phosphide (GaInP) are stacked from bottom to top with tunneling junctions between the layers [11]. The bandgaps for these materials are 0.67, 1.42, and 1.81 eV, respectively [11].

Multijunction solar cells' efficiency is higher than conventional crystalline solar cells, with average efficiencies around 30%, and theoretically potentials exceeding 60% [9]. However, they are expensive and labor-intensive due to the complex material and fabrication processes involved.

1.2.3 Generation III

Thin-Film Solar Cells

Although silicon solar cells dominate the commercial market the wafers necessary for their production are expensive and not accessible in all regions. To address these limitations thin-film solar cell technology was developed. According to M.A. Green, thin-film solar cells can be broadly categorized into two types: those based on silicon and those based on polycrystalline chalcogenide (VI) semiconducting compounds [12].

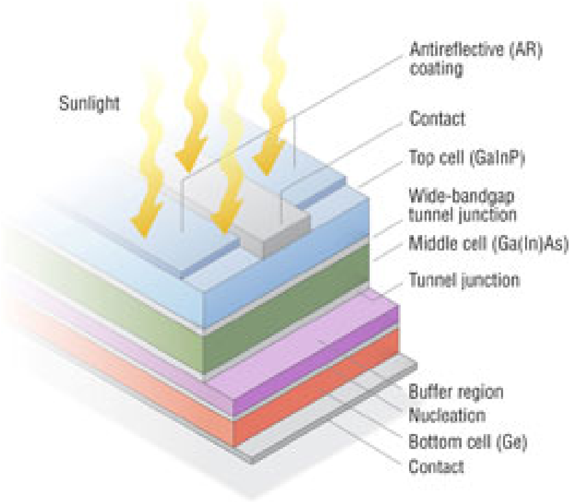

Figure 1.5: Schematic of a multi-junction solar cell containing three cells [11].

Silicon-based thin-film technology involves amorphous or non-crystalline silicon material. This silicon structure allows the material to be deposited at low temperatures allowing for the introductiob of atomic hydrogen. The addition of atomic hydrogen can significantly increase the quality of the material [12]. Since amorphous silicon is not highly conductive it is typically deposited on conductive glass; either indium tin oxide (ITO) or fluorine-doped tin oxide (FTO). Like crystalline silicon solar cells, they can be single or multijunction but have a decreased efficiency of roughly 7% experimentally. A depiction of amorphous silicon multijunction thin-film cells can be seen in Figure 1.6

Chalcogenide-based thin-film cells are typically made from cadmium telluride (CdTe) or copper-indium diselenide (CIS) [12]. As illustrated in Figure 1.7, CdTe thin-film cells are fabricated by first depositing cadmium sulfide onto an ITO glass substrate, followed by the deposition of CdTe using methods such as close-space sublimation, vapor transport, chemical spraying, or electroplating [12]. CIS thin-film cells, in contrast, require a more complex deposition process where the material is sandwiched between two interconnected glass substrates. The efficiency of the CIS thin-film cell is 19.5 % experimentally [12].

While CdTe and CIS thin-films promise higher efficiency, the dangers associated with using cadmium, which is a toxic material, reduces their potential for large-scale production.

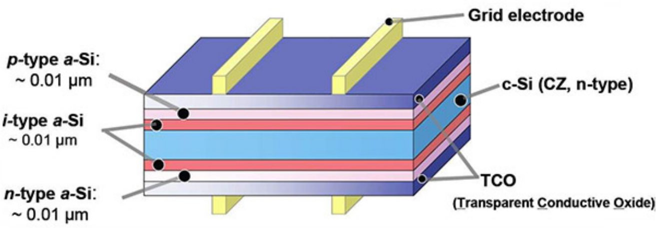

Figure 1.6: Schematic of amorphous silicon thin-film solar cell [13].

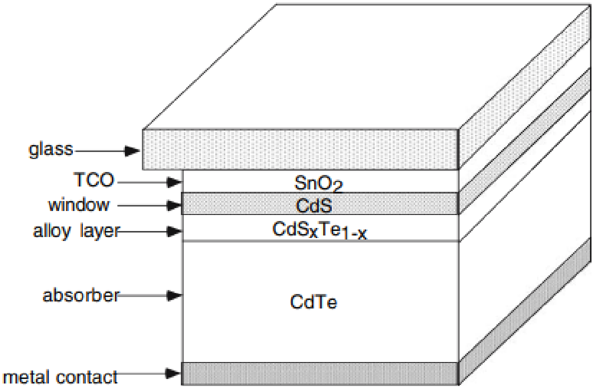

Figure 1.7: Schematic of a Single junction CdTe thin-film cell [12].

Emerging PVs

One of the most promising emerging PVs is the organic-inorganic perovskite solar cell. The halide perovskite solar cell was developed in 2009 by Tsutomu Miyasaka [14], achieving an initial efficiency of 3.1-3.8%. Over the past decade, the efficiency of this cell has almost doubled making it one of the fastest efficiency improvements among solar cell technology. The unique properties of perovskite

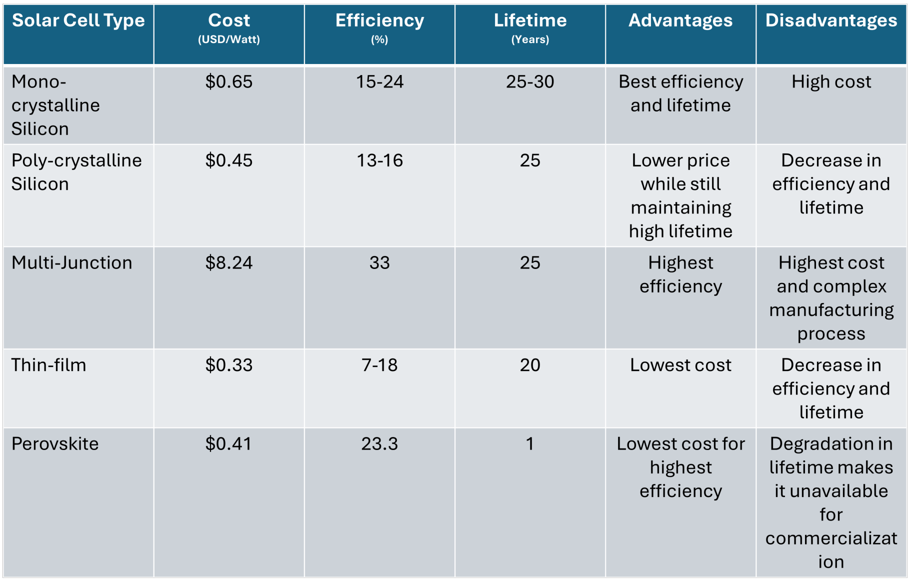

Solar Cell Type	Cost (USD/Watt)	Efficiency (%)	Lifetime (Years)	Advantages	Disadvantages
Mono-crystalline Silicon	$0.65	15-24	25-30	Best efficiency and lifetime	High cost
Poly-crystalline Silicon	$0.45	13-16	25	Lower price while still maintaining high lifetime	Decrease in efficiency and lifetime
Multi-Junction	$8.24	33	25	Highest efficiency	Highest cost and complex manufacturing process
Thin-film	$0.33	7-18	20	Lowest cost	Decrease in efficiency and lifetime
Perovskite	$0.41	23.3	1	Lowest cost for highest efficiency	Degradation in lifetime makes it unavailable for commercialization

Figure 1.8: Comparison of the types of solar cell showing the price/Watt, efficiency, lifetime, advantages, and disadvantages[15]–[20].

materials enable it to convert sunlight into energy within its natural properties without doping mechanisms or additives. This feature, combined with its relatively simple fabrication process, significantly reduces manufacturing costs.

In addition to the standard perovskite solar cell, recent studies have indicated that creating a perovskite/silicon-based solar cell may enhance the perovskite material's stability and increase efficiency. Further information regarding this heterojunction can be found in Chapter 7.0.1

The perovskite material was chosen as the primary focus of this dissertation due to its unique characteristics and rapid growth of solar cell efficiency. Figure 1.8 shows a summary of the types of solar cells listed above, detailing the manufacturing costs, efficiency, lifetime, advantages, and disadvantages. By directly comparing the manufacturing cost with the efficiency, the perovskite-based solar cell offers the cheapest cost while maintaining one of the highest efficiency. However, while analyzing the lifetime, the average is only one year. This severely limits the viability of the perovskite-based solar cell in becoming commercially attractive.

By understanding the major causes of degradation within the perovskite material, it may be possible to offer solutions to mitigate or suppress the degradation. Finding a solution to this issue could make it possible for the perovskite-based solar cell to be a lower-cost alternative to the mono-crystalline solar cell.

Chapter 2

Perovskite Solar Cells

Perovskite Structure

A perovskite is defined as a material of type ABX_3, where A, B, and X are different atoms or molecules. The main configuration of the perovskite material can be visualized as a cube, with the A atoms located at the center, the B atom on the corners, and an X atom in the middle of the edges [21].

Various perovskite materials can be used in photovoltaic applications such as $CaTiO_3$, $BaPbI_3$, $CsPbBr_3$, $MAPbI_3$, or $BaPbI_3$. Some perovskites are ferroelectric, meaning they possess an intrinsic electric field [22]. This arises from a slight tilt or deformity in the cubic lattice. This may cause a mismatch between the positive and negative charges at the center resulting in an electric dipole within the unit cell [21].

A large part of this thesis is based on the specific perovskite material methylammonium lead iodide (MAPI), or $CH_3NH_3PbI_3$. In this case, the A, B, and X components correspond to the organic cation molecule methylammonium (MA), the inorganic cation lead (Pb), and the halogen anion iodide (I), respectively. Structurally, the Pb and I atoms form a rigid lattice or cage, with the MA molecule in continuous rotation at the center. A representation of this crystal structure was created using LAMMPS software, as shown in Figure 2.1

In some conditions, MAPI behaves like a ferroelectric material, although not a strong one [23]. However, the key aspect of the photovoltaic effect in MAPI is the electric dipole of the MA molecule. In the MAPI perovskite material, the dipole is critical in converting light into electricity. When a photon enters the material, it generates an exciton. The continuous rotation of the MA molecules maintains an internal electric field which keeps the electron-hole pair separated and directs them toward their respective electrodes. [21].

Previous density functional theory (DFT) studies have shown that the methylammonia molecules within the PbI cage prefer a facial orientation when temper-

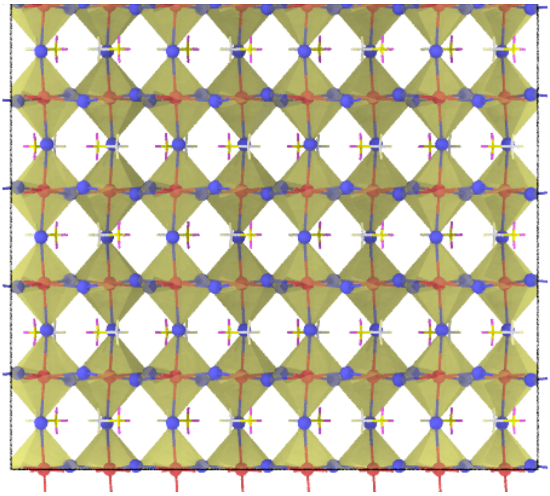

Figure 2.1: Visualization using the OVITO software of the perfect MAPI perovskite structure. The red spheres denote the Pb atoms, and the I− atoms are the blue spheres. The MA molecule is shown through its bonds. The overall slightly tilted orthorhombic structure occurs at 300K.

ature is not considered [21]. However, the structure of the perovskite material is highly temperature-dependent.

At low temperatures (<165 K), the material adopts an orthorhombic phase with all three sides of the unit cell slightly different in length. As the temperature increases to 375 K, the structure transitions into a tetragonal phase where two of the sides become equal, and the third at a slight angle. The cations are no longer fixed in this phase and the cation molecules occupy two non-equivalent positions [21]. Above 375 K, the material transitions into a cubic structure where all sides of the unit cell are equal.

The operational structure of perovskite materials occurs between 165 K and 375 K, with molecular dynamics (MD) simulations typically performed around 300K to ensure that the cation molecules remain mobile. It has been observed that temperatures above room temperature may lower the system's total energy and increase structural distortions by reducing the molecular dipole. The dipoles are generated through the rotational mobility of the MA molecules which involves the twisting of the head and tail groups [21]. This rotational movement induces slight distortions in the Pb-I bonds, thus generating the dipole [21].

2.1 Degradation

Degradation can be explained by the slow breakdown of the solar cell. This may result in a decreased efficiency over time or in some cases, the cell stops working completely. In most commercialized silicon-based solar cells, degradation occurs over ten years dropping to 90% maximum power and 80% after 25 years [24]. However, it is essential to note that the silicon material may not be the leading cause of degradation. The other components of the solar cell added during installation pose the highest threat to an increase in degradation. This may include the junction box, the adhesion of the layers, and broken glass [24]. Most often, moisture penetration into the PV module leads to the corrosion of the junction box's metal components, resulting in detrimental effects on the electrical conductivity [24]. In addition, high humidity areas may cause adhesion between the layers of the solar cell, which may lead to an increase in light reflection and swelling of the cells [24].

When speaking specifically about silicon, light-induced degradation proves to be the primary influence in degradation. Light-induced degradation can be seen as a decrease in the short circuit current and open circuit voltage [25]. It is suspected that an increase in the minority carrier concentrations causes the degradation, specifically in boron-doped silicon [25]. Lindroos et al., also suggest a relationship between increased temperatures (>300 K) and an increase in the minority concentrations [25]. In further support of this relationship, another study conducted tests of light-induced degradation at elevated temperatures (50 °C and 95 °C) [26]. This study concluded that both high injection densities and elevated temperatures accelerate degradation in silicon-based solar cells [26]. However, it should be noted that this degradation is slow, and detrimental effects do not occur until several hundred hours under constant light and elevated temperatures [26]. In addition, after maximum degradation is reached, a regeneration effect is shown in some cases. However, there are limited results on this effect since the timescale of this response is over the warranted study time [26].

Overall, the degradation patterns regarding the solar cells outlined above take 10-20 years to reduce the cell to be nonviable. Elevated temperatures and an increase in minority carrier concentration may accelerate this degradation; however, when computing the cell's lifetime, these effects are considered.

2.1.1 Degradation in MAPI Perovskite

As mentioned earlier, although perovskite materials present a low-cost solution for manufacturing solar cells, they have not yet reached commercialization due to their high degradation rate and short shelf life. The primary factors contributing to this instability are moisture and humidity, temperature, hysteresis, and solution processing [27].

Later sections of this thesis will provide detailed explanations of the steps involved in fabricating perovskite materials and complete perovskite solar cells. However, for this section it is vital to highlight the precursor materials used to better understand the chemical breakdown that leads to degradation. The key precursors are methylammonium iodide (MAI) powder and lead iodide (PbI_2) beads. These are dissolved in a solvent mixture of dimethyl sulfoxide (DMSO) and dimethylformamide (DMF), and chlorobenzene is used as an antisolvent during the final fabrication stage.

Effects of Moisture and Humidity

As water molecules infiltrate the perovskite material they act as a catalyst, triggering the chemical structure's breakdown and reverting the material to its precursor material. Specifically, the Pb atoms typically bond together break their initial bonds and, instead, bond to two I atoms leaving the third I atom to bond with a hydrogen atom. This results in the reformation of PbI_2. This reaction significantly reduces the material's light-absorbing layer and shifts the band edge over time, contributing to the degradation of the perovskite material [27].

Additionally, MD simulations have shown that water molecules can fully disperse within the perovskite material due to polarization [28]. However, this dispersion is not the primary cause of degradation. Instead, the water molecules interfere with the bonding between MA and I^- ions, leading to the formation of ammonia (NH_3) and hydroxide (OH^-) [29]. These chemical reactions further accelerate the degradation of the perovskite solar cells.

Effects of Temperature

As previously discussed, the perovskite materials are highly sensitive to lattice changes when exposed to elevated temperatures. The most devastating lattice change is the switch from a tetragonal to a cubic structure, initially believed to occur at 375K based on X-ray diffraction studies. However, research by Cojocaru *et al.*, revealed that this transformation begins at a lower temperature of 328K during a gradual temperature increase, slowly changing the structure [30].

Beyond lattice changes, temperatures exceeding 300K accelerate the degradation of the perovskite material. This degradation results from increased atomic mobility within the system, similar to the effects caused by moisture and humidity. At elevated temperatures the precursor material PbI_2 reforms, significantly reducing the material's stability and contributing to its breakdown. [31].

Ionic Migration

Ionic migration refers to the movement of ions throughout the material, disrupting its overall structure. It was experimentally shown that iodine atoms are dislocated by the electric field between the electrodes, and they reach the anode as negative ions, or iodides [32]. This migration occurs due to the underlying distribution of iodine vacancies, causing the ions to migrate in an attempt to fill the vacancy. To better understand this defect, kinetic experiments and first-principle methods were used to determine the migration pattern under working conditions.

MD simulations were utilized to determine which vacancy defects (iodide, lead, or methylammonium) cause the most damage to the crystal structure [33]. A vacancy is created by removing a single atom from an otherwise 'perfect' structure. Since it is difficult to trace a 'hole' migration, the other atoms surrounding the vacancy determine the migrational patterns of the atoms in question.

Atoms with a lower activation energy are more commonly the atoms that will migrate throughout the material. In the case of the MAPI perovskite, iodide has the lowest activation energy of 0.58 eV. Due to this, iodide migration is believed to be the leading cause of ionic migration in the MAPI perovskite. The migrational pattern of the iodide atom typically takes the shortest route to fill the vacancy. This path may deviate slightly from a linear route to avoid other iodide sites [34]. However, since filling the initial vacancy ultimately causes another vacancy, the final effect will be the constant migration of different iodide atoms, each trying to fill a vacancy. The continuous migration of the iodide atoms causes the breakdown of the perovskite material over time, reducing its overall efficiency. The speed at which the iodide ions travel depends on external conditions, such as temperature or an external electric field.

Hysteresis

Hysteresis is commonly found in a current-voltage (I-V) scan of solar cell devices. I-V characteristics are performed in the testing phase of photovoltaic devices to determine peak operational conditions. This scan works by completing both a forward (short circuit to open circuit) and reverse scan, providing information on the short circuit current and open circuit voltage. This process is performed to calculate the fill factor, the power conversion efficiency, and the maximum power the device can theoretically provide.

The optimal I-V characteristic would show the forward and reverse scan following the same line with no deviation. When hysteresis is present, the forward and reverse scans are not identical, meaning either that the reverse scan is higher than the forward scan (normal hysteresis) or the opposite in which the forward scan is higher than the reverse (inverted hysteresis) [35]. This phenomenon is thought to be caused by the scan rate being faster than the rate of charge accumulation associated with migration of iodine, electric polarization of the material, traps, and the space charge relaxation time. Depending on where the hysteresis curve is, either in the forward or backward scan, this can imply that the transient carrier collection is more effective in one way than the other [36], [37] .

The hysteresis effect is expected to be seen in the perovskite solar cell while running the I-V scan. MD simulations found that ionic migration due to defects within the perovskite material may be the leading cause of the hysteresis effect [38]. As mentioned above, iodide is the dominant cause of ionic migration in the presence of a defect. This migration alters the polarization within the material, which alters the carrier collection, leading to the hysteresis effect.

Chapter 3

Silicon Nanowire Fabrication

Due to their chemical, mechanical, optical, electronic, and thermal properties, silicon nanowires (SiNWs) can be used for various applications. Depending on the fabrication process, the production of silicon nanowires can be relatively cost-effective and easy. There are several ways to fabricate SiNWs; however, for simplicity reasons, we can categorize them as either bottom-up or top-down techniques. Depending on dry etching or wet chemistry etching, the fabrication process can be split up even more within these two categories.

However, it is essential to mention that other fabrication processes may need to be used depending on the criteria of the desired silicon nanowires. For the fabrication process's specific nanowire diameter and spacing, a mesh may be required. In this case, vacuum-based metal deposition is commonly used instead, although this technique is not within this project's scope.

3.0.1 Bottom-up

Chemical Vapor Deposition

The Vapor-Liquid-Solid (VLS) mechanism is a type of chemical vapor deposition used for fabricating silicon nanowires and is one of the most common fabrication methods. Silicon wafers with metal nanoparticle catalysts are exposed to high-temperature annealing under the inert gas flow [39]. During this process, silicon monoxide (SiO) vapors are created and absorbed initially by the metal catalyst on top of the Si wafer. This injection initiates the Si ions to penetrate the bulk of the metal catalyst, leading to a Au – Si catalyst solution [39]. Oxygen molecules are then absorbed into the catalyst solution, binding with the Si ions to form SiOx, initiating the oxidation phase. This oxidation starts at the liquid-solid interface and is imperative to the growth of the SiNWs. The schematic of this process can be seen in Figure 3.1

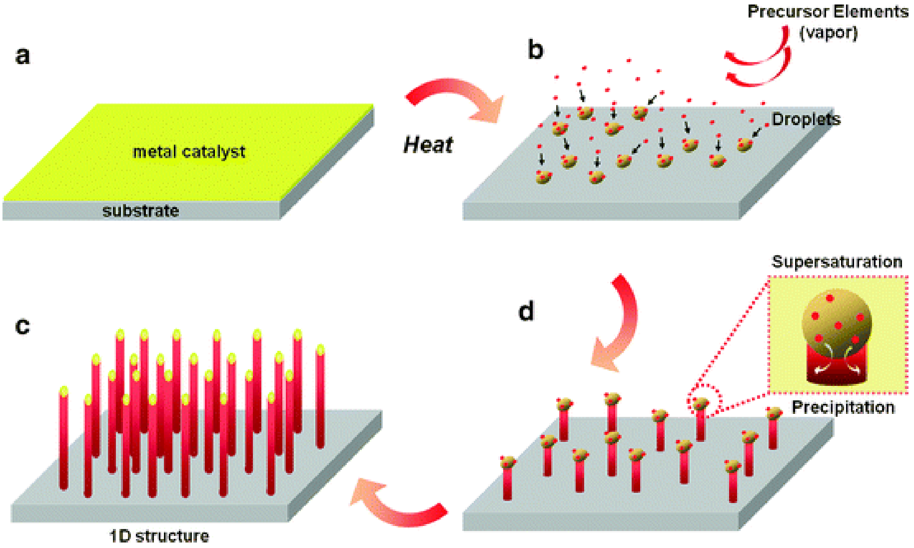

Figure 3.1: Schematic of the VLS method of SiNWs fabrication [40].

Although this process is one of the most common mechanisms for SiNW growth, it is time-consuming; 10 nm diameter growth takes roughly 30 mins. However, the nanowires formed during this time are of good quality, and their lengths can be controlled simply by time alterations.

3.0.2 Top-Down Etching

MACE Procedure

As mentioned above, the MACE procedure is one fabrication process for top-down etching. A basic description of this method involves the deposition of a metal catalyst onto a semiconducting material (typically a silicon wafer). After the deposition, the wafer is placed into an etching solution containing a mixture of an oxidizer and acid for a set time, depending on the desired length of the wires. Finally, the wafer is dipped into nitric acid (HNO_3) to remove access metal particles (Figure:3.2. The final chemical reaction can be seen below: [41]

$$\mathrm{Si} + 2\mathrm{H_2O_2} + 6F^- + 4H^+ -> [\mathrm{SiF_6}]^{2-} + 4\,\mathrm{H_2O} \tag{3.1}$$

The most important aspect of this procedure is the metal catalyst required to enable a charge transfer for the Si wafer's oxidation and breakdown. In the first step of the MACE procedure, the deposition of the metal particles onto the Si wafer

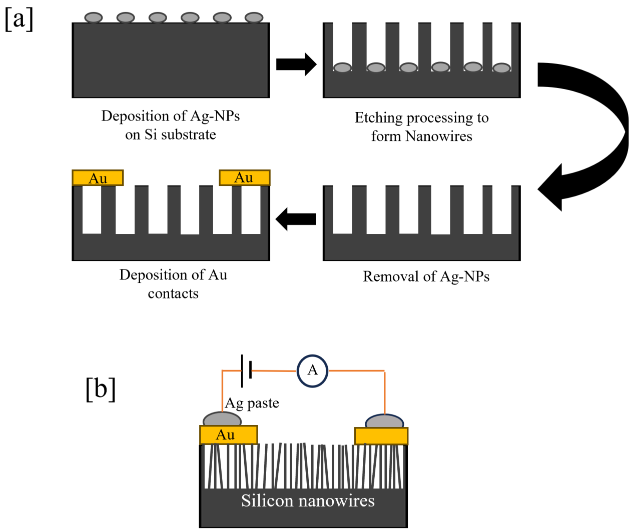

Figure 3.2: (a) is a schematic of the MACE procedure steps, starting with the deposition of the Ag-NPs, the process of etching, removal of Ag-NPs, and finally, the placement of contacts. (b) is a depiction of the final configuration of the silicon nanowire sensor.

results in band bending of the silicon, ultimately causing equilibrium between the Fermi level of Si and the work function of the metal catalyst [41]. This results in the creation of a Schottky barrier inhibiting the charge transfer at the conduction band; since the redox reaction has a higher positivity than the valence band of Si, the valence band will release electrons and accept holes overcoming the barrier [41]. The metal catalyst increases the reduction rate of H_2O_2, increasing the overall hole injection rate into the valence band. This causes the Si underneath the metal catalyst to dissolve much faster than the Si without the metal adhesion, forming nanowires.

Reactive Ion Etching

The reactive ion etching (REI) process is an alternative to the MACE procedure. All steps in the etching process, passivation, physical etching, and chemical etching, coincide [42]. This process is classified as dry etching and utilizes chemically reactive plasma as the etching mechanism. The plasma is created through radio frequency and initiates an acceleration of the electrons. Some of these electrons will permeate the silicon, making it highly negative. Since the reactive ions are positive, they are drawn to the silicon substrate and may begin the etching process [42]. However, once the Si layer is passivated, chemical etching may be halted, and additional energetic ions must be used to continue the process [42]. Experimentally, halogen ions are used as the plasma species with either SF_6 or chlorine (Cl_2) as the plasma source. The passivation gas, typically C_4F_8, increases the anisotropic effect [42]. A visual of this mechanism is seen in Figure 3.3

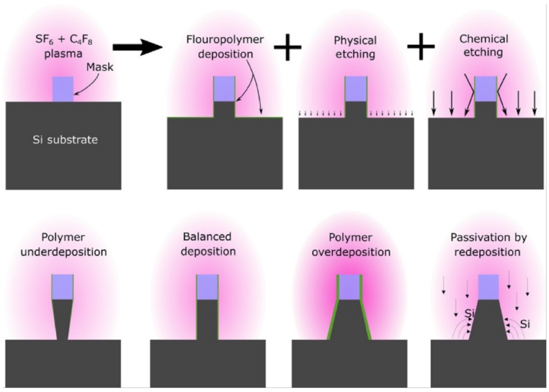

Figure 3.3: Schematic of the REI method for SiNWs [42].

REI allows for simple changes in the morphology of the SiNWs since altering the plasma gas, flow rate, and temperature can all provide various morphological changes.

Part II

Molecular Dynamic Simulations

Chapter 4

Molecular Dynamics

Molecular dynamics simulations are used in various fields of study, such as physics and chemistry, to replicate the natural behavior and processes of atoms and molecules in real time. For example, in a solid structure, one may use molecular dynamics to simulate the deformation and breaking of bonds in a system to study how the material reacts to varying conditions [43]. These simulations use computer simulations to numerically solve Newton's equations of motion for each atom or molecule within the system.

Although the simulations numerically solve the equations of motion, it is essential to consider the system's overall structure. For example, different sets of equations must be used when evaluating a rigid structure (i.e., Euler equations) or structureless particles (i.e., Newton's equations) [44]. In addition, other parameters might be factored into the simulations, such as whether the system includes long-range interactions, short-range interactions, if the system is in equilibrium, the complexity of the structure, and so on. All of the details mentioned above may be intermixed into the same simulation. It is possible to have some molecules within the system be in a rigid structure while other atoms are structureless. External factors like temperature, external electric field, and relaxation periods may also be added to the simulations to create a more 'real-time' model. It is also important to note that molecular dynamics can be used to track the trajectory of atoms as they move throughout the system, which may occur naturally or due to the external factors previously mentioned.

Several factors must be considered for a solid-state system before initiating the simulation. First, all the forces that are present in the system must be taken into consideration. For example, all ions having the same sign (+,+, or -, -), have forces that will repel each other, whereas ions of opposite signs will attract. The Coulomb force approximation is suitable when the atoms in question are relatively far from each other. However, when atoms are at short range, the overall electronic structure of the system is needed to acquire accurate force models. Second, the boundary conditions need to be set. A periodic boundary condition will allow the atoms to cross the boundary, meaning that if an atom crosses the top boundary, it will reappear at the bottom boundary. In contrast, non-periodic boundary conditions do not let the atoms cross and reappear on the opposite side; either the atoms that cross will be deleted from the system (fixed), or the system will always include all atoms even if the boundary is crossed (shrink-wrapping) [45]. Lastly, the initial state of the atoms must be defined. This may include the temperature, electric field, velocity, and, most importantly, the initial lattice structure. The lattice structure tells the software where all atoms are located at the start of the simulation; it is set before any other conditions can alter the system's structure.

4.1 Time Evolution: Verlet Algorithm

The simulations operate in real time to predict the movement of the atoms in the system. Various algorithms have been developed to forecast the particle's future position and velocity based on their prior kinetic and potential energy. These numerical algorithms are typically based on Newton's second law by solving the classical equations of motions, where time t is discretized in class steps Δt.

Consider a particle of mass m moving in the direction x under the action of a force F_x. Assume the particle's position at time t, denoted $x(t)$, is known. The position at the time $t + \Delta t$ can be determined by performing a Taylor series expansion,

$$x(t+\Delta t) = x(t) + \dot{x}(t)\Delta t + \frac{1}{2}\ddot{x}(t)(\Delta t)^2 + \frac{1}{6}\dddot{x}(t)(\Delta t)^3 + \mathcal{O}\left((\Delta t)^4\right) , \tag{4.1}$$

The dots represent derivatives with respect to time, and the final term indicates corrections of the order of the $(\Delta t)^4$ or above. Similarly, we can obtain the position at a $t - \Delta t$ by using a negative time step.

$$x(t-\Delta t) = x(t) - \dot{x}(t)\Delta t + \frac{1}{2}\ddot{x}(t)(\Delta t)^2 - \frac{1}{6}\dddot{x}(t)(\Delta t)^3 + \mathcal{O}\left((\Delta t)^4\right) . \tag{4.2}$$

Adding these equations eliminates the off derivatives, resulting in:

$$x(t+\Delta t) + x(t-\Delta t) = 2x(t) + \ddot{x}(t)(\Delta t)^2 + \mathcal{O}\left((\Delta t)^4\right) . \tag{4.3}$$

Thus, Equation (4.3) allows us to calculate the position at time $t+\Delta t$ if the positions at the previous two-time steps are known and if the acceleration $a_x = \ddot{x}(t)$ at time t is known. Denoting now $x(t-\Delta t) = x_0$, $x(t) = x_1$, and $x(t+\Delta t) = x_2$, we obtain

$$x_2 = 2x_1 - x_0 + a_x(\Delta t)^2 , \tag{4.4}$$

which is known as the Verlet equation for position. Here, we have neglected the higher-order terms, $\mathcal{O}\left((\Delta t)^4\right)$, and it is important to notice that they correspond to tiny, negligible corrections proportional to two extra powers of the time step concerning the acceleration term. Therefore, the Verlet algorithm can be very efficient. The acceleration at time t is calculated from Newton's second law, $F_x = ma_x$, and in general, the force depends on time.

Moreover, we can change the sign of Equation (4.2) and add it again to Equation (4.1), and we obtain

$$x(t + \Delta t) - x(t - \Delta t) = 2\dot{x}(t)\Delta t + \frac{1}{3}\dddot{x}(t)(\Delta t)^3 \,, \tag{4.5}$$

and the velocity of the particle at time t, that is $v_x(t) = \ddot{x}(t)$, can also be calculated assuming that the positions x_2 and x_0 are known, as

$$v_x(t) = \frac{x_2 - x_0}{2\Delta t} \,, \tag{4.6}$$

which is known as the Verlet equation for velocity. As before, the residual value to be neglected is smaller than the main result by two orders of magnitude of the time interval, i.e. $\mathcal{O}\left((\Delta t)^2\right)$.

In practical implementations, the calculation begins with the initial conditions of position and velocity. Let's call them $x(t = 0) = x_1$ and $v(t = 0) = v_x$. In a molecular dynamics problem, the force acting on the particle is a combination of forces created by many other particles that move around,

$$F_x(t) = \sum_i F_{i,x} \,. \tag{4.7}$$

The label i indicates each particle interacting with the particle whose motion we describe. Given the current positions of all these particles (or, at this step, the initial positions), the force F_x and then the acceleration a_x of the particle we focus on can be calculated, and then Equation (4.1) gives its position after the first time step,

$$x_2 = x_1 + v_x\Delta t + \frac{1}{2}a_x(\Delta t)^2 \,. \tag{4.8}$$

Now, we will change the notation x_1 into x_0 and x_2 into x_1, i. e. $x_0 = x(t = 0)$ and $x_1 = x(\Delta t)$, and we calculate $x_2 = x(2\Delta t)$ using Equation (4.4). Then, we can update the velocity, corresponding to the first time step, $v_x(\Delta t)$, using Equation (4.6).

Every particle in the system is evaluated the same way, and each timestep is updated by the particle's force changes and acceleration to present the new location. For example, the new position x_2 in Equations (4.4 is found by substituting $x_1 \to x_0$ and $x_2 \to x_1$. In this version of the Verlet algorithm, the velocities of the particles are calculated one time-step behind the latest position x_2, but only if the timestep is small enough. However, another version of the algorithm, the velocity Verlet algorithm, can update the velocities at the same timestep through calculations based on the acceleration.

To get accurate results, the size of the timestep, Δt, must be determined based on how fast the particles move. This is estimated based on the mass of each particle and the forces surrounding it. For the MAPI system, we can consider the iodine atom, whose mass is $m \approx 163$ atomic units $\approx 2.1 \times 10^{-25}$kg. (1 au = 1/12 $C_6^{12} \approx 1.66 \times 10^{-27}$ kg). The roughly estimated force acting on this atom is an electrostatic force corresponding to two-point charges. This is due to one electron ($q \approx 1.6 \times 10^{-19}$ Coulomb) migrating from the Pb atom to the I atom, separated by a distance $L \approx 3.2$ Å, like in MAPI. Of course, the I atom interacts with more Pb atoms, but we are only interested in a rough estimation. The estimated acceleration of the I atom due to one single Pb atom is

$$a_x = \frac{F_x}{m} = \frac{q^2}{4\pi\varepsilon_0 L^2 m} , \tag{4.9}$$

where $\varepsilon_0 = 8.85 \times 10^{-12}$ F/m is the vacuum permittivity. We want the time step to be small enough such that the last term in Equation (4.4) is a minor (incremental) correction to the distance L between the two atoms, i. e. we want $a_x(\Delta t)^2 \ll L$, which implies

$$\Delta t \ll \sqrt{\frac{L}{a_x}} = \sqrt{\frac{4\pi\varepsilon_0 L^3 m}{q^2}} \approx 1.7 \times 10^{-13} \text{ s} . \tag{4.10}$$

To satisfy this requirement, we should consider a time step two orders of magnitude smaller than this reference value, $\Delta t = 10^{-15}$ s $= 1$ fs (femtosecond), or even smaller.

To accurately describe the movement of the atoms in a three-dimensional system, the Verlet algorithm must be calculated in the directions of x, y, and z. For the macroscopic system, periodic boundary conditions must be placed so no atoms are lost.

In addition, the Verlet algorithm may also be expanded to include rigid bodies within the system, like that of the methylammonium in MAPI. In this case, we must consider the torque, the moment of inertia, and the angular acceleration of the molecules within Newton's equations [46].

4.2 Thermodynamic Ensembles

As mentioned above, molecular dynamic simulations solve the equations of motion in time. For this, the potentials of all atoms in the system must be calculated. The size of the system can range from several atoms, or, in the case of MAPI it can correspond to a macroscopic system, with the number of atoms in the thousands range. For a macroscopic system, a finite set of atoms is extended with periodic boundary conditions to simulate a periodic 3D system without the computation costs. However, other thermodynamic parameters, such as pressure and temperature, must be considered when working with an extensive system.

Thermodynamic ensembles must incorporate a set temperature or pressure within the system. They can recreate real-life environments to understand better how the system will react to specific stressors. The ensembles alter the equations of motion to adjust to external and internal variables. In this project, two ensembles, the canonical ensemble (NVT) and the isothermal-isobaric ensemble (NPT), were utilized to maintain a constant temperature and pressure, respectively [44].

Canonical Ensemble (NVT)

The canonical ensemble (NVT) is implemented to control the system's temperature. This ensemble uses three parameters: the number of atoms, N, the system's volume, V, and the temperature, T. For the simulations presented in this thesis, the Nosé-Hoover thermostat model was used to create more degrees of freedom fictitiously with a coordinate parameter x_t, mass m_t, and the thermodynamic friction coefficient ζ_t, which depends on x_t and $\dot{x}_t$ [44]. The NVT ensemble calculates the redefined equations of motion for each particle with mass M, coordinates X, and temperature x_t. The equations are:

$$\dot{X}(t) = V(t)\,, \tag{4.11}$$

$$M\dot{V}(t) = F(X(t)) - \zeta_t M V(t)\,, \tag{4.12}$$

$$m_t \dot{\zeta}_t(t) = 2M\dot{X}^2 - g\kappa_B T\,, \tag{4.13}$$

where g is the degrees of freedom. NVT ensembles also have a conserved energy of the form:

$$\hat{H}_{NVT} = \frac{1}{2}MV^2 + E(X) + \frac{1}{2}m_t\zeta_t^2 + g\kappa_B T x_t\,. \tag{4.14}$$

The first two terms are the particle's kinetic and potential energies, and the last describes the thermostat's energy.

Isothermal-Isobaric Ensemble (NPT)

The isothermal-isobaric ensemble (NPT) is used to control both the pressure, P, and the temperature T in the system. Unlike the NVT ensemble, the number of atoms in the system is not under control. However, it is defined as a dynamic variable. The Nosé-Hoover thermostat model is again utilized, but new variables, x_p, m_p, and ζ_p, are incorporated for the position, mass, and friction coefficient of a barostat in contact with the system. The equations are now altered as: [44]

$$\dot{X}(t) = V(t) + \zeta_p X\,, \tag{4.15}$$

$$M\dot{V}(t) = F(X(t)) - M\dot{V}\left[\left(1 + \frac{3}{g}\right)\zeta_p + \zeta_t\right]\,, \tag{4.16}$$

$$\dot{\nu}_l = 3\nu_l\zeta_p\,, \tag{4.17}$$

$$m_p\dot{\zeta}_p(t) = 3\nu_l(P_{in} - P) + \frac{3}{g}(MV^2) - m_p\zeta_t\zeta_p\,, \tag{4.18}$$

$$m_t\dot{\zeta}_t(t) = 2MV^2 + \frac{\zeta_p^2}{m_p} - (g+1)\kappa_B T\,. \tag{4.19}$$

Here, ν_l is an external volume associated with the piston. To incorporate both the internal pressure P_{in} and external pressure P_0 the equation below is used:

$$P_{in} = \frac{2}{3\nu_l}\left[E_k - vir - \left(\frac{3\nu_l}{2}\right)\frac{\partial E(X, \nu_l)}{\partial \nu_l}\right]\,, \tag{4.20}$$

where E_k is the total kinetic energy and (the virial) $vir = -\sum_i x_i F_i$ includes the position and force acting on each particle i. Finally, the conservation of energy is supplied through:

$$\hat{H}^{NVP} = \frac{1}{2}MV^2 + E(X, \nu_l) + \frac{1}{2}(m_p\zeta_t^2 + m_p\zeta_p^2) + (g+1)\kappa_B T x_t + P\nu_l\,. \tag{4.21}$$

Chapter 5

Molecular Dynamics of MAPI

5.1 *Ab initio* Molecular Dynamics (AIMD)

Mosconi et al. developed the *ab initio* molecular dynamics method for the MAPI perovskite by using a derivative of the DFT approach. The *ab initio* molecular dynamic method assumes that the system is only formed of nuclei and electrons. This approach calculates the electronic polarization due to chemical bonds breaking and reforming [47]. To understand the different energies in the system, the position of the nuclei is determined through Newton's equations of motion:

$$M\ddot{R} = -\nabla[\epsilon + V_{NN}]\,, \tag{5.1}$$

This equation shows that the energies depend on the position of all the nuclei in the system, with M as the mass of the nucleus at position $\ddot{R}$. The incorporated energies ϵ and V_{NN} are the gradient of single electron energies and the of the internuclear potential, respectively.

The electronic energies are derived using the DFT method in the Kohn-Sham formulation. Here, the total energy is calculated using the density of the electrons, $n(r)$, which is solved for by incorporating all the occupied atomic orbital, ψ_i, $n(r) = \sum_i |\psi_i(r)|^2$, and the interaction potential between a single electron and all nuclei, V_ext:

$$E = -\frac{1}{2}\sum_i \int dr\, \psi_i^*(r)\nabla^2\psi_i(r) + \frac{1}{2}\int drdr'\, \frac{n(r)n(r')}{|r-r'|} + E_{xc}[n] + \int dr\, n(r)\, V_{ext}(r)\,. \tag{5.2}$$

In this approach, the energy is not dependent on the motion of the nuclei. It is minimized concerning the electron density at each new position of the nuclei, given from Newton's equations of motion.

The dynamics of the nuclei are appropriately incorporated in the Car-Parrinello Lagrangian approach, where the electronic wave functions ψ_i are considered functions of time, together with the positions of the nuclei [48]. The Lagrangian functional is written as

$$L = \mu \sum_i \int dr |\dot{\psi}_i(r,t)|^2 + \frac{1}{2} \sum_{I=1}^{N} M_I \dot{R}_I^2(t) - E[\psi(t), R(t)] + \sum_{i,j} \Lambda_{ij} \left(\int dr \psi_i^* \psi_j - \delta_{ij} \right) . \tag{5.3}$$

The last term in the equation, the Lagrange multiplier, is used to ensure the atomic orbital remains orthogonal. The following equations are utilized to follow the movement of the atoms and are obtained through the sets of all nuclear positions $R \equiv [R_I]$ and all electronic wave functions, $\psi \equiv \psi_i$. This is done for every nucleus I and electron i:

$$M_I \ddot{R}_I(t) = -\frac{\partial}{\partial R_I(t)} E[\psi(t), R(t)] , \tag{5.4}$$

$$\mu \ddot{\psi}_i(r,t) = -\frac{\delta}{\delta \psi_i^*(r,t)} E[\psi(t) R(t)] + \sum_j \Lambda_{ij} \psi_j(r,t) . \tag{5.5}$$

Due to the number of approximations in the computational method, the electronic degrees of freedom are not incorporated within the equations and are instead seen as interactions [48].

Specifically, for the MAPI material, the AIMD simulations outlined above were used to determine the structural and electronic properties. They were compared with IR spectroscopy (dipole-dipole correlation function) to ensure accuracy. These studies showed that the MA molecule can rotate within the inorganic space in the pico-second timescale. Further calculations were done to determine the molecular ordering, molecule rotation ability, and thermal effects [47]. However, the AIMD simulations are size-restrictive, limiting the material size to only 25-50 unit cells due to computational time. As this study aims to determine the cause of degradation within the MAPI material, longer time scales are necessary, making the AIMD method inappropriate.

5.2 Force Field Molecular Dynamics: MYP

In contrast to the AIMD method, the force field molecular dynamics method can withstand a longer evolution time, and the number of atoms in the system can be increased to thousands of atoms. However, the accuracy of the final results may be slightly skewed. This method relies on the potential or force fields to simulate the movement and reaction of the atoms in the system. Due to this, any cluster of atoms or molecules is considered as individual atoms being held together through the force fields implemented.

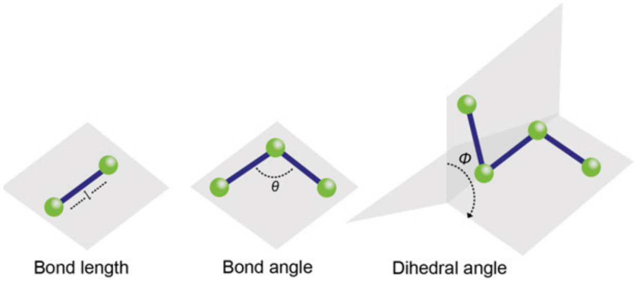

Figure 5.1: Schematic illustration of bond length, the bond angle, and the dihedral angle.

The potential utilized in our simulations is based on the MYP potential model, explicitly created for hybrid organic-inorganic perovskites by Mattoni et al. [47]. The MYP potential model uses several potentials to describe the various interactions within the MAPI structure. For the ionic crystals, the Buckingham-Coulomb (BC) potential is used:

$$U_{ii} = \sum_{ij} A_{ij} \exp(-\frac{r_{ij}}{\rho_{ij}}) - \frac{c_{ij}}{r_{ij}^6} + \frac{q_i q_j}{4\pi\epsilon_0 r_{ij}} \,. \tag{5.6}$$

The first three terms in the summation are repulsive, attractive, and Coulombic interactions. Here $q_{i/j}$ denote the charges of i and j atoms with r_{ij} as their distance.

For the inorganic aspect of the MAPI perovskite, the organic molecules utilized the generalized AMBER force fields (GAFF) to account for bonded and nonbonded interactions [47]. The bonded interactions within the GAFF force field require three main contributions: harmonic bonds, harmonic angles, and AMBER dihedrals (as seen in Figure 5.1):

$$U_{bonds} = \sum_{ij} \frac{1}{2} K_{ij}^{bond} (r_{ij} - r_{ij}^0)^2 \,, \tag{5.7}$$

$$U_{angles} = \sum_{ijk} \frac{1}{2} K_{ijk}^{angle} (\theta_{ij} - \theta_{ij}^0)^2 \,, \tag{5.8}$$

$$U_{dihedrals} = \sum_{ijkl} \frac{1}{2} K_{ijkl}^{dihedral} [1 + \cos(n\theta_{ijkl} - \theta_{ijkl}^0)] \,. \tag{5.9}$$

Here K and n are the fitting parameters of the force field, and r_{ij}^0 and θ^0 are the equilibrium distance and angles.

GAFF uses the Lennard-Jones (12-6) and Coulomb force fields for the nonbonded interactions. The Lennard-Jones parameters are expressed as:

$$U_{io} = 4\epsilon_{ij}\Big[\big(\frac{\sigma_{ij}}{r_{ij}}\big)^{12} - \big(\frac{\sigma_{ij}}{r_{ij}}\big)^{6}\Big]\,, \tag{5.10}$$

Where σ is the equilibrium distance and ϵ is the depth of the energy well, which is used to indicate the strength of the interactions. The terms raised to the power of twelve indicate repulsive forces that are more pronounced at shorter distances, and the terms to the power of six become relevant for more considerable distances, having a negative sign as an attractive force.

As mentioned above, the MAPI lattice can become distorted through temperature changes, and the MA molecule, which is in permanent rotation, creates a dipole. To account for these aspects, the BC potential is explicitly applied to the lattice interactions and the dipole, i.e. Pb/I with N/C. This allows the potential to replicate the orthorhombic, cubic, and tetragonal phases of MAPI. The lattice and H atoms interactions have a minimal effect on the material's properties, so a soft Lennard-Jones and Coulomb potential can be used for them. It is important to note that the Columbic term includes long-range interactions, but it is still important to calculate the point charges precisely using quantum chemistry principles [49]–[51].

5.3 Methodology

Use of LAMMPS software

All simulations outlined in this thesis were performed using the Large-Scale Atomic/Molecular Massively Parallel Simulator (LAMMPS) software. This software uses Newton's equations of motion and, for MAPI, the MYP potentials to create a time evolution of interacting atoms. The models built in this software account for all interatomic potentials and incorporate both long and short-range forces. All simulations were completed using a computer cluster of AMD EPYC processors 2300 MHz with an average computation time of 22 CPU hours per nanosecond.

The output given by LAMMPS can be altered to meet users' needs. This can include the temperature, kinetic energy, potential energy, enthalpy, etc for each timestep. However, in the case of our simulations, the most important output is the mean squared displacement (MSD), which is defined as:

$$\mathrm{MSD}(t) = \langle|\mathbf{r}(t) - \mathbf{r}(0)|^2\rangle = \frac{1}{N}\sum_{i=1}^{N}|\mathbf{r}_i(t) - \mathbf{r}_i(0)|^2\,, \tag{5.11}$$

where $r_i(t)$ is the position at time t of atom i. To find the evolution of movement, the MSD is proportional to the time and the diffusion coefficient D,

$$\mathrm{MSD} = 2gDt\,, \tag{5.12}$$

where g is the dimension of the space (1D, 2D, 3D). LAMMPS can monitor the MSD for all atoms within the system or a subset of atoms of interest. The subset defines the number N.

Simulation Set-Up

The LAMMPS software allows for a realistic simulation of the MAPI material using a personalized input file. The input file for our simulations contained the bonds, angles, and charge accumulation designated for each atom. The specificity of this input file is necessary to get the complicated bonded nature and rotation of the MA molecule and its charge as a cation.

As mentioned above, the MAPI system has several configurations depending on the external factors applied. For our simulations, we considered a triclinic (non-orthogonal) simulation box. This structure allows the simulation box to tilt freely, increasing the stability over a wide range of temperatures.

The boundary condition was considered to be periodic in all directions. This gives the atoms free range to exit the boundary and reenter on the opposite side. By doing this, we ensure that our system will remain in net neutrality and no atoms will be lost.

For our simulations, we implemented six types of atoms for Pb, I, N, and C. We also included two types of H atoms, dependent on whether they were bonded to N or C.

Defect-Free MAPI

We selected the lattice command's option *custom* to create an orthorhombic PbI_3 lattice. This unit cell contains 4 Pb and 12 atoms, with the c-axis in the z direction. This leaves the crystal's basal plane (ab) parallel to the xy plane. The 4 MA molecules were then inserted using the *molecules* command for the inorganic lattice and dipole orientations (Figure 5.2). Finally, we replicated our complete lattice $4 \times 4 \times 2$, giving 3072 atoms, or 64 unit cells.

Defective MAPI

Defects must be placed into the system to simulate the ionic migration within the perovskite material. Three main types of defects can instigate migrational patterns: vacancy, interstitial, and displacement. In the displacement defect, a single atom, typically iodine, is moved from its initial position and placed in a secondary location. The interstitial defect involves the placement of an additional atom, and the vacancy defect is the removal of an atom, leaving a hole in its place. The two latter defects cause the system to no longer be in net neutrality.

Previous studies have shown the basic migrational patterns that evolve through each defect [52]. This study found that the interstitial atom (Pb or I) will roam

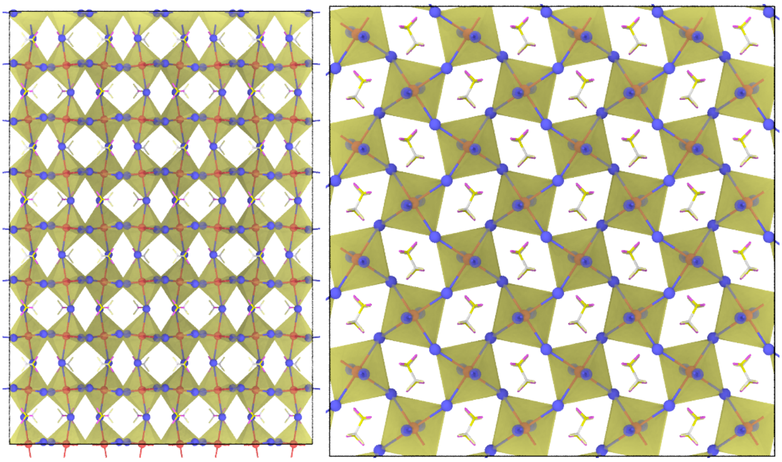

Figure 5.2: (left) *b*- and (right) *c*-axis views of the initial structure of defect-free MAPI. Each Pb atom in red is surrounded by 6 I atoms forming octahedra indicated by yellow. Note how MA molecules are oriented within empty spaces between octahedra in the c-axes view.

freely throughout the crystal lattice without bonding to an additional group (Figure 5.3). However, it did not seem to cause any detrimental effects to the lattice structure.

The displacement defect had one of two results: (1) if the displaced atom were within two unit cells of its original location, it would migrate directly back and fill the vacancy, and (2) when the displaced atom was further away, a ”domino” effect occurred. This occurs when a separate atom fills the vacancy, creating a new one; this process continues until the originally displaced atom fills the final vacancy. Figure 5.4 shows a visualization of this process.

Finally, the vacancy migrational pattern showed the same ”domino” effect. However, the vacancy traveled throughout the system and could not be suppressed, as seen in Figure 5.5 .

Initial Velocities

The initial velocities of the atoms were assigned pseudo-randomly from a Gaussian distribution to achieve the desired temperature while avoiding the introduction of linear and angular momentum to the entire system.

Force Fields

To create realistic simulations, all forces acting on all atoms in the system must be accounted for. Using the hybrid option of the pair style, multiple types of force

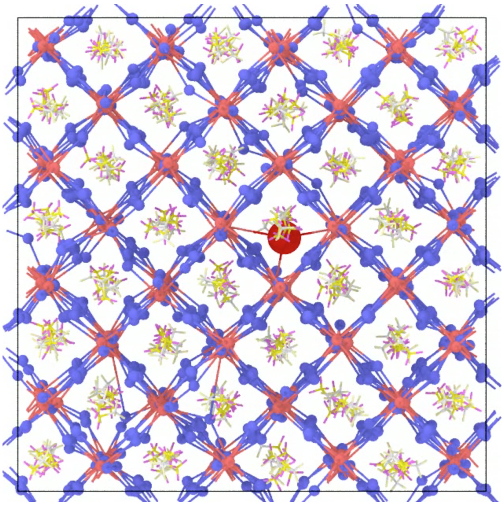

Figure 5.3: Visualization of an interstitial iodide (large red sphere) using the OVITO program.

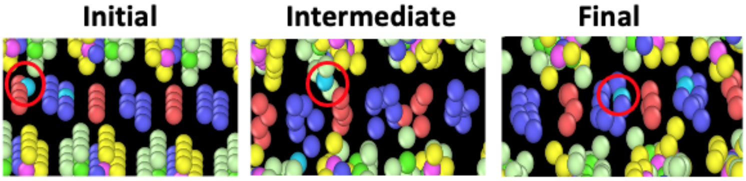

Figure 5.4: Visulaization using the OVITO software to outline the vacancy migration when the displaced iodide is within one unit cell of the vacancy. The large blue sphere between two mid-sized red ones indicates the vacancy (pseudo-particle) and under-coordinated Pb atoms, respectively.

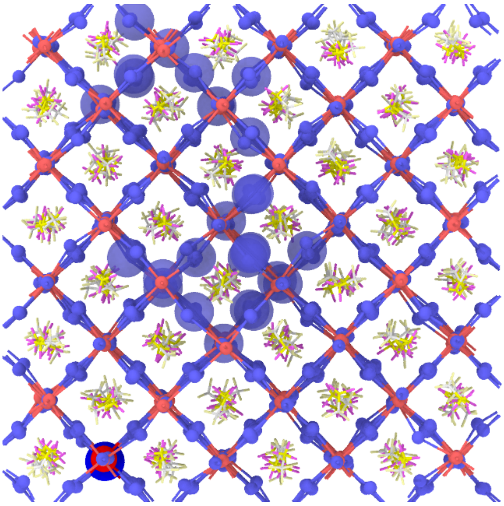

Figure 5.5: Migration of initially displaced iodide is shown by the light blue sphere within the red circle. Both blue spheres indicate iodides that take part in migration.

fields can be implemented. In our case, we combined Buckingham with long-range Coulomb potentials and CHARMM with long-range Coulomb potentials. The CHARMM style for dihedrals was used for the MA-bonded interactions to apply harmonic bonds and angles. LAMMPS must be compiled with the optional ”molecule” package to support the bonded interactions.

Using CHARMM for the pair and dihedral styles is functionally equivalent to using the Lennard-Jones pair styles and AMBER dihedral styles. However, in the case of CHARMM, LAMMPS automatically applies the standard GAFF force field weighting factors of 0.5 for Lennard-Jones and 0.8333 for Coulomb interactions between 1-4 bonded atoms.

Regarding the long-range interactions, LAMMPS must be compiled with the optional ”space” package. We employed the ”ewald/disp” kspace style, which performs standard Ewald summation while treating Lennard-Jones and Buckingham (or any attractive potential in the $1/r^6$ form) as long-range interactions without a cutoff.

The bond, angle, and dihedral styles were defined as harmonic bonds, with the force field coefficients specified in their respective sections. Finally, the charge for Coulomb interactions was set based on each atom’s mass and point charge.

Relaxation

We conducted energy minimization using the conjugate gradient algorithm, applying a force tolerance of 10^{-6} kcal/mole Å and an energy tolerance of 10^{-8} ($\Delta E/E$, unitless). The box dimensions were allowed to fluctuate during the minimization process to achieve a pressure of 1 bar. Three stages were initiated to reach equilibrium within the isothermal-isobaric (NPT) ensemble, with damping constants of 50 fs for temperature and 250 fs for pressure. The first step set the initial temperature to 1 K for five ps, the second gradually increased the temperature to 300 K for a time period of 145 ps, and finally, the third step maintained a constant 300 K for an additional 250 ps.

Seeds

Each trial was completed six times, with the seed changed each time. The seed is a pseudo-random number that alters the initial conditions slightly. By adjusting this number each run, we can ensure that our results are random or repeatable, depending on whether the seed is different or the same, respectively.

Post-Processing and Visualization

The open visualization tool (OVITO) and its Python interface were utilized for post-processing and visualization purposes. For example, the iodide vacancy must be defined by its neighbors, i.e., two under-coordinated Pb atoms. Since the vacancy is considered an ”empty space,” the MSD cannot be tracked. Thus, we utilize the visualization component of OVITO to track the trajectory of the vacancy and execute its script through the Python interface.

Chapter 6

Modeling Results

6.1 Effect of Pressure on the Dynamics of Iodide Defects in Methylammonium Lead Iodide: An Atomistic Simulation

The effects of pressure on the perovskite material have been detailed in research over the past years. These studies have shown that pressure changes in a perovskite material affect the optical, electronic, and photovoltaic properties [53]. More specifically, the changes in properties are related to the structural changes of the lattice when either tensile or compressive strain is applied.

According to Jaffe et al., applied pressure causes octahedral tilting of the perovskite lattice [54]. When compressive pressure is applied, there is an increase in orbital overlapping and a decrease in overlaying during tensile strain [54]. This overlapping directly affects the electronic band dispersion, increasing or decreasing the carrier concentration, respectively [53]. In addition, compressive strain, specifically, has been shown to cause an increase in the band gap [53]. Therefore, it may be possible to fine-tune the bandgap through control in pressure to maintain the optimal bandgap for the desired application [53].

Given the information mentioned above, we hypothesize that altering the pressure through either tensile or compressive strain may alleviate the effect of ionic migration. Specifically, the ionic migration caused by the vacancy and interstitial iodide defects is detailed in 5.3. Below is an overview of the paper reporting the results of this study.

Overview

The purpose of the paper ”Effect of Pressure on the Dynamics of Iodide Defects in Methylammonium Lead Iodide: An Atomistic Simulations” was to determine if

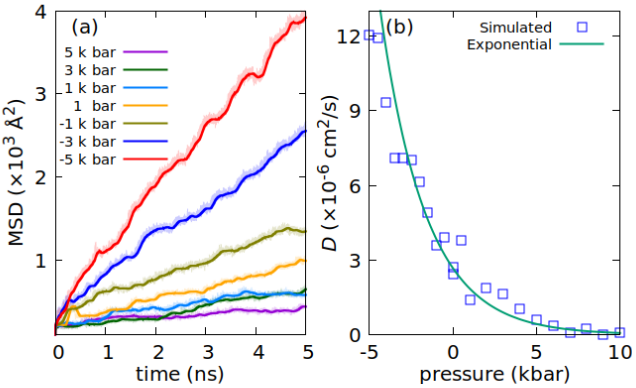

Figure 6.1: Graphical analysis of the MSD of all atoms in the system when in the presence of a vacancy. Each line indicated a change in pressure from -5000 atm to 5000 atm.

external factors, such as pressure, could suppress or mediate the effects of ionic diffusion. As discussed previously, we consider the ionic migration to be the driving factor of degradation with the MAPI perovskite. Not only does the ionic migration cause a breakdown of the perovskite crystal, but it also causes hysteretic behavior due to the accumulation of ions at the electron and hole transport layers. Within this paper, we considered both the iodine vacancy and the iodide interstitial as the driving forces of ionic migration. Both defects were studied using the perfect crystal structure. The definitions of these defects and their placement in the structure can be seen in section 5.3.

The MYP potential was utilized for all interatomic force fields in our system. To ensure our results were viable, previous studies using the MYP potential were reviewed, and our results were comparable to Mattoni et al. [47], and therefore considered repeatable. Initial testing was completed within a perfect crystal structure with an implanted defect (IVAC or Iint) with a baseline pressure of 1 atm. We tested both negative and positive pressure to understand the effects of expansion (tensile strain) and compression of the material, respectively. A time scale of 5 ns was chosen for the duration of each simulation. Figure 6.1 shows the results from the IVAC simulations. Whereas Figure 6.2, show the results from the Iint trials.

We concluded that the iodine vacancy is highly reactive to positive and negative pressures. The vacancy's mobility decreased in the presence of a positive pressure and increased when a negative pressure was applied. However, the diffusion rate of the iodide interstitial was not constant over pressure changes. Therefore, additional simulations were conducted, increasing the timescale from 5 ns to 50 ns. The longer timescale indicated that the only migration was the iodide intersti-

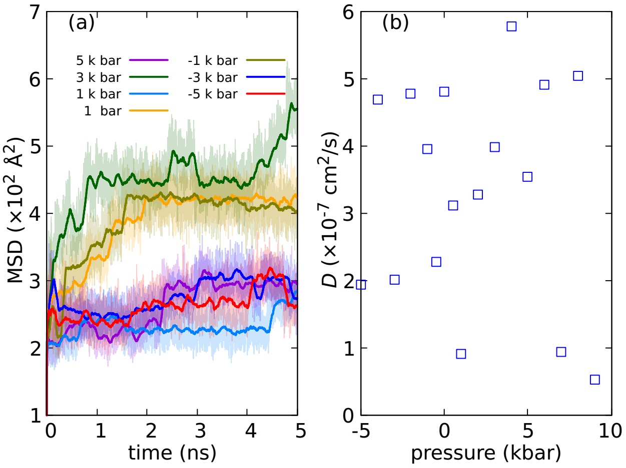

Figure 6.2: Graphical analysis of the MSD of all atoms in the system in the presence of an Iint defect. Each line represents a change in pressure from -5000 atm to 5000 atm.

tial jumping from one unit cell to another, causing limited negative results on the material.

In all, it seems any compressive strain, leading to orbital overlapping, will slightly alter the crystal structure, decreasing the iodide migration. However, it is essential to note that pressure less than -5 K bar was not tested and may lead to adverse alteration in the band alignment.

My role in this research included all computational testing of the MAPI material through the varying pressure changes and the data analysis of the MSD and vacancy migration patterns.

The published paper regarding this work can be seen in Appendix A.1.

6.2 OH- ions can reduce the iodide migration in MAPI

To the best of our knowledge, adding OH—ions to the perovskite material to suppress ionic migration is a novel idea. Although the effects of water and humidity have shown a negative impact on the perovskite material through an increase in degradation, we hypothesized that a small amount of water may help mediate or completely suppress ionic migration.

DTF studies have shown that water molecules in the MAPI perovskite dissociate at 0.75 eV in the dark and 0.57 eV in light [55]. This dissociation allows for the formation of H^+, and OH^- ions. Therefore, we can assume that when the MAPI perovskite is fabricated in the presence of low humidity, water molecules may enter the perovskite material, possibly through grain boundaries, ultimately dissociating. Due to the negativity of the OH- ions, we hypothesized that in the presence of a vacancy defect, the positive 'hole' may be drawn to the OH- ions and either fill the vacancy or halt the migration.

The results of this study can be found in the overview of the paper below.

Overview

It is known that water molecules infiltrating the MAPI perovskite material can increase the degradation rate and foster changes to the band gap. However, we hypothesized that in small amounts, the dissociated water molecules (H+ and OH−) could assist in suppressing the iodide vacancy migration. This paper was presented at the 2023 CAS conference and showcased the results of adding the hydroxyl group OH− to the MAPI perovskite material.

The methodology follows that outlined in section 5.3, including both the simulation setup and the MSD computation. Similarly to the paper outline above, the MYP potential was utilized for the MAPI perovskite crystal. We also included the TIP3P parameters to our already established force and charge parameters to add the hydroxyl group to the system. Once added, four simulations were conducted, each time changing the distance between the vacancy and the hydroxyl group. Figure 6.3 shows the MSD of all iodides in the system per trial.

Through the use of the OVITO visualization software, we were able to track both the migration of the vacancy and the hydroxyl group. Initially, we assumed that the hydroxyl group would bind to the iodide group containing the vacancy. However, we noticed that the hydroxyl group and the vacancy both migrate toward each other but do not bind. A visualization of this can be seen in Figure 6.4

DFT calculations were also conducted to ensure that the addition of the hydroxyl group did not significantly impact the band alignment or the interaction between the MAPI material and the TiO_2 electron transport layer.

Our studies concluded the hydroxyl group can mediate the migration of the iodide vacancy. The placement of the hydroxyl group tends to stay consistent

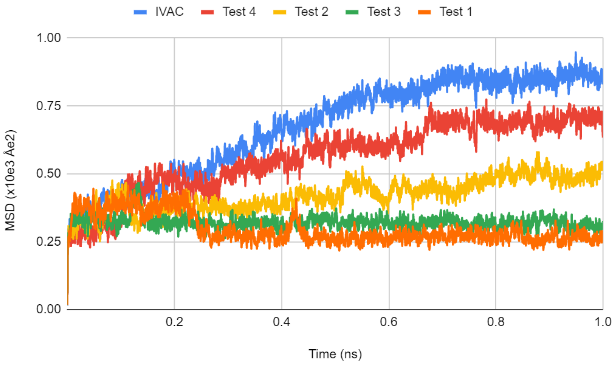

Figure 6.3: Graphical analysis of the MSD of all iodide atoms in the system when there is a vacancy defect and a hydroxyl group. Each trial indicates a further distance between the vacancy and the OH-.

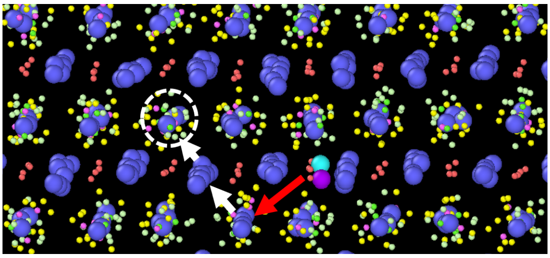

Figure 6.4: Visualization of the migration pattern of the iodides (blue spheres) and the hydroxyl group (teal and purple spheres) using the OVITO software.

throughout the simulations, and depending on the placement of the initial iodide vacancy, the vacancy will migrate toward the hydroxyl group until it is within one unit cell away. Once the vacancy is close enough to the hydroxyl group, the migration halts and remains stationary.

The DTF studies concluded that the presence of the hydroxyl group only showed a slight shift in energy, but the band alignment remained primarily unaffected. Similarly, the band aliment between MAPI and the electron transport layer remained unchanged in the presence of several OH^- molecules. Most notably, in the presence of just an iodide vacancy, there is a slight downward shift in the band alignment, and the addition of the hydroxyl group mediates this result.

Given the information presented in this manuscript, further testing should be done, including the addition of several hydroxyl groups to determine if there are any negative effects to the MAPI structure.

Regarding my role in this paper's scientific research, I included adding the OH− to our LAMMPS input file and all computational testing. I also completed the data analysis of the MSD and vacancy migrational patterns.

Further information regarding this manuscript can be seen in Appendix A.2.

6.3 Suppression of ionic migration in MAPI perovskite by OH- ions in the presence of grain boundaries

Overview

As mentioned above, the inclusion of an OH- molecule has the ability to suppress the migration of an iodide vacancy when it is in close proximity. However, the studies testing this theory only considered a perfect crystal structure [56]. It is not uncommon for the MAPI perovskite to have a grain boundary within the crystal structure. A grain boundary can be regarded as two fragmented parts of the crystal placed together. This is commonly seen in poly-crystalline solar cells. In the case of MAPI, the grain boundary may contain dangling iodide or lead atoms. These dangling atoms may cause the grain boundary to be negatively or positively charged, respectively. Due to this charge interference, the vacancy tends to migrate throughout the crystal and into the grain boundary. Therefore, the purpose of this study is to determine if the introduction of OH- molecules is able to suppress the vacancy and inhibit it from traveling toward the grain boundary.

The simulation for the perfect crystal structure can be seen in section 5.3. Once the main model was fabricated, we introduced a grain boundary into the system. This was done by rotating the crystal +/-18.5° in two grains, giving twin boundaries of $\sum 5/(120)[001]$. The grain boundaries were then shifted to give a uniform distance between them. The final product of the system is pictured in 6.5, which was created using the OVITO program.

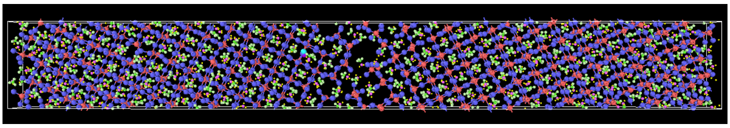

Figure 6.5: Visualization of the dangling iodide grain boundary using the OVITO software.

Once our system was created and our baseline studies of the MSD were completed, we added vacancy defects to it. Similar to our previous study, we conducted several trials, placing the OH molecule further away from the vacancy each time.

Each trial was completed five times, and the seed was varied to ensure our results were accurate and reproducible. Figure 6.6 shows the MSD of all iodide atoms within the system when the hydroxyl group was placed within one unit cell of the vacancy. This result shows that the hydroxyl group was able to fill the vacancy and surpass any further migration. The total diffusion coefficient was calculated to be 2.84×10^{-8} cm^2/s.

However, when the vacancy was placed at an equal distance between the hydroxyl group and the grain boundary, the vacancy migrated toward the grain bound-

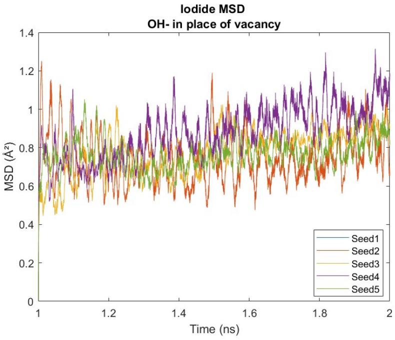

Figure 6.6: Graphical analysis of the MSD of all iodide atoms in the MAPI crystal with a grain boundary. When a vacancy is within one unit cell away from the hydroxyl group.

ary. We hypothesize this is due to a stronger polarization of the dangling iodide grain boundary. Figure 6.7, shows the increase in the MSD as the vacancy travels toward the boundary. The overall diffusion coefficient of this trial averaged 2.63×10^{-7} cm^2/s, showing an apparent increase in migration compared to the previous trial.

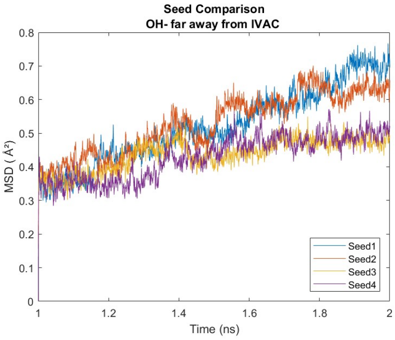

Figure 6.7: Graphical analysis of the MSD of all iodide atoms in the presence of a vacancy and a grain boundary. A single hydroxyl group was placed three unit cells away from the vacancy.

My role in this paper's research included altering our previous LAMMPS input file to include a grain boundary, all seed testing, and the data analysis, including both the MSD and the vacancy migration.

Further information regarding this paper can be seen in Appendix A.3.

Part III

Experimental

Chapter 7

MAPI and Silicon Nanowires

7.0.1 MAPI/SiNWs Heterojunctions

To the best of our knowledge, incorporating silicon nanowires and MAPI perovskite into a new photovoltaic device is a novel idea. However, the combination of silicon and MAPI in photovoltaics has been tested before. For example, Mariotti, et al. designed a complete cell of n-type silicon/MAPI/Spiro-OMeTAD/Au, where the n-type silicon worked as the electron transport layer, and the Spiro-OMeTAD acted as the hole transport layer [57]. The overall efficiency of this cell was 2.08%, with a fill factor of 38.4%. However, one issue associated with the fabrication of this cell involved the spin coating technique to deposit the perovskite material. Although the MAPI layer formed a polycrystalline layer on the silicon wafers, the layer had several defects, such as pinholes and voids [57]. The defects within the perovskite layer could potentially cause shunting throughout the MAPI layer [57]. However, the addition of the Spiro-OMeTAD may act as a pinhole blocker, reducing the risk of shunting [57].

The use of metal nanoparticles in perovskite photovoltaic devices is not a novel concept. Previous reports have noted that the addition of metal nanoparticles causes an increase in the photoresponsivity, response speed, and tuning response wavelength band [58]. However, the nanoparticle's placement within the solar cell's structure has varied throughout studies; the most common placements include doping the semiconductor material, inserting the nanoparticles between the semiconductor and electrodes, or decorating the surface of the semiconductor material [58]. In recent reports, Wang et al., suggested adding Ag nanoparticles at the interface between the bulk Si and the MAPI perovskite layer in order to increase the photoresponsivity [58]. Their testing concluded that the addition of Ag nanoparticles showed an increase in the photoresponsivity of around 10.6 times, compared to the solar cell without Ag nanoparticles [58]. In addition, the photo response speed was also increased by 7.9 times [58]. However, it should be noted that while depositing the MAPI material onto the Ag nanoparticles interface, there was an increase in pinholes with an unequal diameter throughout the material. As stated above, the pinholes may result in shunting within the MAPI material, negatively impacting the efficiency of the solar cell.

Therefore, our study suggests that instead of bulk Si being used as the semiconductor material, SiNWs could be utilized to reduce the number of pinholes in the deposition of the MAPI perovskite material while still maintaining the benefits of a silicon/MAPI heterojunction. In addition, earlier theoretical research performed by our group suggested that quantum confinement effects can influence the energy of the excitons in thin nanowires [59], [60]. The information provided below shows our case study of the addition of SiNWs.

The perovskite material requires a deposition onto a mesoporous layer in order to form an equally dispersed layer. Figure 7.1 shows an SEM scan of the MAPI perovskite deposited on a TiO_2-compact layer and a TiO_2-mesoporous layer. Due to this deposition limitation, depositing the perovskite material onto bulk silicon can be an added issue. It may result in an increase of defects (grain boundaries) and a nonuniform deposition.

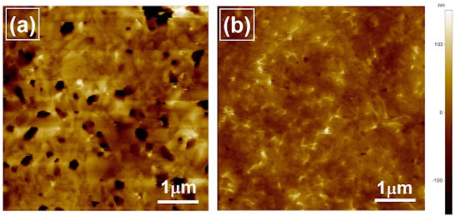

Figure 7.1: AFM image of the deposition of MAPI perovskite on TiO_2 compact (a) wherein the dark spots indicate pin-holes where the MAPI perovskite could not bind. The deposition of MAPI on a mesoporous TiO_2 layer (b) shows a uniform deposition and a clear binding with no pinholes.

Depositing the perovskite material onto silicon nanowires preserves the advantages of silicon and perovskite junctions while limiting the issues accompanying pinholes. In addition, silicon nanowires may increase photon absorption due to light refracting off the nanowires and back into the perovskite material.

7.0.2 Methology

Silicon Nanowires

The silicon nanowire substrates were prepared using the MACE procedure on polished p-type silicon wafers. Typically, the silicon nanowire substrates have a difficult reproducibility rate and are time-consuming to fabricate. To combat this, we developed what we believe to be a new recipe to speed up the process and increase reproducibility. We created a 'Batch' recipe that can manufacture a minimum of 8 substrates at a time while limiting the chance of error in chemical weight measurements.

After our silicon wafers are cut into 2x2 cm substrates, then processed through a three-cycle ultrasonic bath process: washed with isopropanol, acetone, and distilled water (DI water), and dried using N_2 gas. This process ensures that our substrates have no external debris that could affect silicon nanowire fabrication.

The 'Batch' recipe's metal catalyst solution comprises 0.255 mg $AgNO_3$ nanoparticles, 18.6 mL of 40% HF, and 81.4 mL of distilled H_2O. At the same time, the etching solution is comprised of a diluted solution of HF and H_2O_2.

After the washing cycle, each substrate is dipped into the metal catalyst solution for 30 seconds and then immersed in the etching solution for 10-20 minutes, depending on the length of wire we are testing. Once removed from the etching solution, the substrates are dipped into DI water to stop the etching process, then dipped into HNO_3 to remove the excess Ag particles. This process may be repeated twice to ensure all Ag particles are removed from the surface. Finally, the substrates are dried again, using N_2 gas.

MAPI Perovskite

The MAPI layer is prepared within a glove box and an influx of N_2 gas. We deposited the MAPI layer on the SiNWs using a two-step spin coating method. A single solution of MAPI perovskite can cover ten substrates at a time.

The MAPI layer is made using PbI_2, CH_3NH_3I, DMSO (1:1:1 molar ratio) and 600mg of DMF. The solution is then stirred for 1 hour. After this, the MAPI is deposited directly on the SiNW substrate using a spin-coater. We utilize a two-step method (1000 rpms for 10s, 4000 rpms for 30s), with the final step containing the addition of 25 μL of chlorobenzene within the last 20 seconds, acting as an anti-solvent. Finally, the freshly deposited substrates are placed on a 100 °C hotplate for 4 minutes.

Spiro-OMeTAD

The Spiro-OMeTAD layer acts as the hole transport layer and must be prepared 24 hr before deposition. Similar to the MAPI layer, we deposit the Spiro-OMeTAD using spin coating.

The Spiro-OMeTAD layer consists of 28.8 μL of 4-tert-butyl pyridine (TBP), 15.5 μL lithium bis (trifluoromethane sulfonyl) imide (li-TFSi) solution. The layer is then deposited on the MAPI layer at 4000rpm for 30 seconds.

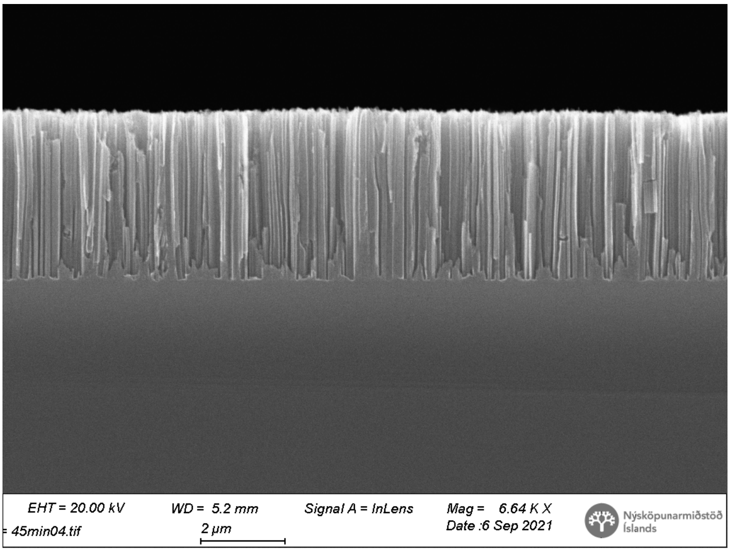

Figure 7.2: SEM cross-section analysis of silicon nanowires fabricated using the MACE procedure.

7.0.3 Preliminary results

Several trials were completed to determine which density and length of SiNWs were best to form the MAPI/silicon junctions. We determined that a 15-minute length of 7 μm was best for the deposition of the MAPI material. Figure 7.2, shows the density and length of the SiNWs before the MAPI deposition.

The thickness of the MAPI perovskite material was determined to be 550 nm, allowing for a clear separation of the junctions. Figure 7.3, show the top view of the SiNW substrates before and after the deposition of the perovskite material.

These preliminary results are promising regarding the deposition of MAPI on the complex surface of the nanowires, with good penetration of MAPI into the nanowires and presumably good contact. Regarding pinholes, the AFM images show a large reduction in these defects by incorporating the SiNWs.

However, until now, the photovoltaic effect we could observe on such a junction was minimal. We are currently working on improvements to the MAPI quality and the quality of contacts. This progress has been delayed due to several technical issues in both our labs at Reykjavik University and the University of Iceland. The presently available electrical characterization shows only a typical diode effect.

Further testing on the MAPI/SiNWs-based solar cells could be enhanced through alterations in the density or configuration of the SiNWs, which may be easily al-

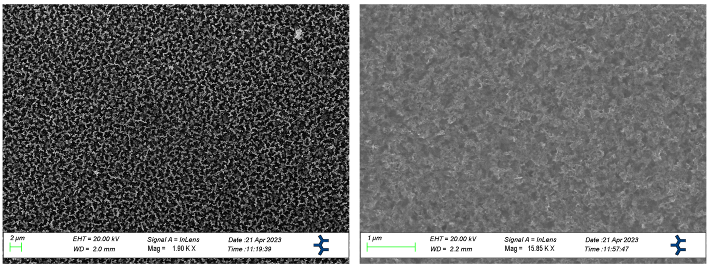

Figure 7.3: SEM top-view characterization of (left) silicon nanowires before MAPI perovskite deposition, and (right) the silicon nanowires after the deposition of the MAPI perovskite.

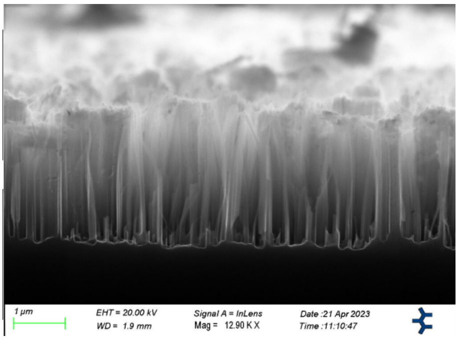

Figure 7.4: SEM cross-section characterization of the MAPI deposition onto the silicon nanowires.

tered through slight changes in the etching process. In addition, our collaborators in Romania specialize in the MAPI fabrication process, which may enhance the efficiency of the configuration.

Part IV

Silicon Nanowires as Gas Sensors

Chapter 8

Gas Sensing

While testing the resistivity of the SiNWs, we noticed that the resistivity changed significantly in the presence of human breath. Initially, we were unsure if this resulted from CO_2 or humidity. Due to this, we decided to alter our focus to the use of SiNWs for gas sensing capabilities. The following sections outline the results gathered during this experimental phase.

The idea of utilizing SiNWs for gas sensing, specifically NO_2 is not a novel idea. Previous studies have shown that periodic SiNWs can detect as low as 10 ppb NO_2 concentration [61]. However, one major issue with these SiNW-based sensors is that relative humidity concentrations above 10% cause detrimental effects on the sensibility. For example, the same study shows a decrease in sensitivity to only 500 ppm when humidity levels increased to 30%. Another example shows that when using disordered arrays, the sensitivity to NO_2 is limited to 10 ppm, but again, relative humidity concentration above 40% caused a significant loss [62]. To our knowledge, the best solution to date was Qin et al., who added an octadecyltrichkirsilane (OTS) layer on the surface of the SiNWs to block the penetration of water molecules [63]. This resulted in a device that could detect 50 ppb within 70% relative humidity [63].

Given the results listed above, the relative humidity concentration significantly impacts the sensitivity of SiNW gas sensors. However, we suggest that using a 'forest'-like structure of SiNWs, made of p-type silicon, would be able to work in high humidity concentrations without limiting the sensitivity of the device.

8.1 Ultra Responsive NO_2 silicon nanowires gas sensor

Overview

The unique and versatile properties of silicon nanowires allow for a wide range of applications across several fields of study. The main advantages of silicon nanowires

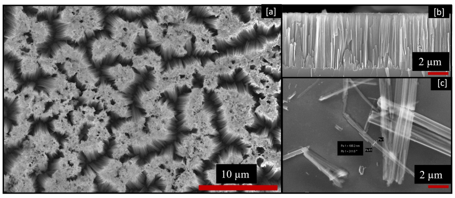

Figure 8.1: SEM images of SiNWs after a 20-minute etching time using the MACE procedure. Image (a) is the top-view of the SiNWs, showing a forest-like structure. Image (b) is the cross-sectional analysis, and image (c) shows individual wire configurations.

are their relatively simple fabrication process and large surface-to-volume ratio. In addition, they maintain a high sensitivity of current-voltage characteristics to surface states. One advantageous idea for utilizing these characteristics is using silicon nanowire-based gas sensors.

This study used the MACE procedure to fabricate p-type silicon nanowires with a 7 μm length.We analyzed our SiNWs structure through both a top view and cross-section SEM images, as seen in Figure 8.1. The top-view image shows the forest-like structure, which we believe increases the device's sensitivity through the interconnected bundles.

The SiNWs-based sensor was tested using a custom-made gas mixing system at Tübingen University with mass flow controllers (Tylan, Bronkhorst). The electrical resistance was tested using a four-wire Multimeter (Keysight 34972A), and contacts were made using copper wires and silver paste. To control the humidity, a ratio of dry air through a vaporizer filled with deionized water at 20°C was sent directly to our gas chamber. In addition, to confirm the relative humidity and concentration of NO_2 gas in the chamber, we used a commercial humidity sensor (HYT939 IST, AG) and a commercial air quality SMOX sensor (TGS2600, Figaro), respectively.

The tested gases were carbon monoxide, hydrogen, ethanol, toluene, acetone, and nitrogen dioxide, providing additional information on the cross-sensitivity. The results can be seen in Figure 8.2. To initiate our testing, we set a baseline of 0% relative humidity for two hours, then increased the humidity every half hour until the maximum humidity was reached at 80%. The process was then reversed in the same fashion.

When comparing the resistance at 0% humidity and 80% humidity, an increase of 10 Ω was seen. In addition, to ensure a steady condition, over five hours, we increased the humidity to 80%, then immediately decreased back to 0% humidity for ten cycles.

Based on this study, we concluded that our sensor was highly sensitive to hu-

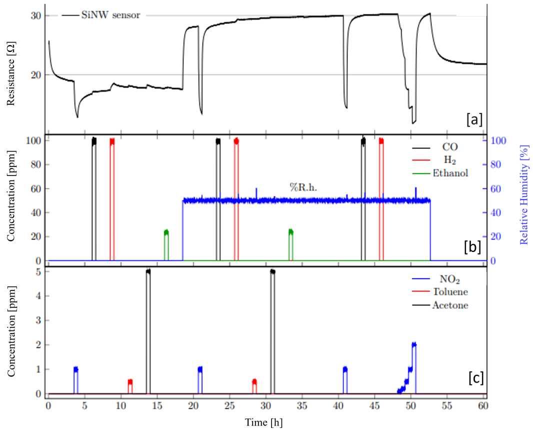

Figure 8.2: Graphical analysis of (a) the resistance change in the SiNWs sensor throughout the varying gas concentrations. Graphs (b) and (c) show the gases and varying concentrations tested.

midity and NO_2 gas. To ensure our results were accurate and reproducible, we conducted another study, testing NO_2 gas at concentrations as low as 20-200 parts per billion (ppb) while ranging the relative humidity from 0-70%. This study concluded that the silicon nanowire-based gas sensor could experimentally detect NO_2concentration as low as 20 ppb in all concentrations of the relative humidity tested. However, higher concentrations of relative humidity seemed to increase the signal strength.

We believe the mechanism allowing this high sensitivity results from the interaction between NO_2 and the silicon surface, which enables a charge transfer. The surface interactions between silicon and NO_2 are more potent than those between silicon and H_2O, so the more humidity within the system, the more water molecules can be displaced by the NO_2.

Overall, this study allowed for the production of a highly sensitive SiNW-based NO_2 gas sensor that can work under high humidity concentrations and remains stable for several years. This would enable the SiNW sensor to work in many areas, as humidity concentrations do not limit it. This sensor is cost-effective, has a simple fabrication method, and can work in various environments.

In this paper, my specific role included fabricating the SiNWs, and taking a gas sensor course at Tübingen University in Germany. While there, I participated in the testing of our SiNWs and completed the final data analysis of our results.

The final paper regarding this study can be found in Appendix B.1.

8.2 Fabrication and application of SiNWs based PANI:MO$_x$ Heterostructures for Human Respiratory Monitoring

Overview

Due to the breath-sensing capabilities discovered in our initial trials with SiNWs, we decided to investigate different ways to increase the device's sensitivity. This work was part of an ongoing project of our group to create a susceptible yet small device that could be brought into the medical field as an alternative to the current breath-sensing appliances. Specifically, the current testing of sleep apnea calls for a large mask covering both the mouth and nose in order to monitor breathing throughout the night[64], [65]. This testing may be uncomfortable to the patient, leading to an unstable sleeping pattern, which may negatively alter the results. The device we are proposing is 1 x 1 cm and can easily fit between the upper lip and nose, significantly reducing the size of the breath-sensing mechanism.

The PANI: MO$_x$ (metal oxide) layer increases the device's conductivity while also allowing for low-temperature operations and increased stability. The two types of metal oxides used in the test were titanium dioxide (TiO_2) and tungsten trioxide (WO_3). Three samples were tested, PANI, PANI: TiO_2, and PANI: WO_3. We utilized the MACE procedure to fabricate the SiNWS, the methodology of which can be seen in Section 7.0.1. The PANI layer was deposited by immersing the SiNWs into a polymer solution for 24 hours under constant stirring. The MO$_X$ were deposited similarly; however, TiO_2 and WO_3 were included in the monomer solution this time. Figure 8.3 shows the SEM characterization of each layer deposited onto the SiNWS.

Once our substrates were prepared, we tested each sample using three different breathing techniques: rapid breathing, normal breathing, and slow breathing. This allowed us to determine if the device was sensitive enough to differentiate between the varying types of breathing. Figure 8.4 shows the results of each substrate undergoing each breathing exercise. As compared to just SiNWs, the PANI:MO$_X$ layer was able to increase the overall sensitivity of the device and the response time.

This manuscript showed that the SiNWs with a PANI:MO$_X$ showed an increased sensitivity to breath sensing than just PANI or SiNWs alone. However, we also show that the addition of WO_3 had the best response to breath, and was also able to maintain a steady baseline.

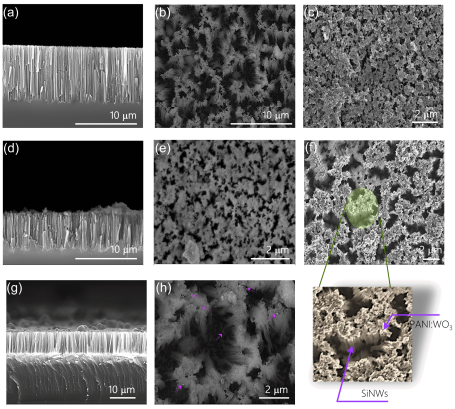

Figure 8.3: SEM characterization of the substrates used for testing. (a,b) show the cross-sectional and top-view of SiNWs structures obtained by MACE, (c) shows the top-view of SiNWs coated with just PANI, (d, e) is the cross-sectional and top-view of SiNWs coated with PANI:TiO$_2$, (f) shows the top-view of SiNWs coated with PANI:WO$_3$, along with a magnified image showing the presence of NWs and (g, h) show the cross-sectional and top-view of SiNWs spin-coated with WO$_3$.

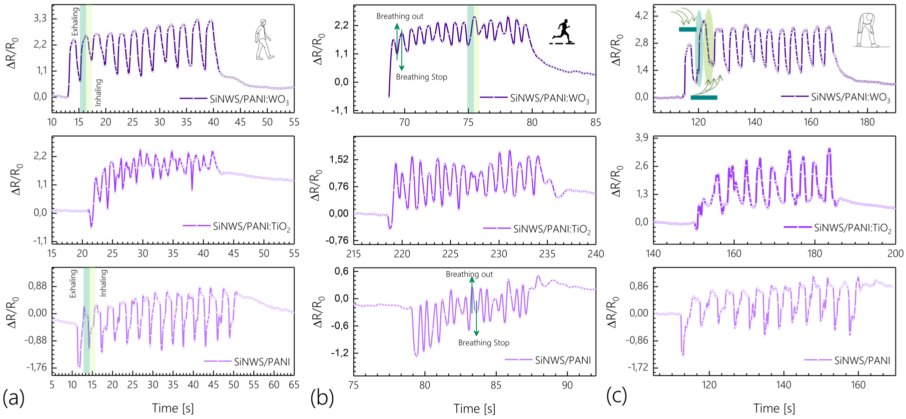

Figure 8.4: Results of the PANI:MO$_x$ substrates to varying type of breathing. From left to right, the types of breathing are rapid, normal, and slow, respectively.

My role in this paper included fabricating the SiNWS and conducting all breath tests of the variations of the MO$_x$ substrates.

Further information regarding this manuscript can be seen in Appendix B.2.

Part V

Publications

Chapter 9

Publications

9.1 Published Papers Directly Connected to This Thesis

1. Tudor Luca Mitran, **Rachel Elizabeth Brophy**, Marina Cuzminschi, Nicolae Filipoiu, Movaffaq Kateb, Ioana Pintilie, Andrei Manolescu, George Alexandru Nemnes, *Ab initio studies on perovskites*, Chapter 5 in the book Low-Dimensional Halide Perovskites: Structure, Synthesis, and Applications, Edited by Y. Zhan, M. Khalid, and N. Arshid, Elsevier ISBN: 978-0-323-88522-5, link here (2022).
2. **Rachel Elizabeth Brophy**, Movaffaq Kateb, Kristinn Torfason, George Alexandru Nemnes, Halldor Gudfinnur Svavarsson, Ioana Pintilie, Andrei Manolescu, *Effect of pressure on the dynamics of iodide defects in methylammonium lead iodide: An atomistic simulation*, The Journal of Physical Chemistry C **127**, 7938 (2023).
3. **Rachel Elizabeth Brophy**, Movaffaq Kateb, Ioan Ghitiu, Nicolae Filipoiu, Kristinn Torfason, Halldor Gudfinnur Svavarsson, George Alexandru Nemnes, Ioana Pintilie, Andrei Manolescu, *OH^- ions can reduce the iodide migration in MAPI*, 2023 International Semiconductor Conference (CAS), Sinaia, Romania, IEEE Xplore Digital Library, link here (2023).
4. **Rachel Elizabeth Brophy**, Benjamin Junker, Elham Aghabalei Fakhri, Hákon Örn Árnason, Halldór Guðfinnur Svavarsson, Udo Weimar, Nicolae Bârsan, Andrei Manolescu, *Ultra Responsive NO_2 silicon nanowires gas sensor*, Sensors and Actuators B: Chemical **410**, 135648 (2024).

9.2 Manuscript in preparation

Rachel Elizabeth Brophy et al., *Suppression of ionic migration in MAPI perovskite* *by OH^- ions in the presence of grain boundaries.*

9.3 Contributions to Other Publications on Related Research

1. Nicolae Filipoiu, Amanda Teodora Preda, Dragos-Victor Anghel, Roxana Patru, **Rachel Elizabeth Brophy**, Movaffaq Kateb, Cristina Besleaga, Andrei Gabriel Tomulescu, Ioana Pintilie, Andrei Manolescu, George Alexandru Nemnes, *Capacitive and inductive effects in perovskite solar cells: The different roles of ionic current and ionic charge accumulation*, Physical Review Applied **18**, 064087 (2022).

2. Nicolae Filipoiu, Marina Cuzminschi, Calin-Andrei Pantis-Simut, Kristinn Torfason, **Rachel Elizabeth Brophy**, Andrei Manolescu, Roxana E Patru, Cristina Besleaga, George E. Stan, Ioana Pintilie, George Alexandru Nemnes, *Impact of interface defects on the band alignment and performance of TiO/MAPI/CuO perovskite solar cells*, arXiv:2406.19594, submitted for publication (2024).

3. Muhammad Taha Sultan, Anca Dumitru, Elham Aghabalaei Fakhri, **Rachel Elizabeth Brophy**, Snorri Thor Ingvarsson, Andrei Manolescu, H Svavarsson, *Fabrication and application of SiNWs based PANI:*MO_x Heterostructures for Human Respiratory Monitoring, Journal of Semiconductors (2024). link here

Appendix A

Simulation Publications

A.1 Effect of pressure on the dynamics of iodine defects in MAPI: An atomistic simulation

Rachel Elizabeth Brophy, Movaffaq Kateb, Kristinn Torfason, George Alexandru Nemnes, Halldor Gudfinnur Svavarsson, Ioana Pintilie, Andrei Manolescu, *Effect of pressure on the dynamics of iodide defects in methylammonium lead iodide: An atomistic simulation*, The Journal of Physical Chemistry C **127**, 7938 (2023).

Effect of pressure on the dynamics of iodine defects in MAPI: An atomistic simulation

Rachel Elizabeth Brophy[1], **Movaffaq Kateb**[1,2], **Kristinn Torfason**[1], **George Alexandru Nemnes**[3,4,5], **Halldor Gudfinnur Svavarsson**[1], **Ioana Pintilie**[6], **and Andrei Manolescu**[1]

[1]Department of Engineering, Reykjavik University, Menntavegur 1, IS-102 Reykjavik, Iceland
[2]Condensed Matter & Materials Theory Division, Department of Physics, Chalmers University of Technology, SE-412 96 Gothenburg, Sweden
[3]Research Institute of the University of Bucharest (ICUB), Mihail Kogalniceanu Blvd 36-46, 050107 Bucharest, Romania
[4]University of Bucharest, Faculty of Physics, 077125 Magurele-Ilfov, Romania
[5]Horia Hulubei National Institute for Physics & Engineering, 077126 Magurele-Ilfov, Romania
[6]National Institute of Materials Physics, Atomistilor 405A, 077125 Magurele, Romania

Abstract. The diffusion of iodine defects has been considered the most important degradation mechanism of methylammonium lead iodide (MAPI) in solar cells. The present study demonstrates the importance of the pressure inside this material on the dynamics of iodine defects, using molecular dynamics simulations. It is known that the diffusion coefficient of an iodine vacancy is an order of magnitude higher than that of interstitial iodine. We show that this difference systematically increases with increased tensile strain and that both diffusion coefficients tend to zero when a compressive strain is applied. This result suggests that compression of the MAPI can be a good solution to reduce its degradation rate. Besides, the statistical aspect of deriving the diffusion coefficient from the mean squared displacement (MSD) is discussed in terms of the initial conditions (positions and velocities) of the atoms and the simulation time, considering different seeds of the pseudo-random number generator used in the simulations performed with the LAMMPS software.

1. Introduction

Methylammonium lead iodide (MAPI) [1] is a promising photovoltaic material mainly due to its low-cost fabrication and high power conversion efficiency, exceeding 24% [2]. It has a perovskite structure with $CH_3NH_3PbI_3$ stoichiometry in which the methylammonium (MA) molecule, or CH_3NH_3, has 1:1 ratio with Pb, and is located in the middle of a nearly $L1_2$ cell made of PbI_3. Then the structure polymorphism is dominated by the kinetics of MA molecules i.e. their random rotation gives cubic phase

(Pm$\bar{3}$m) while more aligned molecules lead to tetragonal (I4/mcm) and orthorhombic (P4/mbm) phases. However, the MAPI material is currently characterised by the lack of stability and relatively short lifetime in the working conditions of a solar cell. It has been found that diffusion of iodine defects is the primary degradation mechanism of MAPI cell [3–6]. Whereas during the regular working regime, the iodine migration and accumulation at the interfaces with the charge transporter layers leads to a hysteretic behavior of the current-voltage characteristic of the device [7–9].

In order to describe the behavior of the MAPI cells with atomistic simulations, and in particular the iodine migration, a simple, but useful interatomic force field, called MYP, has recently been developed [10]. This force field allows modeling several thermodynamic properties of MAPI via molecular dynamics simulations (MDS) [11]. Using the MYP potential, the variation of defect dynamics with temperature could be simulated [12], the motion of defects near grain boundaries was compared with experimental data [13], and strain introduced by an external electric field due to caloric effect has been studied [14]. It has been shown that hydrostatic pressure can affect optical, electronic, and photovoltaic properties of various hybrid perovskites [15–21]. Earlier, it had been shown that the diffusion barrier changes with variation of the lattice constant, which can be achieved by applying an external strain, or by alloying MA and I sites [22].

In the present study, we utilize the MDS method to determine the effect of pressure on the iodine defect dynamics in MAPI. We consider separately the motion of an iodine vacancy, and of an interstitial iodine ion. Apart from the presence of the defect, the MAPI material is assumed to be homogeneous.

2. Methods

We performed our simulation with the LAMMPS software package [23] which solves Newton's equation of motion based on parameterized interatomic forces, which were derived from the MYP potential [10]. The intra-MA interactions are modeled with a bounded generalized Amber force field (GAFF). Pb-Pb, I-I, Pb-I, and Pb/I-C/N interactions are considered non-bonded and modeled with Buckingham force field. Pb/I-H interactions were modeled by Lennard-Jones potential. Partial charges are assigned to each atom species and associated with pairwise Coulomb potentials. The Coulomb interaction was limited by a 10 Å cutoff, and for the residual long-range contribution, we utilized the Ewald summation with particle-particle particle-mesh (pppm) solver and accuracy of 10^{-4}.

The initial defect-free MAPI structure was considered to be orthorhombic, with a simulation cell consisting of 3072 atoms which correspond to $8 \times 8 \times 4 = 256$ cubic unit cells. We assumed the c-axis of the orthorhombic crystal in the z direction which leaves the basal plane (ab) of the crystal parallel to the xy plane, as shown in Figure 1.

The system was relaxed in three steps. First, energy minimization was performed using the conjugate gradient algorithm with a tolerance of 10^{-6} Kcal/moleÅ for the

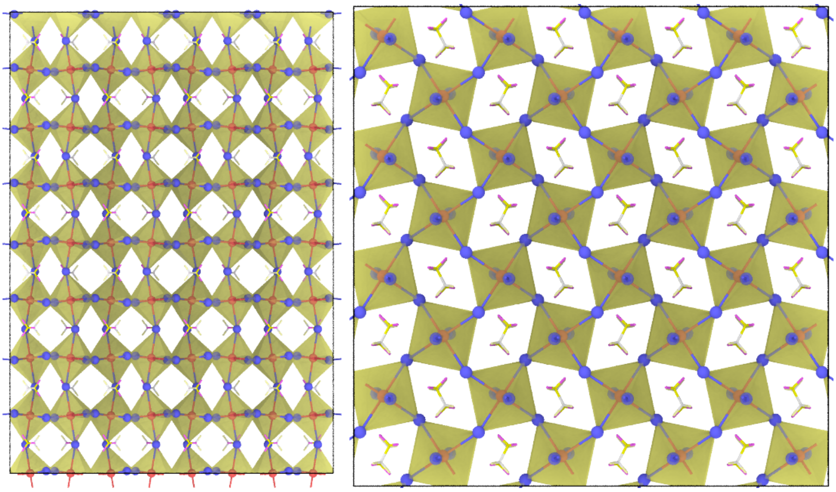

Figure 1. (left) *b*- and (right) *c*-axis views of the initial structure of defect-free MAPI. Each Pb atom in red is surrounded by 6 I atoms that together form octahedra indicated by yellow. Note, how MA molecules are oriented within empty spaces between octahedra in the c-axes view.

force, and 10^{-8} relative tolerance for the energy ($\Delta E/E$). We allowed the box dimension to vary during the minimization to produce the desired pressure, between -5×10^3 and 10^5 bar. Further relaxation was performed using the isothermal-isobaric (NPT) ensemble, by performing a temperature and pressure rescaling at each 100-th and 500-th time step (with each single step of 0.5 fs), using the Noose-Hoover thermostat and barostat, respectively. We gradually increased the temperature from 1 to 300 K within a time interval of 0.25 ns, and maintained it constant for an interval of 1.75 ns. Then, the NPT ensemble was used for the subsequent part of the simulation. The typical computational time was about 22 CPU hours for each nanosecond on a high-performance computer cluster of AMD EPYC processors 2300 MHz.

In practice, MAPI suffers from a relatively high density of various defects originating in the preparation process, most often in the original chemical solution used. In the present work, we consider two types of iodine defects: iodine vacancy and iodine interstitial. They can be generated simply by removing or adding an iodine to the lattice, respectively. They are both considered positively and negatively charged, respectively, and therefore, theoretically, these defect models may slightly violate the charge neutrality of the entire system. However, if the total number of atoms is sufficiently large, there should be no practical consequence on the atomistic simulations [12]. Instead, a paired iodine-vacancy defect can also be created by displacing an iodine from its original site to a desired distance. This model allows for maintaining the charge neutrality of the system, but it may not be viable for a long time as the pair may recombine.

In order to observe the diffusion of the iodine defects, we compute the time-dependent mean square displacement (MSD) of all iodine atoms during the simulation, which is

$$\mathrm{MSD}(t) = \frac{1}{N_I} \sum_{i=1}^{N_I} |\mathbf{r}_i(t) - \mathbf{r}_i(0)|^2 \ , \tag{1}$$

where N_I is the total number of all iodine atoms in our simulation cell, and $\mathbf{r}_i(t)$ is the position of each iodine atom, $i = 1, 2, ..., N_I$, at time t. In the absence of mobile atoms, the MSD varies only due to the local thermal vibration, with a small average over the entire simulation time. Instead, the presence of mobile defects leads to a linear trend of MSD versus time, with a positive slope. Using the random walk theory the diffusion coefficient D of the mobile defect can be calculated as [24]

$$D = \frac{1}{6} \lim_{t\to\infty} \frac{\mathrm{MSD}(t)}{t} \ . \tag{2}$$

In practice D can be obtained as the slope coefficient of the MSD versus time, divided by the factor 6, which is the double of the spatial dimension [11, 12]. The relaxation time after the initial positions, plus an additional extra time after that, is excluded from the slope calculation.

We utilized open visualization tool (OVITO) and its Python interface for the post-processing and visualization.

3. Results

3.1. Iodine vacancy

Fig. 2 shows the time dependent MSD and the corresponding diffusion coefficients D for an iodine vacancy at 300 K and different applied pressures. It can be seen that the negative pressures, corresponding to a tensile strain (and an expansion of the material), lead to an increased slope of the MSD, and of the corresponding diffusion coefficient, while in the presence of a positive pressure (or a compression of the material) the diffusion coefficient decreases, and eventually tends to zero at about 10 kbar (not shown).

The graph clearly indicates an exponential decrease of D with increasing the pressure p. A linear fit of the resulting values of the diffusion coefficient of the iodine vacancy, on the log scale, yielded an R-squared coefficient of 0.92. The corresponding solid line shown in Fig. 2(b) is the resulting fitting function, $2.67 \times 10^{-6} \exp(-0.364p)$. At atmospheric pressure our diffusion coefficient is 2.42×10^{-6} cm^2/s, close to the value reported by Delugas et al., which is $4.3{\times}10^{-6}$ cm^2/s, obtained at 300 K, but using the canonical thermodynamic ensemble, NVT, implemented in the DL_POLY molecular simulation package [12]. The decrease of the MSD and of the diffusion coefficient with increasing the pressure can be associated with the increase of the density of the MAPI material, leading to a blocking of the iodine atoms at their original sites, or to an increase of the energy they need for jumping into the nearby vacancy.

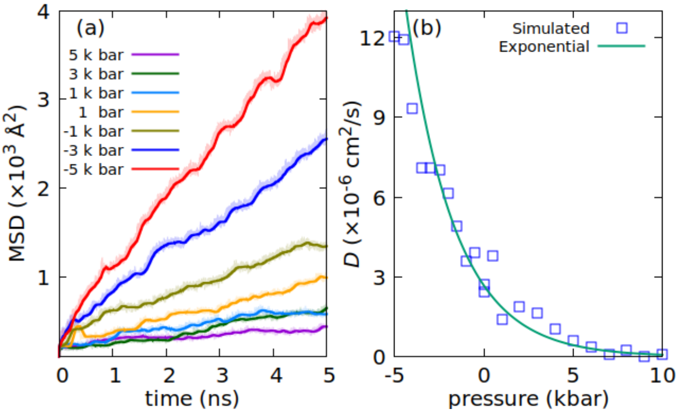

Figure 2. (a) MSD of iodine vacancy at 300 K and different pressures. The lines show a smeared MSD using 2000 time points, while the original data is shown as a shaded area around the lines. (b) Variation of D with pressure, for more values of the pressure, the solid line being the exponential fit mentioned in the main text.

As we can see in Fig. 2(a), the instantaneous time derivative of the MSD, $d(\mathrm{MSD})/dt$, is not a smooth function of time. For this reason, for a reasonably accurate estimation of the diffusion coefficient D, a simulation time longer than the average oscillation time of the MSD slope is needed, and apparently a total time of several ns should be sufficient. However, the observable variation of the slope, over shorter time intervals, also suggests that the MSD evolution may depend on the initial conditions. To check that we repeated the simulations by changing the seed of the (pseudo)random number generator in LAMMPS, which implies different initial states of the entire lattice at the beginning of the simulation, and also after the relaxation phase, and consequently different trajectories of the entire system in the phase space. In addition, we also used different (random) initial placements for the vacancy.

Fig. 3(a,c) shows the MSD results for the iodine vacancy with different seeds at 1 bar and 5 kbar, respectively. In both cases, the initial positions of all atoms were the equilibrium positions plus random displacements with $-0.1 < \delta < 0.1$ Å in each direction x, y, z, depending on the seed. The initial velocities of the atoms were also assigned randomly, from a Gaussian distribution, again depending on the seed. Thus, all simulations began with different initial conditions. Additionally, in Fig. 3(a,c) the iodine vacancy had the same initial position, whereas in Fig. 3(b,d) this position was also randomized. Clearly, the effect of the seed creates significant variations of the slope. This is evident at both pressures used. We can also see that at the higher pressure, of 5 kbar, the slope is systematically reduced, in agreement with the previous result that the diffusion of iodine vacancies is suppressed at elevated pressures.

In the nine simulations represented in Fig. 3 (a), at 1 bar, the slope coefficients are, in increasing order: 96, 104, 151, 159, 163, 179, 189, 204, 229 Å^2/ns, with a mean value of 164 Å^2/ns and a standard error (or statistical uncertainty) of about 14 Å^2/ns,

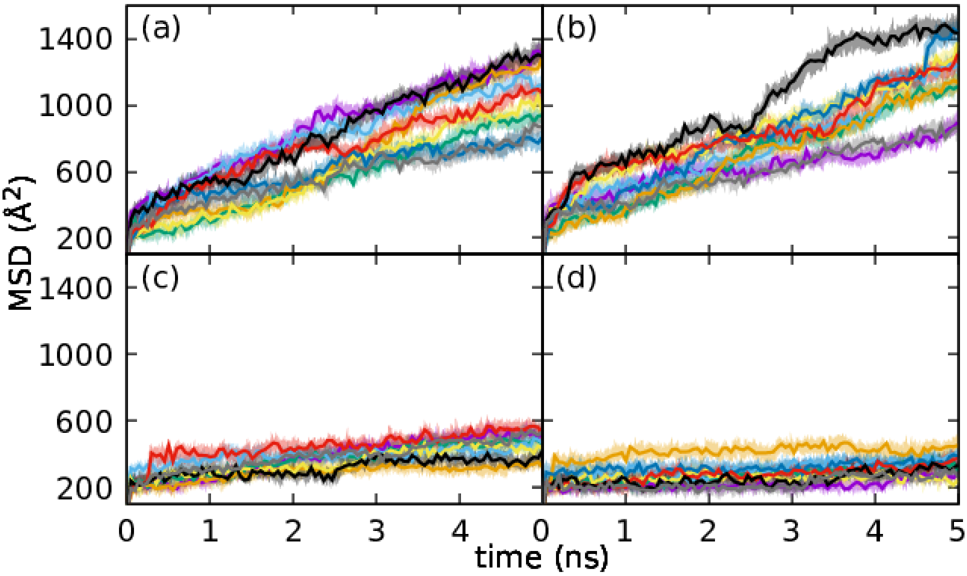

Figure 3. (a) The MSD in the presence of an iodine vacancy, at pressure 1 bar, using different seeds of the random number generator, and (b) using also different initial positions of the vacancy. (c,d) The same at pressure 5 kbar. The temperature was fixed at 300 K.

meaning ±9% relative uncertainty for the estimated diffusion coefficient. With the data obtained at 5 kbar the relative uncertainty of D is about ±15%. At the same time the uncertainty of the slope coefficient corresponding to a single simulation is much smaller, in the range 0.1–0.3%, or less, because it is based on a sample with millions of time points.

Therefore, it turns out that each single run of several ns does not include sufficient information about the distribution of all possible states of the system in the phase space. This is true because the slope coefficients obtained with 4 ns simulations differ from their mean values obtained with different initial conditions. It is also seen in our figures that the slope of the MSD vs. time changes on intervals of the order of 1 ns or less. Similar slope variations can also be observed in the calculations of Delugas et al., in their Figure 3, representing the MSD data for iodine vacancy and iodine interstitial at different temperatures [12]. Our interpretation is that a computational time of several ns is not sufficient to observe the ergodic behavior of our system, i.e. the convergence of the time-averaged and phase space-averaged values of the diffusion coefficient. For that purpose an unrealistically long computational time might be necessary, or, instead, a reasonable accuracy could be achieved with shorter simulations with different initial conditions. Long time memory of initial conditions in a diffusion process has also been addressed by other studies, and formulated in on a rigorous mathematical background [25]. However, such fundamental aspects of statistical mechanics are beyond the scope

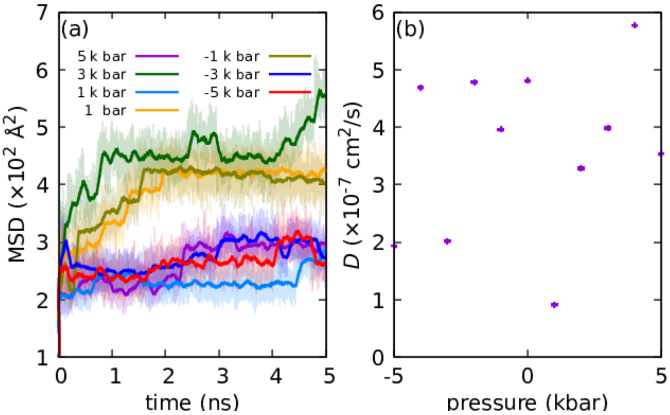

Figure 4. (a) MSD of charged iodine interstitial at 300 K and different pressures. Darker lines indicate moving average of 2000 points while the original data are shown with lighter colors in the background. (b) Variation of D with pressure.

of our present work, rather based on an empirical approach.

3.2. Iodine interstitial

Now we consider an interstitial iodine ion (i.e. an iodide) added to the MAPI lattice, and repeat the previous simulations. The results are shown in Fig. 4, obtained with the NPT ensemble, at different pressures. As before, the MSD corresponds to all iodine atoms, and the diffusion coefficient of the interstitial ion is found from the slope of the MSD. Note that the scale of the diffusion coefficient D is an order of magnitude smaller than in the case of the vacancy, Fig. 2(b). Again, we are close to the value previously reported by Delugas et al., of $7.4{\times}10^{-7}$ cm^2/s, obtained using the NVT ensemble at 300 K [12]. We also find out that the diffusion coefficient of the interstitial iodide is at least one order of magnitude smaller than that of the vacancy at atmospheric pressure.

However, in the iodide case, we could not find a systematic variation of the diffusion coefficient with the applied pressure. The values shown in Fig. 4(b) are scattered, and probably not convergent after 5 ns simulation time. The slope of the MSD data now looks variable over larger time intervals than in the case of the vacancy. And, as expected, by repeating the simulations with different seeds of the random number generator, the overall slope of MSD with respect to time is systematically smaller than in the case of the iodine vacancy, and possibly with a larger uncertainty.

The results obtained with different seeds, for pressures of 1 bar and 5 kbar, are shown in Fig. 5. It is clearly seen that when a defect is introduced in the same place, Fig. 5 (a,c), the MSD data look similar, and nearly flat. However, as can be seen in Fig. 5 (b,d), introducing the defect elsewhere might lead to a different MSD data, but their slope being always much smaller than in the case of the vacancy. Nonetheless, pressure seems to have a minor effect in these MSDs, indicating that iodide diffusion is

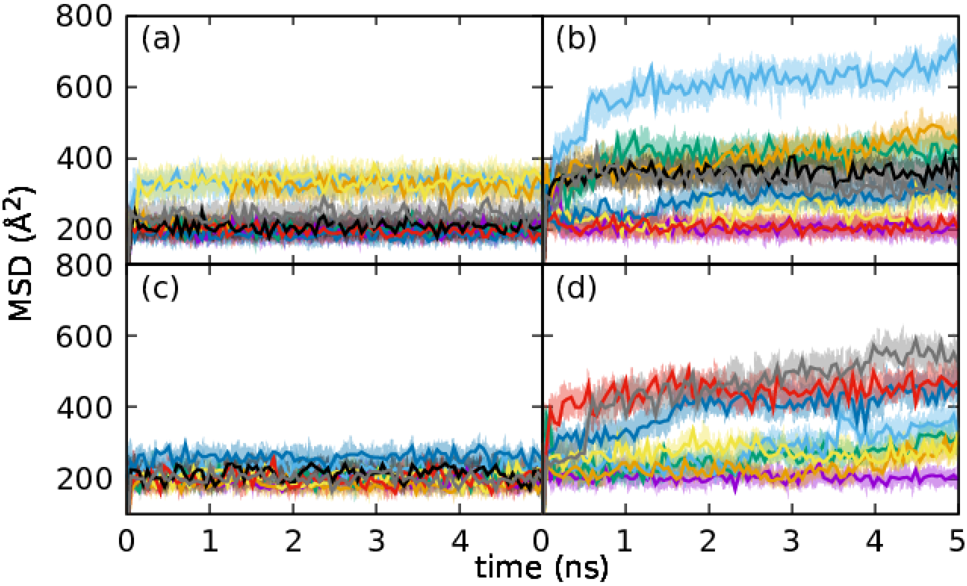

Figure 5. Variation of the MSD for the negatively charged iodine (iodide) interstitial with the seed of the random numbers. (a,b) correspond to 1 bar and (c,d) to 5 kbar pressure. In (a) and (c) the initial position of the iodide was the same, whereas in (b) and (d) it was randomized.

a less frequent event, at least up to a pressure of 5 kbar, which was our largest value.

To clarify these results, ten times longer simulations were performed for the case with the interstitial iodide, at four different pressure values. The resulting MSDs are shown in Fig. 6. Note that the results corresponding to different pressures are shifted vertically, for illustration purposes. At this time scale, for all pressure values, we can only identify jumps of the MSD, on the background of all iodine atoms' back-and-forth movements or local vibrations. The jumps are of approximately $\sqrt{\mathrm{MSD}} \approx \sqrt{100} = 10$ Å, which correspond to the size of a unit cell. So at this time scale, no net motion of the iodide can be identified, but only hopping events from one unit cell to another, which appear to be more frequent at high negative pressures such as -5 kbar, than at positive pressures.

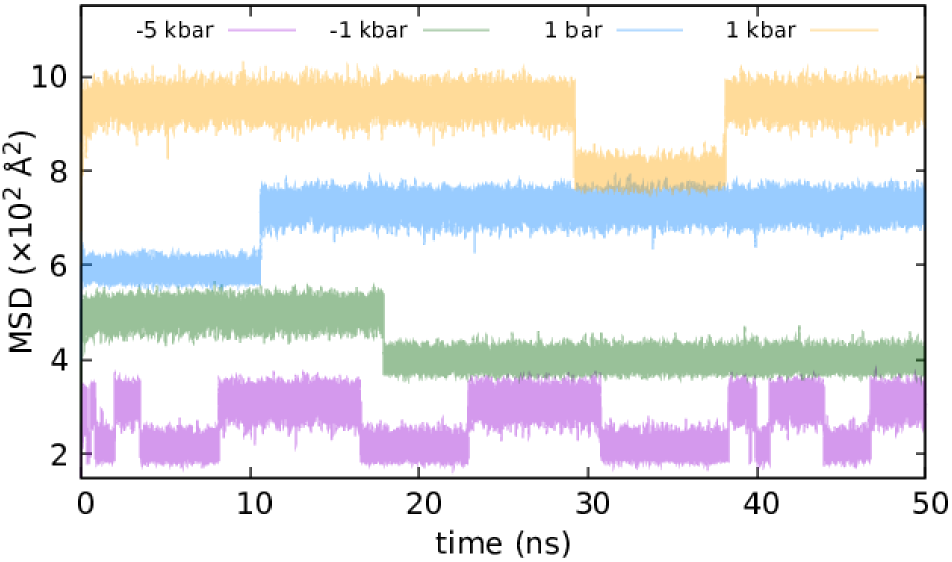

Figure 6. MSD of iodine interstitial at different pressures obtained over 50 ns time scale. The curves are shifted manually for clarity.

4. Conclusions

We performed molecular dynamics simulations of the iodine migration in the MAPI material, using the LAMMPS software, over time intervals from a few to a few tens of ns, and we obtained estimated values of the diffusion coefficients of the iodine vacancies and interstitial atoms, for different negative and positive pressures applied to the MAPI material. Our simulations show that the iodine vacancy has a diffusion coefficient, or, equivalently, a mobility, that depends significantly on the pressure. The mobility of the vacancy varies exponentially with the pressure, increasing in the presence of a tensile stress (negative pressure compared to the atmospheric value), and decreasing in the presence of a compressive stress (positive pressure). For the same conditions, the mobility of an interstitial iodine negative-ion (or iodide) is at least one order of magnitude lower, which means that the net, macroscopic, iodine migration can be associated with the diffusion of the iodine vacancies. Therefore the migration of the iodine atoms, which is a major factor in the degradation of the MAPI material, could be suppressed, or at least reduced, by applying to the material a compressive stress of the order of a few kbar.

Recent studies also suggested that with even larger pressures, of the order of hundreds of kbar, the band gap can also be modified, although achieving such pressures could be technically difficult, and could possibly lead to phase transitions of the MAPI material [26–28].

In our simulations we assumed a homogeneous MAPI lattice, and no external electric field. The presence of lattice defects such as grain boundaries can change the physical conditions. The local electric field may attract the ionic defects towards the grain boundaries [13], inhibiting further their diffusion. However, the iodine migration may still occur at the contact between the MAPI material and another layer, for example the hole transporter made of Spiro-OMeTAD [6].

Acknowledgment

The research leading to these results has received funding from the EEA Grants 2014–2021, under Project contract no. 36/2021 (project code: EEA-RO-NO-2018-0106) and from the Core Program 2019–2022 (contract 21N/2019). REB is thankful for partial support from the National Power Company of Iceland (Landsvirkjun) via the Sustainability Institute and Forum (SIF) of Reykjavik University. The computational resource was sponsored by EGI and the EGI-ACE H2020 project (GA no. 101017567) with the dedicated support of CLOUDIFIN.

Appendix A. Time dependent fluctuations of the diffusion coefficient

In a more rigorous treatment than ours, the single atom diffusion coefficient is given by the velocity auto-correlation function [24]

$$D_i = \frac{1}{3}\int_0^\infty \mathrm{d}t\Big\langle v_i(t).v_i(0)\Big\rangle \ , \tag{A.1}$$

where 3 is the number of degrees of freedom (the 3D physical space), $v_i(t)$ velocity of particle i, and the angular brackets denote the statistical average. However, in practice this method gives some level of background noise fluctuations. Therefore, the corresponding Einstein relation that can be valid at a very long time is preferred [24], which leads to

$$2tD_i = \frac{1}{3}\Big\langle |\mathbf{r}_i(t) - \mathbf{r}_i(0)|^2\Big\rangle_t \ , \tag{A.2}$$

where $\mathbf{r}_i(t)$ is the particle position. Here, the angular brackets correspond to the time averaged mean-squared displacement, which is another form of Eq. (2) from the main text.

In practice, there exist two approaches for calculation of the diffusion coefficient for defects. The first approach requires the calculation of the coordination number. Then a vacancy or interstitial is associated with a dummy particle located as the center of mass of the under- and over-coordinated atoms, respectively. For instance Pb has coordination number of six within the defect-free MAPI structure. Thus, two under- and over-coordinated Pb (i.e. with 5 or 7 neighbors, respectively) represent a iodine vacancy and interstitial, respectively [12]. This method, however, is very sensitive to the definition of cutoff for finding nearest neighbors and lattice vibration may introduce a considerable noise in determining coordination number. Thus the second approach is

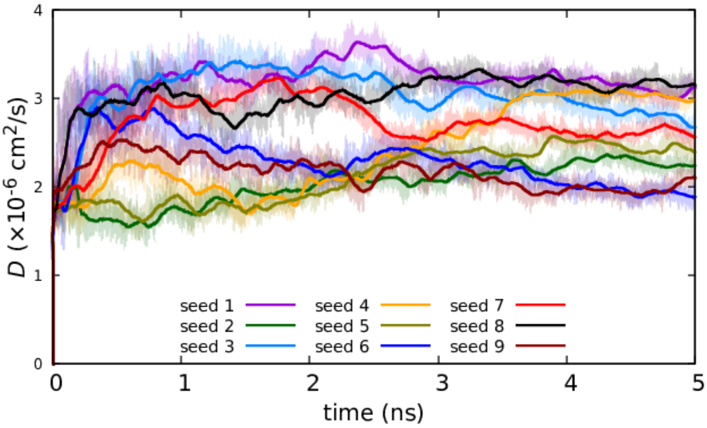

Figure A1. Instantaneous diffusion coefficient for different seeds and a fixed position of the iodine vacancy at 300 K and 1 bar. The darker lines show moving average of 2000 points while the data is plotted with lighter colors.

based on the existing particles rather than a dummy one. For example the movement of an iodine vacancy is associated with the hopping of the nearby iodines into it. Thus, it is possible to calculate the MSD of defect through the MSD of all iodine atoms. It is worth mentioning that the MSD can be summed over a group of particles and averaged over the number of particles. For the defect these averaged values must be multiplied by the number of particles [29] i.e.

$$\mathrm{MSD}(t)_{\mathrm{defect}} = N \times \mathrm{MSD}(t)_{\mathrm{total}} \ , \tag{A.3}$$

with N being total number of atoms defining the defect, which in our study are the iodine atoms.

In Fig. A1 we show the time averaged values of the D coefficient for the iodine vacancy, averaged over 2000 samples with time between samples being 100 time steps, where we can see the fluctuations during each simulation, and also for different initial conditions imposed by the initial values of the random number generator. This graphs show again that at this time scale the diffusion coefficient of vacancies has a distribution whose standard deviation is about 30%-50% of the mean value. It is (presumably) a normal distribution, because each D value has been obtained as a sample mean.

References

[1] Kojima A, Teshima K, Shirai Y and Miyasaka T 2009 Journal of the American Chemical Society **131** 6050–6051 pMID: 19366264 (*Preprint* `https://doi.org/10.1021/ja809598r`) URL `https://doi.org/10.1021/ja809598r`

[2] National Renewable Energy Laboratory (NREL) Best research-cell efficiency chart (accessed April 2nd 2022) URL `https://www.nrel.gov/pv/cell-efficiency.html`

[3] Sanchez R S, Gonzalez-Pedro V, Lee J W, Park N G, Kang Y S, Mora-Sero I and Bisquert J 2014 J. Phys. Chem. Lett. **5** 2357–2363

[4] Eames C, Frost J M, Barnes P R, O'regan B C, Walsh A and Islam M S 2015 Nature communications **6** 7497

[5] Li C, Tscheuschner S, Paulus F, Hopkinson P E, Kießling J, Köhler A, Vaynzof Y and Huettner S 2016 Advanced Materials **28** 2446–2454

[6] Besleaga C, Abramiuc L E, Stancu V, Tomulescu A G, Sima M, Trinca L, Plugaru N, Pintilie L, Nemnes G A, Iliescu M, Svavarsson H G, Manolescu A and Pintilie I 2016 J. Phys. Chem. Lett. **7** 5168–5175

[7] Tress W, Marinova N, Moehl T, Zakeeruddin S M, Nazeeruddin M K and Grätzel M 2015 Energy Environ. Sci. **8** 995

[8] Zarazua I, Bisquert J and Garcia-Belmonte G 2016 The Journal of Physical Chemistry Letters **7** 525

[9] Nemnes G A, Besleaga C, Tomulescu A G, Pintilie I, Pintilie L, Torfason K and Manolescu A 2017 Sol. Energy Mater. Sol. Cells **159** 197 – 203 ISSN 0927-0248

[10] Mattoni A, Filippetti A, Saba M I and Delugas P 2015 The Journal of Physical Chemistry C **119** 17421–17428

[11] Mattoni A, Filippetti A and Caddeo C 2017 Journal of Physics: Condensed Matter **29** 043001

[12] Delugas P, Caddeo C, Filippetti A and Mattoni A 2016 The Journal of Physical Chemistry Letters **7** 2356–2361 URL `https://doi.org/10.1021/acs.jpclett.6b00963`

[13] Phung N, Al-Ashouri A, Meloni S, Mattoni A, Albrecht S, Unger E L, Merdasa A and Abate A 2020 Advanced Energy Materials **10** 1903735

[14] Liu S and Cohen R 2016 The Journal of Physical Chemistry C **120** 17274–17281

[15] Kong L, Liu G, Gong J, Hu Q, Schaller R D, Dera P, Zhang D, Liu Z, Yang W, Zhu K et al. 2016 Proceedings of the National Academy of Sciences **113** 8910–8915

[16] Jaffe A, Lin Y, Beavers C M, Voss J, Mao W L and Karunadasa H I 2016 ACS central science **2** 201–209

[17] Jaffe A, Lin Y and Karunadasa H I 2017 ACS Energy Letters **2** 1549–1555

[18] Liu G, Kong L, Gong J, Yang W, Mao H k, Hu Q, Liu Z, Schaller R D, Zhang D and Xu T 2017 Advanced Functional Materials **27** 1604208

[19] Wang P, Guan J, Galeschuk D T, Yao Y, He C F, Jiang S, Zhang S, Liu Y, Jin M, Jin C et al. 2017 The Journal of Physical Chemistry Letters **8** 2119–2125

[20] Postorino P and Malavasi L 2017 The journal of physical chemistry letters **8** 2613–2622

[21] Ghosh D, Aziz A, Dawson J A, Walker A B and Islam M S 2019 Chemistry of Materials **31** 4063–4071

[22] Yang D, Ming W, Shi H, Zhang L and Du M H 2016 Chemistry of Materials **28** 4349–4357

[23] Plimpton S 1995 Journal of computational physics **117** 1–19

[24] Allen M P and Tildesley D J 1989 Computer simulation of liquids (Oxford: Oxford university press) ISBN 0198556454 URL `https://udel.edu/ arthij/MD.pdf`

[25] Banerjee T, Jack R L and Cates M E 2022 Phys. Rev. E **106**(6) L062101 URL `https://link.aps.org/doi/10.1103/PhysRevE.106.L062101`

[26] Rajeswarapalanichamy R, Amudhavalli A, Padmavathy R and Iyakutti K 2020 Materials Science and Engineering: B **258** 114560

[27] Faghihnasiri M, Beheshtian J, Shayeganfar F and Shahsavari R 2020 Phys. Chem. Chem. Phys. **22** 5959–5968

[28] Lee J H, Jaffe A, Lin Y, Karunadasa H I and Neaton J B 2020 ACS Energy Letters **5** 2174–2181

[29] National Institute of Standards and Technology (NIST) iprPy high-throughput computational framework description (accessed April 2nd 2022) URL `https://www.ctcms.nist.gov/potentials/iprPy/`

A.2 OH$^-$ ions can reduce the iodide migration in MAPI

Rachel Elizabeth Brophy, Movaffaq Kateb, Ioan Ghitiu, Nicolae Filipoiu, Kristinn Torfason, Halldor Gudfinnur Svavarsson, George Alexandru Nemnes, Ioana Pintilie, Andrei Manolescu, OH$^-$ ions can reduce the iodide migration in MAPI, 2023 International Semiconductor Conference (CAS), Sinaia, Romania, IEEE Xplore Digital Library, link here (2023).

OH^- ions can reduce the iodide migration in MAPI

R. E. Brophy*, **M. Kateb**†, **I. Ghitiu**‡§, **N. Filipoiu**$^{\ddagger\|}$, **K. Torfason***, **H. G. Svavarsson***,
G. A. Nemnes$^{\ddagger\P\|}$, **I. Pintilie****, **A. Manolescu***

Email: Rachel18@ru.is
*Department of Engineering, Reykjavik University, Menntavegur 1, IS-102 Reykjavik, Iceland
†Department of Physics, Chalmers University of Technology, SE-412 96 Gothenburg, Sweden
‡University of Bucharest, Faculty of Physics, 077125 Magurele-Ilfov, Romania
§National Institute for Laser, Plasma and Radiation Physics, 077125 Magurele-Ilfov, Romania
¶Research Institute of the University of Bucharest (ICUB), Mihail Kogalniceanu Blvd 36-46, 050107 Bucharest, Romania
$^\|$Horia Hulubei National Institute for Physics & Engineering, 077126 Magurele-Ilfov, Romania
**National Institute of Materials Physics, 077125 Magurele-Ilfov, Romania

***Abstract*—One of the main degradation mechanisms of methylammonium lead iodine (MAPI), which is an important material for perovskite based solar cells, is the migration of iodide ions. It is believed that this phenomenon is in fact dominated by the diffusion of iodide vacancies. In this paper, we suggest that the addition of a small amount of OH^- ions can help suppress the migration of iodide and increase the overall stability of the material. Through the use of molecular dynamics simulations, we show that the OH^- ions can bind to the positively charged iodide vacancies and can block the access of the negative iodide ions into those vacancies.**

***Index Terms*—MAPI material, iodide migration, molecular dynamics simulations**

I. INTRODUCTION

The hybrid organic-inorganic perovskite materials, and in particular the methylammonium lead iodine ($CH_3NH_3PbI_3$, or MAPI), have become a significant topic of interest in the last decade due to their photovoltaic properties. Since 2013, perovskite based solar cells have increased in efficiency from 13% to roughly 25%, making this category one of the fastest-growing photovoltaic devices. The main interest in the perovskite material is that it is able to convert light into electricity within its natural structure, significantly lowering the manufacturing costs [1], [2]. Also adding to the lower manufacturing cost is that it only requires modest fabrication equipment, much simpler than needed for conventional silicon-based solar cells. However, the perovskite based solar cells have the disadvantage of a limited stability. One main reason for that is the degradation caused by ionic migration within the perovskite material, especially the diffusion of iodide [3], [4]. Another consequence is a long relaxation time of the photo-induced current leading to a hysteresis of the current-voltage characteristic when the voltage is varied in time [5]–[8].

Quantitative data about the dynamics of the iodide diffusion is difficult to extract from experiments since it depends on several factors, such as temperature, boundaries, various types of defects, intrinsic electric field, etc. Nevertheless, molecular dynamics (MD) simulations have shown that, at least in the homogeneous MAPI material, the dominant diffusion mechanism is the migration of the iodide vacancies, with an estimated diffusion coefficient between $2.5-4.3\times10^{-6}\ \mathrm{cm}^2/\mathrm{s}$, whereas the diffusion coefficient of iodide interstitial ions is smaller by one order of magnitude or more [9], [10]. Hence, since the iodide ion is negative, once an iodide vacancy is formed, it will be positively charged, and a nearby iodide will migrate toward it and attempt to fill it up, and simultaneously creating a new vacancy. Therefore, since the vacancy appears to move faster than the iodide ion, it is tempting to think that blocking the vacancy would reduce the overall diffusion of the iodide.

Another known cause of degradation of the perovskite-based solar cells is the introduction of humidity (water) into the device. Water molecules can have multiple effects. Depending on the amount of H_2O molecules, the absorption factor may significantly decrease [11], iodide ions may be dislocated [12], and other detrimental phenomena may occur. Still, a small amount of water can be beneficial for the photovoltaic properties, for example by delaying the electron-hole recombination events [13], with negligible changes of the band gap [12].

Atomistic calculations based on the density functional theory (DFT) have shown that the dissociation of a water molecule into H^+ and OH^- ions in MAPI requires an energy of 0.75 eV in dark, and 0.57 eV in the presence of photo generated electrons [14]. Therefore, if a small amount of water is present in the light-harvesting perovskite material, we can assume the existence of some OH^- (hydroxyl) ions therein. One possibility can be that the hydroxyl is generated at the surface and enters in MAPI along grain boundaries. Another possibility is a controlled adsorption during the preparation of MAPI. Other ways to obtain OH^- in MAPI may also exist.

In this paper we use MD simulations to show that an OH^- interstitial can reduce the migration of the iodide ions inside MAPI, by binding to an iodide vacancy, and blocking the path of the iodide ions through that site. We have also tested, using density functional theory (DFT) based calculations, that the presence of hydroxyl ions at the interfaces of MAPI with the electron and hole transporter materials (TiO_2 and Cu_2O, respectively) does not have a significant effect on the energy gaps and band alignment.

II. METHODS

We utilize MD simulations to describe the movement of all atoms in the MAPI system. The simulations were performed using the LAMMPS software package [15] which solves Newton's equations of motion for each atom or molecule, based on interatomic effective forces. We used the perovskite structure with $CH_3NH_3PbI_3$ stoichiometry in which the methylammonium (MA) molecule has a 1:1 ratio with Pb, and is located in the middle of a cubic cell (or cage) made of PbI_3.

To describe the interatomic forces we used the MYP potential derived by Mattoni et al. [16]. This potential considers bonded interactions in MA and non-bonded for the PbI cage and PbI–MA link. This combination allows the computation of the local movement or diffusion of all iodide, lead, and MA constituents. The random rotation of the MA molecule at 300 K gives a cubic phase. The intra-MA interactions were modeled using a bounded generalized AMBER force field (GAFF), and the Buckingham force field was used for Pb-Pb, I-I, Pb-I, and Pb/I-C/N interactions Pb/I-H interactions were modeled with Lennard-Jones potential. For the hydroxyl we used TIP3P parameters with charges -0.8476 and 0.4238 e on O and H, respectively. This gives the hydroxyl group a total -0.4238 e as compared to +1.13 e for iodide vacancy.

The simulated system was made of 256 unit cells ($MAPbI_3$), with a total of 3072 atoms, which were relaxed by energy minimization followed by ramping up and maintaining its temperature at 300 K and the constant pressure of 1 bar for 1 ns. This produces samples from an isothermal-isobaric (NPT) ensemble controlled by the Nose-Hoover thermostat and barostat. Once the system was relaxed, a single iodide was removed, theoretically making the system positively charged. However, due to the large size of the system, there are no artificial implications on the simulations. To see if there was a way to mediate the migration, the hydroxyl group was placed within the system at varying positions and distances from the initial vacancy, and each case was run as a separate simulation. The positions of all iodine atoms in the NPT ensemble as function of time were recorded during each simulation. Further justification on the choice of the ensemble and other calculation details can be found elsewhere [10]. The average computation time was about 22 CPU hours for each nanosecond on a high-performance computer cluster of AMD EPYC processors 2300 MHz.

DFT based simulations were also performed to test the impact of OH substitutions on the band gap and band alignment at the interfaces between MAPI and hole and electron transporter materials, respectively. They were carried out using the SIESTA software [17], a code that employs the local density approximation with the inclusion of Hubbard correction (LDA+U) to treat the electron-electron interactions, and numerical atomic orbitals as a basis set to solve the Kohn-Sham equations. Since this ab-initio method operates with atoms, and not with ions like the force based method of LAMMPS, neutral OH groups were used to substitute random iodine atoms in the MAPI layer.

In the case of the hole transporter, the simulation cell consisted of 218 atoms, grouped in 2x2x6 unit cells of Cu_2O, and 1x1x3 tetragonal MAPI. The Brillouin zone was sampled using a Monkhorst-Pack k-point mesh of $7 \times 7 \times 1$. The system was then allowed to relax until the forces on each atom were less than 0.04 eV/Å. The resulting optimized structures were further utilized to determine the electronic states. The partial densities of states (PDOS) were analyzed to determine the band gap and band alignment, using the same Monkhorst-Pack k-point mesh. The energy cutoff for the basis set was 100 Ry.

A similar computational setup was used to check the influence of OH substitutions of iodine atoms at the interface between the MAPI and a TiO_2 layer which has the role of electron transporter in the solar cell device. This time the interface contained 198 atoms, and it was composed from a rutile TiO_2 layer, obtained by multiplying the unit cell with 2x2x5, and a MAPI 1x1x3 tetragonal layer.

III. RESULTS

We computed with LAMMPS the mean square displacement (MSD) of all iodide ions included in the simulation cell, as a function of the time t,

$$\mathrm{MSD}(t) = \frac{1}{N} \sum_{i=1}^{N} |\mathbf{r}_i(t) - \mathbf{r}_i(0)|^2 \ , \tag{1}$$

with N being the total number of iodides and $\mathbf{r}_i$ the position of the particular ion i. The diffusion coefficient associated with the mobile ions can be obtained as

$$D = \frac{1}{6} \lim_{t \to \infty} \frac{\mathrm{MSD}(t)}{t} \ , \tag{2}$$

which in practice is calculated using the slope of the MSD vs. time, divided by the double of the spatial dimension [18].

The numerical results of the MSD are shown in Figure 1. We first consider a simulation cell that in the initial state includes the reference case of an iodide vacancy (IVAC) and no hydroxyl, at room temperature and normal pressure. The corresponding MSD is shown in blue, and the slope is as expected from previous studies [9], [10]. Then, in Test 1 we repeat the simulation by adding an OH^- group in the same unit cell as the IVAC. Further, in Tests 2, 3, and 4, we increase the initial distance between the IVAC and the OH^- group to one, two, and three unit cells, respectively. It can be seen that when the OH^- group is within three unit cells from the vacancy, there is a significant drop in the MSD compared to the IVAC only simulation. To make sure that we observe a real trend of the MSD slope, and not simply random effects, we repeated several simulations by using different seeds of the random number generator, which correspond to different initial positions and velocities of the iodide ions, and indeed, the trend was confirmed. This is because the vacancy migration tends to go toward the OH^- group and once it is within one unit cell distance, the migration of the IVAC is blocked.

As we have shown in a previous study [10], when a vacancy defect is placed in the material, another iodide atoms

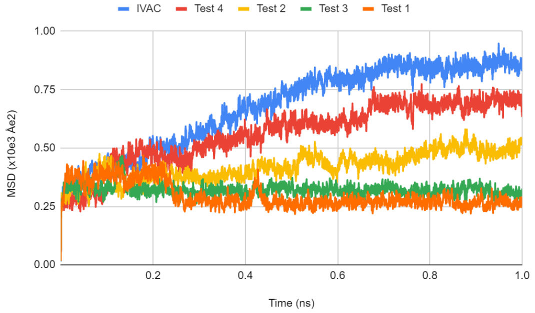

Fig. 1. MSD of all atoms at 300K for 1 ns. From ascending order, each test represents the vacancy and OH^- group are initially placed further apart. In Test 1 they are placed within the same unit cell, in Test 2 they placed one unit cell apart, and so on. The IVAC case corresponds to the MSD of all atoms without the addition of the OH^- group.

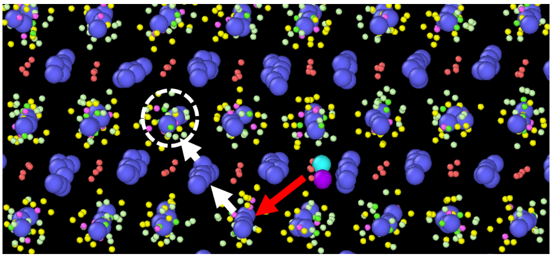

Fig. 2. An example of migration path of both the iodides (white arrows) and hydroxyl group (red arrow) in the presence of a vacancy. The initial position of the iodide vacancy is indicated by the dashed circle. The iodides are shown as dark blue spheres, and the OH^- as a light blue-violet group.

will migrate to fill the vacancy, consequently creating a new vacancy in its place. This process will continue throughout the simulation domain until the vacancy reaches the boundary lines. However, in the presence of the hydroxyl group, the initial migration of iodide atoms will still occur, but, once the newly created vacancy is within roughly one unit cell from the hydroxyl group, this group will migrate toward the vacancy and will remain very close to it, or possibly fill it itself. Thus, the hydroxyl is capable of stopping the migration of the iodide and allowing the system to return to stability. Specifically, in Figure 2, the white dashed circle indicates the initial placement of the IVAC, and the white arrows show the path of the iodides that have migrated and created new vacancies behind them. The red arrow indicates the migration of the hydroxyl group that has joined with the final vacancy, stopping the migration.

A natural question is whether the presence of hydroxyl ions in the MAPI does not harm other properties of the solar cell. While only an experimental study can have a definite answer to this question, here we check if the band alignments of MAPI with the electron and hole transporter layers are affected.

The band alignment at the interface between MAPI and Cu_2O, seen as a hole transporter material, was determined using ab initio DFT calculations with SIESTA software. Initially, the band alignment of the ideal interface was computed, and the PDOS for each material was determined for the bulk-like regions, i.e. excluding the layers in the immediate vicinity of the interface and of vacuum, which introduce additional states. Next, a random iodine atom was replaced with OH, and this procedure was repeated 10 times, each time substituting a different iodine. The results for the ideal interface and three cases with OH are presented in the upper part of Figure 3. The calculations showed a slight shift in energy, but the band alignment appeared to be mostly unaffected, and the placement of OH did not have a significant impact on the band alignment.

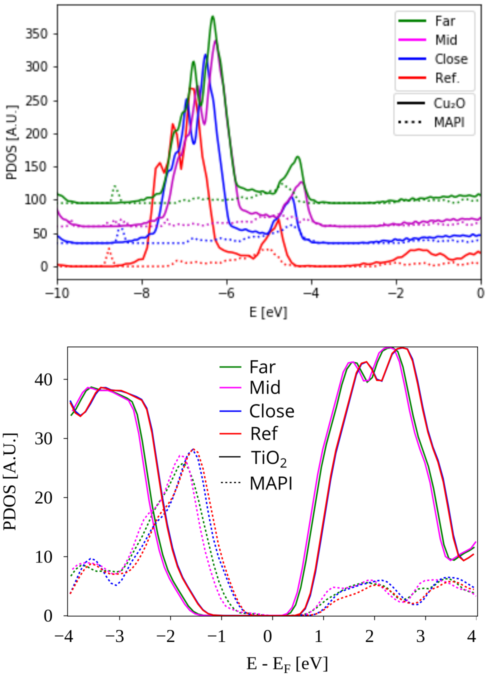

Fig. 3. **Top:** PDOS of MAPI/Cu_2O interface: Solid lines represent Cu_2O, while dotted lines represent MAPI. The red lines show the ideal MAPI/Cu_2O interface, and the blue/green lines have one iodine atom replaced with OH^-. The blue line represents the interface-close substitution, the green line represents the interface-far substitution, and the magenta line a substitution in the middle. The substitution lines have been shifted upwards for clarity.
Bottom: Analog results of the PDOS for MAPI/TiO_2 interface.

We performed similar tests on the MAPI/TiO_2, TiO_2 being a known electron transporter material for MAPI. Four situations were simulated, with the OH group replacing the iodine atoms, to be compared with the case without iodide vacancies. A picture qualitatively similar to the case of the hole transporter emerges, as shown in the lower part of Figure 3, again indicating that the band alignment in the presence of (few) OH^- ions remain practically unchanged. Notably, we also found that an uncompensated iodine vacancy shifts the MAPI bands downwards in energy (not shown), meaning that the OH^- can efficiently compensate for this effect.

IV. Discussion and conclusion

The binding of OH^- to positively charged iodine vacancy is in principle possible in the context of humid environments. Previously, it was shown that, under ambient conditions, superoxide (O_2^-) can be generated at the position of iodine vacancies, which triggers perovskite degradation, leading to the formation of lead iodide, molecular iodine, gaseous methylammonium and water [19]. On the other hand, the formation of OH^- ions can also trigger the deprotonation of the methylammonium, resulting in neutral water and CH_3NH_2 molecules [20]. Therefore, negative ions containing oxygen can passivate iodine vacancies, and likely inhibit iodine migration, but may also prompt the perovskite degradation. However, recent studies have shown that small amounts of coordinating water can have a beneficial effect against degradation, acting as a barrier and preventing the formation of additional hydrates [21]. In a similar way, a stability improvement of formamidinium based solar cells was achieved using ambient air additive during fabrication [22]. Therefore, the potential benefits of the small water amounts should be further investigated experimentally.

The proton H^+ resulting from the dissociation of water, being very light, should be harmless to MAPI. Still, it might bind strongly to iodide, neutralizing and blocking the migration of the slow iodide interstitial ions, or eventually can create iodide vacancies which can be immobilized by the OH^-.

In conclusion, we have shown that a negatively charged hydroxyl ion present in MAPI can form a neutral complex with a positively charged iodide vacancy, thereby reducing the migration of the iodide ions via their vacancies.

Acknowledgment

The research leading to these results has received funding from the EEA Grants 2014–2021, under Project contract no. 36/2021 (project code: EEA-RO-NO-2018-0106). The computational resource was sponsored by EGI and the EGI-ACE H2020 project (GA no. 101017567) with the dedicated support of CLOUDIFIN.

References

[1] N.-G. Park, M. Grätzel, and T. Miyasaka, eds., *Organic-Inorganic Halide Perovskite Photovoltaics. From Fundamentals to Device Architectures*. Springer Cham, 2016.

[2] Y. Zhan, M. Khalid, P. Vivo, and N. Arshid, eds., *Low-Dimensional Halide Perovskites; Structure, Synthesis, and Applications*. Elsevier, 2023.

[3] C. Eames, J. M. Frost, P. R. Barnes, B. C. O'regan, A. Walsh, and M. S. Islam, "Ionic transport in hybrid lead iodide perovskite solar cells," *Nature communications*, vol. 6, no. 1, p. 7497, 2015.

[4] C. Besleaga, L. E. Abramiuc, V. Stancu, A. G. Tomulescu, M. Sima, L. Trinca, N. Plugaru, L. Pintilie, G. A. Nemnes, M. Iliescu, H. G. Svavarsson, A. Manolescu, and I. Pintilie, "Iodine migration and degradation of perovskite solar cells enhanced by metallic electrodes," *J. Phys. Chem. Lett.*, vol. 7, no. 24, pp. 5168–5175, 2016.

[5] R. S. Sanchez, V. Gonzalez-Pedro, J.-W. Lee, N.-G. Park, Y. S. Kang, I. Mora-Sero, and J. Bisquert, "Slow dynamic processes in lead halide perovskite solar cells. Characteristic times and hysteresis," *J. Phys. Chem. Lett.*, vol. 5, no. 13, pp. 2357–2363, 2014.

[6] W. Tress, N. Marinova, T. Moehl, S. M. Zakeeruddin, M. K. Nazeeruddin, and M. Grätzel, "Understanding the rate-dependent J–V hysteresis, slow time component, and aging in $CH_3NH_3PbI_3$ perovskite solar cells: the role of a compensated electric field," *Energy Environ. Sci.*, vol. 8, p. 995, 2015.

[7] G. A. Nemnes, C. Besleaga, A. G. Tomulescu, I. Pintilie, L. Pintilie, K. Torfason, and A. Manolescu, "Dynamic electrical behavior of halide perovskite based solar cells," *Sol. Energy Mater. Sol. Cells*, vol. 159, pp. 197 – 203, 2017.

[8] N. Filipoiu, A. T. Preda, D.-V. Anghel, R. Patru, R. E. Brophy, M. Kateb, C. Besleaga, A. G. Tomulescu, I. Pintilie, A. Manolescu, *et al.*, "Capacitive and inductive effects in perovskite solar cells: the different roles of ionic current and ionic charge accumulation," *Physical Review Applied*, vol. 18, no. 6, p. 064087, 2022.

[9] P. Delugas, C. Caddeo, A. Filippetti, and A. Mattoni, "Thermally activated point defect diffusion in methylammonium lead trihalide: Anisotropic and ultrahigh mobility of iodine," *The Journal of Physical Chemistry Letters*, vol. 7, no. 13, pp. 2356–2361, 2016.

[10] R. E. Brophy, M. Kateb, K. Torfason, G. A. Nemnes, H. G. Svavarsson, I. Pintilie, and A. Manolescu, "Effect of pressure on the dynamics of iodide defects in methylammonium lead iodide: An atomistic simulation," *The Journal of Physical Chemistry C*, vol. 127, no. 17, pp. 7938–7943, 2023.

[11] D. Wang, M. Wright, N. K. Elumalai, and A. Uddin, "Stability of perovskite solar cells," *Solar Energy Materials and Solar Cells*, vol. 147, pp. 255–275, 2016.

[12] E. Mosconi, J. M. Azpiroz, and F. De Angelis, "Ab initio molecular dynamics simulations of methylammonium lead iodide perovskite degradation by water," *Chemistry of Materials*, vol. 27, no. 13, pp. 4885–4892, 2015.

[13] R. Long, W. Fang, and O. V. Prezhdo, "Moderate humidity delays electron–hole recombination in hybrid organic–inorganic perovskites: Time-domain Ab initio simulations rationalize experiments," *The Journal of Physical Chemistry Letters*, vol. 7, no. 16, pp. 3215–3222, 2016.

[14] C. Peng, J. Chen, H. Wang, and P. Hu, "First-principles insight into the degradation mechanism of $CH_3NH_3PbI_3$ perovskite: Light-induced defect formation and water dissociation," *The Journal of Physical Chemistry C*, vol. 122, no. 48, pp. 27340–27349, 2018.

[15] S. Plimpton, "Fast parallel algorithms for short-range molecular dynamics," *Journal of computational physics*, vol. 117, no. 1, pp. 1–19, 1995.

[16] A. Mattoni, A. Filippetti, M. I. Saba, and P. Delugas, "Methylammonium rotational dynamics in lead halide perovskite by classical molecular dynamics: The role of temperature," *The Journal of Physical Chemistry C*, vol. 119, no. 30, p. 17421–17428, 2015.

[17] J. M. Soler, E. Artacho, J. D. Gale, A. García, J. Junquera, P. Ordejón, and D. Sánchez-Portal, "The siesta method for ab initio order-n materials simulation," *Journal of Physics: Condensed Matter*, vol. 14, p. 2745, mar 2002.

[18] M. P. Allen and D. J. Tildesley, *Computer simulation of liquids*. Oxford: Oxford university press, 1989.

[19] N. Aristidou, C. Eames, I. Sanchez-Molina, X. Bu, J. Kosco, M. S. Islam, and S. A. Haque, "Fast oxygen diffusion and iodide defects mediate oxygen-induced degradation of perovskite solar cells," *Nature Communications*, vol. 8, p. 15218, May 2017.

[20] L. Zhang and P. H.-L. Sit, "Ab initio study of interaction of water, hydroxyl radicals, and hydroxide ions with $CH_3NH_3PbI_3$ and $CH_3NH_3PbBr_3$ surfaces," *The Journal of Physical Chemistry C*, vol. 119, no. 39, pp. 22370–22378, 2015.

[21] L. Contreras-Bernal, C. Aranda, M. Valles-Pelarda, T. T. Ngo, S. Ramos-Terrón, J. J. Gallardo, J. Navas, A. Guerrero, I. Mora-Seró, J. Idígoras, and J. A. Anta, "Homeopathic perovskite solar cells: Effect of humidity during fabrication on the performance and stability of the device," *The Journal of Physical Chemistry C*, vol. 122, no. 10, pp. 5341–5348, 2018.

[22] K. M. M. Salim, S. Masi, A. F. Gualdrón-Reyes, R. S. Sánchez, E. M. Barea, M. Krečmarová, J. F. Sánchez-Royo, and I. Mora-Seró, "Boosting long-term stability of pure formamidinium perovskite solar cells by ambient air additive assisted fabrication," *ACS Energy Letters*, vol. 6, no. 10, pp. 3511–3521, 2021.

A.3 Suppression of ionic migration in MAPI perovskite by OH^- ions in the presence of grain boundaries

Rachel Elizabeth Brophy, Movaffaq Kateb, Kristinn Torfason, Halldor Gudfinnur Svavarsson, George Alexandru Nemnes, Andrei Manolescu, ”Suppression of ionic migration in MAPI perovskite by OH- ions in the presence of grain boundaries.” Manuscript in preparation.

OH^- ions can reduce the iodide migration in MAPI in the presence of a grain boundary

Rachel Elizabeth Brophy,[*,†] Movaffaq Kateb,[‡] Jasmín Lára Jóhannsdóttir,[†] Kristinn Torfason,[†] Halldór Guðfinnur Svavarsson,[†] Ioana Pintilie,[¶] George Alexandru Nemnes,[§,‖,⊥] and Andrei Manolescu[†]

†*Department of Engineering, Reykjavik University, Menntavegur 1, IS-102 Reykjavik, Iceland*

‡*Condensed Matter and Materials Theory Division, Department of Physics, Chalmers University of Technology, SE-412 96 Gothenburg, Sweden*

¶*National Institute of Materials Physics, 077125 Magurele-Ilfov, Romania*

§*University of Bucharest, Faculty of Physics, 077125 Magurele-Ilfov, Romania*

‖*Research Institute of the University of Bucharest (ICUB), Mihail Kogalniceanu Blvd 36-46, 050107 Bucharest, Romania*

⊥*Horia Hulubei National Institute for Physics & Engineering, 077126 Magurele-Ilfov, Romania*

E-mail: rachel18@ru.is

Abstract

Due to its unique properties and high efficiency, the perovskite material methylammonium lead iodine (MAPI) has become a primary research topic in photovoltaic technology. However, the MAPI material suffers from low stability and a high degradation rate. One primary reason for the degradation is the ionic migration caused by the diffusion of iodide vacancies. This paper's focus demonstrates the possibility of suppressing ionic diffusion using OH^- ions. We use molecular dynamic simulations to show that OH^- ions show an attractive force to the positively charged iodide vacancies, blocking the migration to the negative iodide ions and ultimately halting the migration. We perform numerical simulations both in the perfect crystal and in the presence of a grain boundary.

Keywords: MAPI material, iodide migration, grain boundary, molecular dynamics simulations.

Introduction

Due to its unique photovoltaic properties, the perovskite material has become a prominent research topic in recent years. Compared to conventional solar cells, the perovskite material can operate within its natural structure to convert light into electricity without doping mechanisms or additional junctions. Not only does this significantly reduce manufacturing costs, but the overall fabrication of the perovskite-based solar cell is simple and only requires basic equipment.[1] The overall efficiency of the perovskite solar cell has increased from 13% to roughly 25% within 13 years, making it one of the fastest-growing efficiency rates of all types of solar cells. However, perovskite solar cell commercialization has become impossible due to the material's high degradation rate and short shelf-life.

There are several reasons for the high degradation rate of the perovskite solar cells. Some examples are temperature variations, moisture and humidity, and ionic migration.[2] Through the use of molecular dynamic (MD) simulations, it is possible to understand the details of the degradation mechanisms. Specifically, recent MD simulations have shown that the ionic migration of iodide atoms has the most significant role in the degradation of the perovskite material.[3] A positively charged vacancy is left behind when the negative iodide is missing from the system. This causes the other iodides in the system to migrate toward the vacancy and ultimately fill it, simultaneously creating a new vacancy. Given the domino effect of a new vacancy being created each time another is filled, the diffusion coefficient of an iodide vacancy has been calculated to be between $2.5 - 4.3 \times 10^{-6}$ cm^2/s.[4,5]

Due to the large impact of the iodide migrations, several MD simulations were completed to determine if external factors, such as pressure or temperature alterations, can suppress the migrations. For example, in our previously published work, we suggest that highly compressive pressure can reduce to ionic migration and enable the material to remain stable.[5] However, applying a high compressive pressure to the perovskite material under its working conditions is not an ideal solution. Therefore, instead of using external factors to suppress the migrations, filling the vacancy may be more beneficial before the migration even occurs.

Although humidity can lead to the degradation of the perovskite material through iodide dislocation and a decrease in the absorption factor,[6] we suggest that small amounts of water may be beneficial to the material by delaying the electron-hole recombination without causing changes to the band gap.[3] Density functional theory (DFT) calculations show that water dissociates into H^+ and OH^- (hydroxyl) at 0.75 eV in the dark and 0.57 eV in the presence of photo-generated electrons.[7] Through DFT calculations, previous research has shown that the addition of OH^- does not cause adverse effects on the band alignment between the MAPI and electron transport layer material.[8] Small amounts of water may be introduced into the perovskite material through fabrication or generated at the surface and enter through grain boundaries. We can assume that if water enters the system, there are also accumulations of hydroxy ions.

Simultaneous to the addition of the hydroxyl group into the perovskite material, we included a grain boundary defect as well. A grain boundary, commonly seen in polycrystalline solar cells, occurs when two separate crystal lattices are placed together. In the case of the perovskite solar cells, a grain boundary is common in the two-step spin coating fabrication process.[9] Therefore, the presence of a grain boundary makes our model more realistic. The addition of a grain boundary also creates a slight potential difference in the material, depending on whether the grain boundary has dangling iodide atoms, or lead atoms.[9] We suggest that the grain boundary may also help suppress the migration of the iodide vacancy, an effect that may be enhanced in the presence of the hydroxyl. Our present work is based on MD simulations.

Methods

Through the use of MD simulations, we were able to analyze the movement of all atoms within the MAPI system. All simulations were done using the LAMMPS software,[10] by solving for Newton's equations of motion for all atoms. Our simulations utilized the $CH_3NH_3PbI_3$ stoichiometry with the MA (methylammonium) molecules having a 1:1 ratio with the Pb atoms, placed in the middle of each cubic cell made of PbI_3. We introduced grain boundaries into the system, an example of which can be seen in 1. This was done by rotating the crystal $+/-18.5°$ in two grains, giving twin boundaries of $\sum 5/(120)[001]$. The grain boundaries were then shifted to give a uniform distance between them. The final product of the system is pictured in 2, which was created using the OVITO program.

We utilized the MYP potentials derived by Mattoni, et al.[11] to account for all interatomic forces. This potential considered bonded interactions in the MA molecule and non-bonded PbI cage and Pb-MA. This will produce a stable cubic phase at 300 K. The intra-MA interactions were modeled using a bounded generalized AMBER force field (GAFF), and the Buckingham force field was used for Pb-Pb, I-I, Pb-I, and Pb/I-C/N interactions. Pb/I-H interactions were modeled with Lennard-Jones potential. For the hydroxyl, we used TIP3P parameters with charges -0.8476 e for O and 0.4238 e for H ions. This gives the hydroxyl

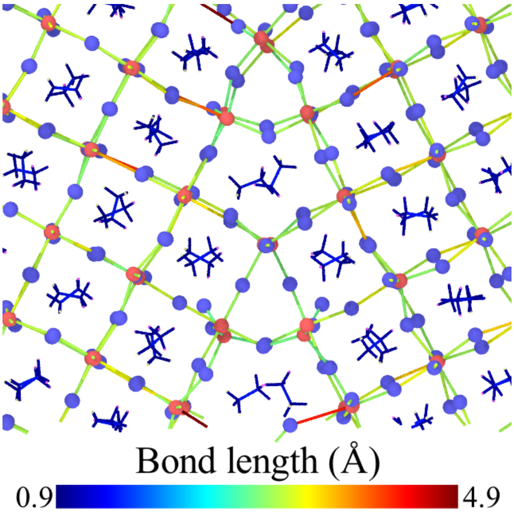

Figure 1: Visualization of a dangling iodide in the so-called MAI grain boundary. Red and blue atoms denote Pb and I. MA, illustrated by their bonds.

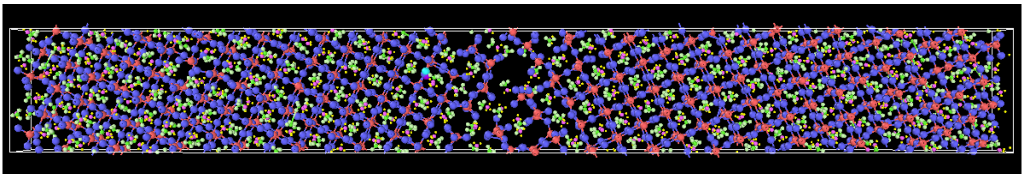

Figure 2: Super cell composed of two grains and MAI grain boundary in the middle and PbI_2 grain boundary at the ends

group a total of -0.4238 e compared to $+1.13$ e for iodide vacancy.

The simulated system comprises 3471 atoms, corresponding to $8 \times 8 \times 4 = 256$ cubic units, first relaxed through energy minimization and maintained at a temperature of 300 K and a pressure of 1 bar for 1 ns, producing samples from isothermal-isobaric (NPT) ensemble. Once the relaxation is complete, a single iodide atom is removed, and a hydroxyl group is placed into the system. To see if adding the hydroxyl group mediated the vacancy migration, we considered iodide vacancy and hydroxyl group at different distances with respect to grain boundaries.

All results were computed with LAMMPS using the mean squared displacement (MSD) of all iodide atoms within the simulation cell as a function of time t.

$$\mathrm{M}SD(t) = \frac{1}{N}\sum_{i=1}^{N} |\mathbf{r}_i(t) - \mathbf{r}_i(0)|^2 \ , \tag{1}$$

with N being the total number of iodides and $\mathbf{r}_i$ the position of the particular ion i. The diffusion coefficient associated with the mobile ions can be obtained as

$$D = \frac{1}{6}\lim_{t\to\infty}\frac{\mathrm{M}SD(t)}{t} \ , \tag{2}$$

Each simulation was completed six times with different seeds, a pseudonym number to initialize the simulations. This process allows us to ensure our results are reliable and repeatable. The pressure and temperature were set to room temperature (300 K) and standard pressure (1 atm) to ensure no external factors affected the migrational patterns.

The computation time averaged 22 CPU hours per nanosecond on a computer cluster of AMD EPYC processors 2300 MHz.

Results

The effect of OH^-

Using a simulation cell of a perfect crystal structure, where the initial states include only an iodide vacancy (IVAC), the diffusion coefficient that we previously obtained from the slope of the MSD, at room temperature and atmospheric pressure, was 2.4×10^{-6} cm^2/s, with a 9% uncertainty,[5] comparable that reported by another study, which was $4.3{\times}10^{-6}$ cm^2/s.[4]

To try to mediate the iodide diffusion, we now systematically included a hydroxyl group in the perfect crystal structure containing a vacancy defect at varying distances. Each trial was completed ten times, changing the seed, allowing for slight alterations of the initial conditions. Figure:3 shows the MSD obtained with an OH^- group and the iodide initially placed at the same vacancy location. The graph clearly shows a stable MSD for each seed trial throughout the simulation of 1 ns. The average diffusion coefficient of all seeds was calculated to be 7.9 cm$^2/s$, with a statistical standard error (i.e. the standard deviation divided by the square root of the sample size) or 32%. This relatively large uncertainty is consistent with the very low diffusion coefficient.

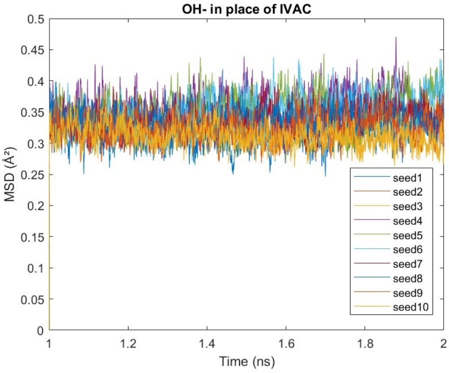

Figure 3: Perfect crystal structure containing a vacancy defect, and a hydroxy group placed in the same location. Each line on the graph represents a different seed, with a total of 10 seed trials.

After this group of simulations, we increased the distance between the initial placement of the vacancy and the hydroxyl group to 1 unit cell. Figure:4, shows the MSD of all ten seed trials at this distance. The average MSD for this simulation set was calculated to be 1.1×10^{-6} with a standard error of 25%. In this case, there is an initial increase in the MSD, as the iodide vacancy travels toward the vacancy, then once close enough, returns to stability.

Next, we increased the distance between the initial vacancy and the hydroxyl group to four unit cells away. Figure:5 shows the results from this trial. In this case, the iodide migration does not seem to be suppressed, and there is a significant increase in the MSD throughout the simulation. The average diffusion coefficient of the 10 seed trials was calculated to be 1.7×10^{-7} with a standard error of 16%.

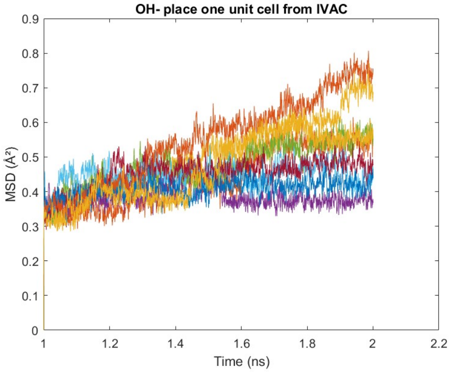

Figure 4: Perfect crystal structure containing a vacancy defect, and a hydroxy group placed at a distance of 1 unit cells. Each line on the graph represents a different seed, with a total of 10 seed trials.

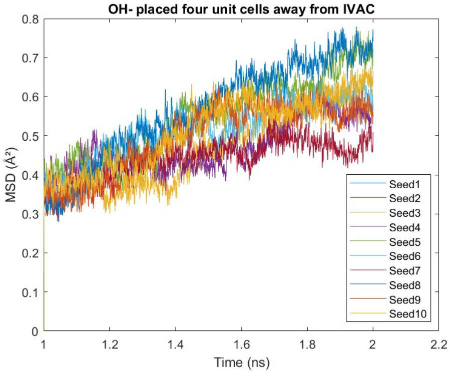

Figure 5: Perfect crystal structure containing a vacancy defect, and a hydroxy group placed at a distance of 4 unit cells. Each line on the graph represents a different seed, with 10 seed trials.

Table 1: Average diffusion coefficient and standard error for each trial.

Trials	Diffusion Coefficient (cm^2/s)	Standard Error (%)
OH^- in place of vacancy	7.9×10^{-8}	32
OH^- at one unit cell distance	1.1×10^{-6}	25
OH^- at two unit cells distance	1.7×10^{-6}	16
OH^- at four unit cells distance	1.7×10^{-6}	9

The effect of grain boundary

Simulations were then done in the presence of a dangling iodine grain boundary. This allows for a net negative grain boundary. By doing this, we can determine whether the positive vacancy would rather travel toward the grain boundary, or be suppressed by the hydroxyl group.

Figure 6 shows the MSD of all iodide atoms in our grain boundary system with an IVAC between the grain boundary and the periodic boundary. The IVAC was initially located three unit cells from the grain boundary, on the left side in Figure 2. The estimated average diffusion coefficient is 2.8 cm^2/s, which is comparable to the value in the perfect crystal. Which means that with the present initial conditions the grain boundary does not block the migration of the IVAC.

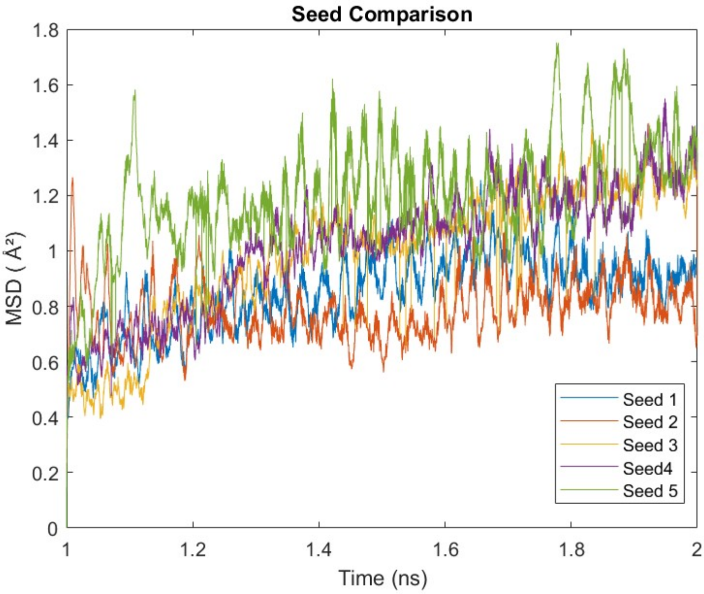

Figure 6: Graphical analysis of the MSD of all iodide atoms in the MAPI system, in the presence of a dangling iodide grain boundary.

The effect of OH^- in the presence of the grain boundary

We added defects once we completed the baseline for your system in the presence of a grain boundary. Like the perfect crystal structure simulations, we created a vacancy defect and added a single hydroxyl group either next to or three unit cells away from the vacancy. Starting from the initial conditions when the OH^- and the IVAC have the same location, we obtained a similar diffusion constant as in the absence of the grain boundary, 7.81 $\times 10^{-8}$ cm^2/s, with a standard error of 26%. Which means the diffusion of the IVAC is still blocked (or reduced) by the hydroxyl group in the presence of the grain boundary.

When placing the hydroxyl group three unit cells away from the vacancy defect, we see an increase in the overall MSD, shown in Figure 7. The average diffusion coefficient over the six trials is 1.6×10^{-6} cm^2/s, with a standard error of 24%, again comparable to the value obtained in the absence of the grain boundary and shown in Table 1.

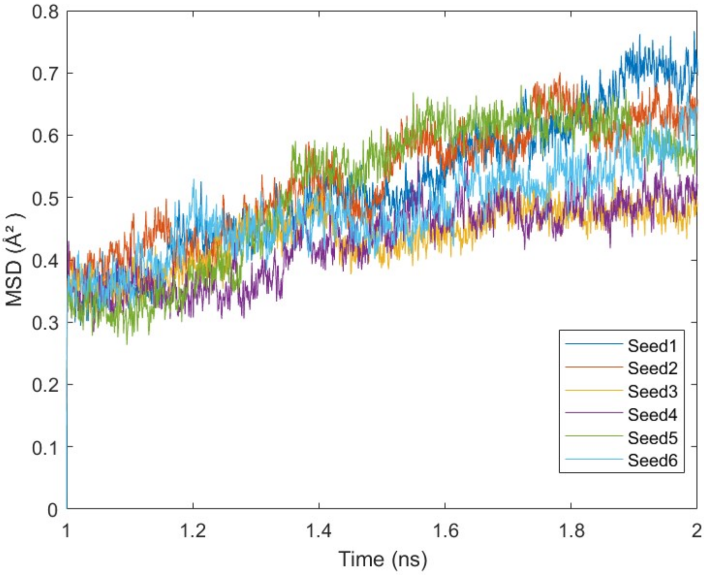

Figure 7: Crystal structure with a grain boundary and vacancy defect. An OH- molecule was placed three unit cells away from vacancy.

Conclusion

In the perfect crystal structure, when the hydroxyl group and the initially placed vacancy are in close proximity, within a few unit cells, the hydroxyl group will work to fill the vacancy. While using the OVITO visualization software, it was noted that the vacancy is more likely to migrate toward the hydroxyl group. In contrast, the hydroxyl group remains around its initial placement, with only slight migration. In these cases, the MSD increases slightly at the beginning of the simulations, but once the vacancy meets the hydroxyl group the MSD indicates stability and remains so for the duration of the simulation. However, in cases where the vacancy and hydroxyl groups are initially at a distance of two to four unit cells, the vacancy is more likely to migrate away, but still slower than in the absence of the hydroxyl.

We showed that a grain boundary alone has a negligible effect on the IVAC migration if the IVAC is initially three unit cells from it. However, despite the highly negative charge of the grain boundary, the presence of the hydroxyl group close to the boundary is still able to suppress the IVAC migration. Therefore it appears that the grain boundary does not suppress attraction between the IVAC and the hydroxyl.

The addition of water molecules is typically considered a significant defect in the perovskite material, decreasing both the stability and lifetime of the material. However, the results of this paper can conclude that small amounts of water added to the system may increase the stability, due to suppressing a more detrimental defect, i.e. ionic migration.

Acknowledgment

The research leading to these results has received funding from the EEA Grants 2014–2021, under Project contract no. 36/2021 (project code: EEA-RO-NO-2018-0106), and from the Reykjavik University doctoral fund. The computational resource was sponsored by EGI and the EGI-ACE H2020 project (GA no. 101017567) with the dedicated support of CLOUD-

IFIN.

References

(1) Park, N.-G., Grätzel, M., Miyasaka, T., Eds. *Organic-Inorganic Halide Perovskite Photovoltaics. From Fundamentals to Device Architectures*; Springer Cham, 2016.

(2) Wang, D.; Wright, M.; Elumalai, N. K.; Uddin, A. Stability of perovskite solar cells. *Solar Energy Materials and Solar Cells* **2016**, *147*, 255–275.

(3) Mosconi, E.; Azpiroz, J. M.; De Angelis, F. Ab Initio Molecular Dynamics Simulations of Methylammonium Lead Iodide Perovskite Degradation by Water. *Chemistry of Materials* **2015**, *27*, 4885–4892.

(4) Delugas, P.; Caddeo, C.; Filippetti, A.; Mattoni, A. Thermally Activated Point Defect Diffusion in Methylammonium Lead Trihalide: Anisotropic and Ultrahigh Mobility of Iodine. *The Journal of Physical Chemistry Letters* **2016**, *7*, 2356–2361.

(5) Brophy, R. E.; Kateb, M.; Torfason, K.; Nemnes, G. A.; Svavarsson, H. G.; Pintilie, I.; Manolescu, A. Effect of Pressure on the Dynamics of Iodide Defects in Methylammonium Lead Iodide: An Atomistic Simulation. *The Journal of Physical Chemistry C* **2023**, *127*, 7938–7943.

(6) Wang, D.; Wright, M.; Elumalai, N. K.; Uddin, A. Stability of perovskite solar cells. *Solar Energy Materials and Solar Cells* **2016**, *147*, 255–275.

(7) Long, R.; Fang, W.; Prezhdo, O. V. Moderate Humidity Delays Electron–Hole Recombination in Hybrid Organic–Inorganic Perovskites: Time-Domain Ab Initio Simulations Rationalize Experiments. *The Journal of Physical Chemistry Letters* **2016**, *7*, 3215–3222.

(8) Brophy, R. E.; Kateb, M.; Ghitiu, I.; Filipoiu, N.; Torfason, K.; Svavarsson, H. G.; Nemnes, G. A.; Pintilie, I.; Manolescu, A. OH^- ions can reduce the iodide migration in MAPI. 2023 International Semiconductor Conference (CAS). 2023; pp 139–142.

(9) Lee, J.-W.; Bae, S.-H.; Marco, N. D.; Hseih, Y.-T.; Dai, Z.; Yang, Y. The role of grain boundaries in perovskite solar cells. *Materials Today Energy* **2018**,

(10) Plimpton, S. Fast parallel algorithms for short-range molecular dynamics. *Journal of computational physics* **1995**, *117*, 1–19.

(11) Mattoni, A.; Filippetti, A.; Saba, M. I.; Delugas, P. Methylammonium Rotational Dynamics in Lead Halide Perovskite by Classical Molecular Dynamics: The Role of Temperature. *The Journal of Physical Chemistry C* **2015**, *119*, 17421–17428.

Appendix B

Experimental

B.1 Ultra responsive silicon nanowires NO2 gas sensor

Rachel Elizabeth Brophy, Benjamin Junker, Elham Aghabalei Fakhri, Hákon Örn Árnason, Halldór Guðfinnur Svavarsson, Udo Weimar, Nicolae Bârsan, Andrei Manolescu, Ultra Responsive NO_2 silicon nanowires gas sensor, Sensors and Actuators B: Chemical **410**, 135648 (2024).

Ultra responsive silicon nanowires NO_2 gas sensor

Rachel Elizabeth Brophy,[*,†] Benjamin Junker,[‡,¶] Elham Aghabalei Fakhri,[†] Hákon Örn Árnason,[†] Halldór Guðfinnur Svavarsson,[†] Udo Weimar,[‡,¶] Nicolae Bârsan,[‡,¶] and Andrei Manolescu[†]

[†]*Department of Engineering, Reykjavik University, Menntavegur 1, IS-102 Reykjavik, Iceland*

[‡]*Institute of Physical and Theoretical Chemistry, University of Tübingen, Auf der Morgenstelle 15, 72076 Tübingen, Germany*

[¶]*Center for Light-Matter Interaction, Sensors & Analytics (LISA+), University of Tübingen, Auf der Morgenstelle 15, 72076 Tuebingen, Germany*

E-mail: rachel18@ru.is

Abstract

Nitrogen dioxide (NO_2) is a hazardous gas emitted primarily from burning fossil fuels. When inhaled, it can have severe health implications, particularly for individuals with respiratory conditions such as asthma. It contributes to ground-level ozone formation, which can cause reduced lung function and increased susceptibility to respiratory infections. When in contact with water moisture in the air, NO_2 is easily oxidized into nitric acid (HNO_3), causing acid rain. Detection of NO_2 levels is therefore important for monitoring air quality and protecting public health. Among the possible technical solutions for gas sensing, silicon nanowires (SiNWs) have proven to be a promising candidate, partly due to their high sensitivity, low manufacturing cost, and ability to perform in various air qualities. This paper presents using SiNWs, fabricated by metal-assisted chemical etching, as a fast, accurate, sensitive, robust, and cost-effective

NO_2 gas sensor. Our SiNWs gas sensor can experimentally detect 20 parts per billion (ppb) of NO_2 under a wide range of relative humidity. Our sensor shows ultra-high sensitivity with fast response and recovery time.

Introduction

Air pollutants can have detrimental effects on the environment as well as human health. One of the gases that have been of great concern is nitrogen dioxide (NO_2). It is released primarily from burning fossil fuels through power plants and automobiles and is considered one of the major pollutants in today's atmosphere. Exposure to it can cause respiratory infections, even at very low concentrations. Present healthy standards correspond to 53 ppb annual average, with an one-hour daily maximum concentration of 100 ppb.[1] Additionally, NO_2 contributes to the formation of acid rain when it reacts with water molecules to form HNO_3. It is, therefore, vitally important to monitor and measure the NO_2 concentration in a fast and accurate way.

Silicon nanowires (SiNWs), with their unique properties and versatile nature, have emerged as promising building blocks for various applications across different fields, ranging from solar cells and biosensors to thermoelectrics, as discussed in a very recent review article.[2] These nanoscale structures, typically ranging from a few to a few hundred nanometers in dimensions, can be integrated into transistors, memory devices, and sensors, enabling advancements in miniaturization and performance. This is mainly due to their large surface-to-volume ratio and high sensitivity of current-voltage (I-V) characteristics to the presence of surface states.[3]

Among the various existing methods to synthesize the SiNWs, metal-assisted chemical etching (MACE) is one of the simplest, and it offers the perspective of integration with microelectronics technologies at a lower cost with larger processable areas[4] and easy tuning of geometrical parameters.[5] Both disordered (random)[6] and ordered (periodic)[7] arrays of SiNWs can be obtained by MACE, and they can be fabricated in just two very simple wet-chemical steps. In particular, a recent study reported a sensor based on SiNWs that exhibited a change of electrical resistance of several percent upon exposure to human breath.[8] The presence of germanium (Ge) nanoparticles on the surface of the SiNWs (Ge:SiNWs) could further improve the sensitivity of such a sensor to humidity, and stabilize the baseline.[9]

SiNWs used as an NO_2 gas sensor have been a topic of research in recent years. In et al.[10] used periodic arrays of SiNWs covered with a periodic porous top electrode, and could detect down to 10 ppb NO_2 for relative humidity (r.h.) below 10% , whereas the detection level reported at higher humidity, such as 30%, was much higher, i.e. 500 ppb. More recently, Kwon et al.[11] used disordered arrays of SiNWs, and were able to detect 10 parts per million (ppm) of NO_2 at room temperature in dry conditions, but increasing the humidity to 40% - 80% (typical atmospheric conditions) had a detrimental effect on their sensitivity. It was suspected that the humidity blocks the NO_2 from binding with the SiNWs, causing a decrease in the overall response, and in order to lessen this reaction, Qin et al.,[12] placed an octadecyltrichlorosilane (OTS) layer within the sensor to block the access of the water molecules to the surface of the SiNWs. With this device, they could detect 50 ppb of NO_2 in the presence of 70% r.h.

In contrast, our simpler SiNW sensor does detect concentrations of NO_2 at least as low as 20 ppb at room temperature at up to 80% r.h. This allows for a more realistic application of the sensor, using a cheaper and simpler fabrication method than previously reported.

Results and discussion

Our results demonstrate that the sensor based on SiNWs can work successfully as a humidity sensor and a NO_2 gas sensor. The behavior of the SiNW sensor as a humidity sensor was comparable to that of a commercial-grade humidity sensor. Figure 1 shows the increase in resistance due to the rise in the relative humidity in the chamber. The relative humidity was tested by setting a baseline of 0% R.H for the first two hours. The humidity was then raised step-wise every half an hour until it reached 80% and then reduced step-wise back to 0% in the same manner. The resistance increased from 20 Ω at 0% R.H to 30 Ω at 80% R.H To test the baseline steadiness, the next testing set included an increase of the humidity for 0.5 h, and then an immediate decrease back to 0% for the next 0.5 h. This testing was done six times. These results showed that the SiNW sensor has both a steady baseline, as well as a fast response time.

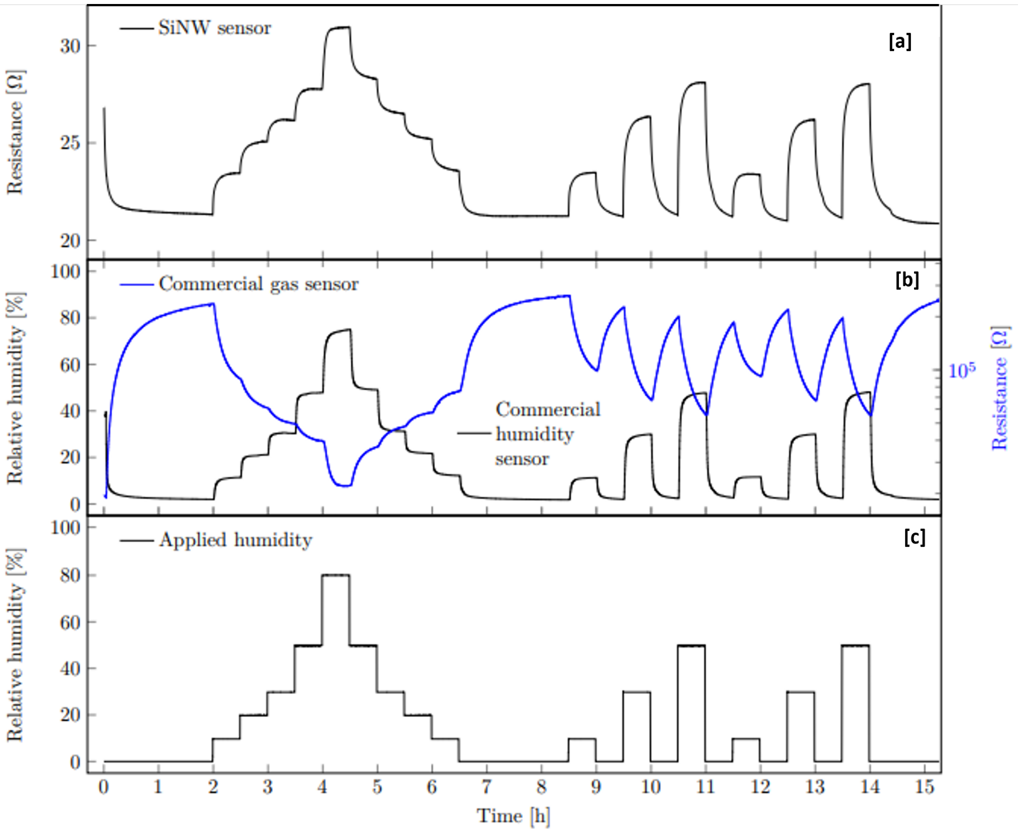

Figure 1: Graph (a) shows the SiNW response to varying relative humidity concentrations. Graph (b) shows the response of the commercial humidity sensor HYT 939 and the commercial gas sensor TGS 2600. Graph (c) shows the actual set of relative humidity concentrations.

In the course of this study, the response of the SiNWs to NO_2 was tested extensively, both in the presence of humidity and without humidity. The sensor responded well to concentrations as low as 20 ppb of NO_2. The response and especially the recovery, however, was limited in dry conditions and became faster with increasing the background humidity, as shown in Fig. 2. The recovery was much faster in the presence of humidity already at 10% R.H, which is important for practical applications.

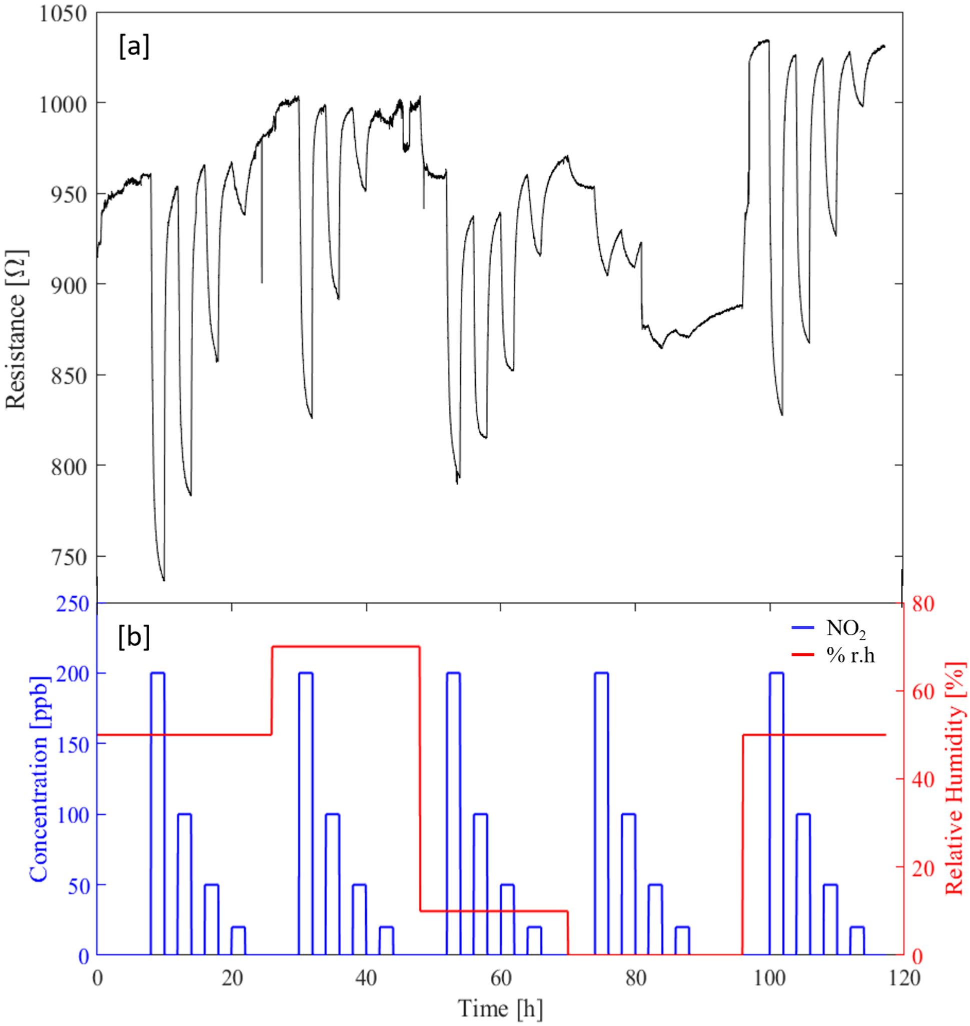

Figure 2: (a): SiNW response to NO_2 in varying relative humidity concentrations. (b): concentration of NO_2 and background humidity, measured at 20 °C. The humidity was modified in several steps for more than 100 hours.

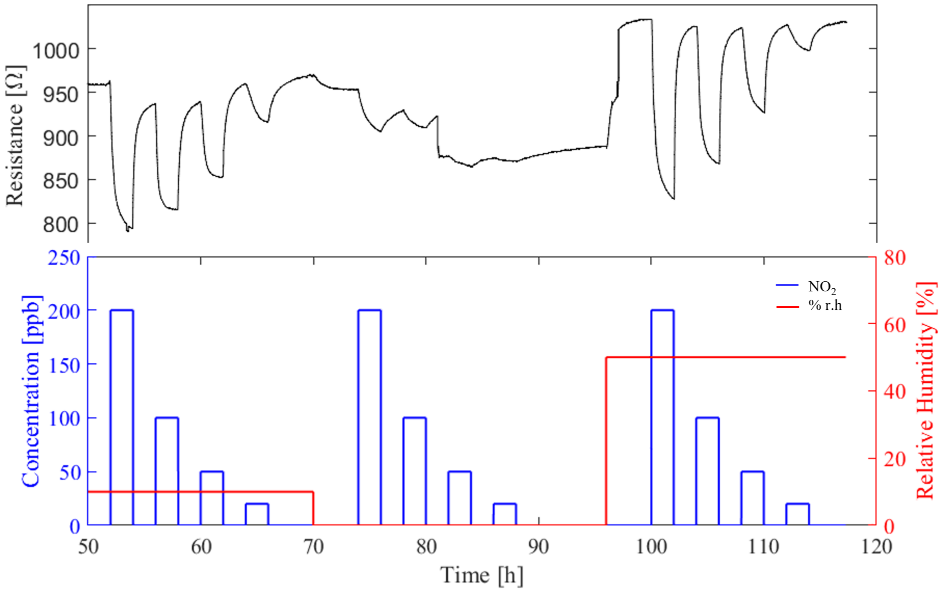

Figure 3: Zoomed-in image of Figure 2, showing the resistance with changing concentration of NO_2 and humidity after 50 hours. During this time, the sensor has established stability.

To determine the sensor's cross-sensitivity, a variety of common reducing gases was also tested on a separate sample. No significant response was observed from any of them except for hydrogen, which produced a minor increase in resistance, as shown in Fig. 4. In the presence of humidity, the resistance baseline was increased from 28 Ω to 30 Ω, without causing any detrimental effects on the sensitivity to NO_2.

Based on the above results, it can be concluded that the SiNWs system can detect both humidity and NO_2 with high sensitivity and high selectivity. We have also been able to prove reproducibility through testing different samples with similar sensitivity responses. While we could detect an experimentally controlled concentration of 20 ppb NO_2, it is obvious from Figure 5 that the gradient of the signal, i.e. the sensitivity, at low concentrations is strong enough to allow the detection of even lower NO_2 concentrations in the presence of humidity.

Previous experimental work reported the detection of humidity with SiNWs using impedance spectroscopy measurements, as capacitance variations due to the presence of water molecules

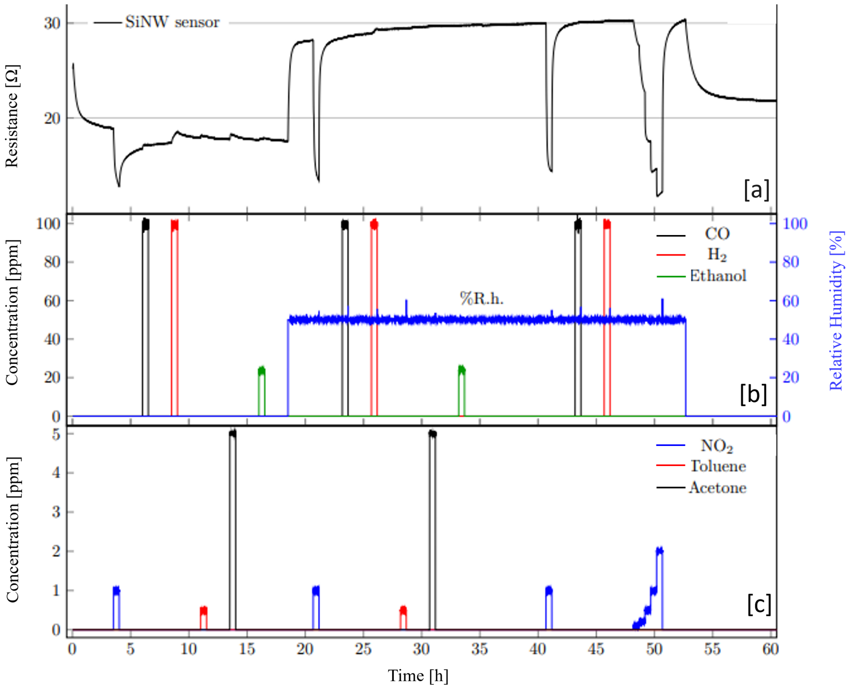

Figure 4: Graph (a) shows the resistance variation in the SiNW sensor with changing the gas concentrations. Graphs (b) and (c) show the input concentrations of varying gases and R.H..

in the proximity of the nanowires[13].[14] Our understanding of the gas sensing mechanism involved in our experiments is based on the interaction of the SiNWs surface with atmospheric oxygen, which can occur at room temperature.[15] The SiNWs were made from a p-type wafer. The chemisorption of oxygen leads to increased hole concentration in the bulk, as electrons are localized at the surface as O_2^- (superoxo) ions in a dynamic equilibrium. Water vapor will disturb this equilibrium by competing with oxygen molecules for suitable adsorption sites at the surface.[16] In contrast to oxygen, water molecules are probably only physisorbed and no charge transfer occurs at room temperature.[17] The observed increase in resistance

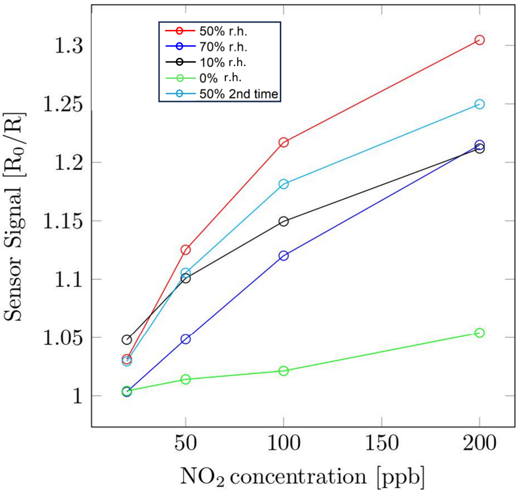

Figure 5: Sensor signals of the SiNWs for different concentrations of NO_2 in different background levels of relative humidity.

due to humidity exposure is thus ascribed to a displacement of oxygen ions.

In contrast to H_2O, NO_2 can be ionosorbed at the surface already at room temperature. The interaction of NO_2 with the silicon surface has been reported as a formation of surface states that enable a charge transfer.[18,19] The result is the creation of additional holes and a decrease in resistance. The surface interacts much stronger with NO_2 than with H_2O or O_2 and will dominate in this competition. This suggested mechanism can also explain the higher sensor response in humidity compared to dry air: The more water is present at the surface before exposure to NO_2, the more can be displaced by NO_2. The other analytes are either not dissociated at room temperature, e.g. H_2, or their interaction is too weak to compete with O_2 for reactive sites.

Experimental

The SiNWs were made from single-side polished, p-type (boron-doped), (100) Si-wafers with a thickness of 525 µm and resistivity ρ of 0.1 Ω cm to 0.5 Ω cm. A two-step MACE fabrication route was used to process the samples. The first steps involved the deposition of silver nanoparticles (Ag-NPs) on top of the Si-wafer in an aqueous solution of 1.5 mM $AgNO_3$ and 3 M hydrofluoric acid (HF) for 1 minute. The second step involved catalytic etching of the wafer in a diluted solution of HF and hydrogen peroxide (H_2O_2) for 20 min. Before the Ag-NPs deposition, the wafers were cleaned in an ultrasonic bath with acetone, methanol, and isopropanol, after which they were dipped in deionized water and dried with nitrogen (N_2) gas. A more detailed description of the fabrication process can be found elsewhere.[6]

The SiNWs surface morphology shown in Figure 6 was characterized by a field-emission scanning electron microscope, FE-SEM (ZEISS SUPRA 35). A top-view and a cross-section image of SiNWs obtained after 20 min etching time is seen. The top-view image reveals that the synthesized SiNWs form an interconnected structure that forms bundles at the tips of wires due to capillary forces being activated when extracting the samples out of the etching solution. Also, a uniform etching depth of 6 µm is evidenced in the cross-sectional image. In order to obtain the diameter of each nanowire, samples were partially cut using a razor blade to separate the wire area from the un-etched part of the Si wafer. The SEM image of the extracted wires revealed the diameter of wires being around 100 nm.

A custom-made gas mixing system with mass-flow controllers (Tylan, Bronkhorst) was used to characterize the SiNWs as a gas sensor. The samples were placed in a measurement chamber made from polytetra fluoro ethylene (PTFE), to limit exposure to outside interactions. The electrical resistance was measured with a Multimeter (Keysight 34972A) in a four-wire configuration. The contact pads on the wafer were connected to copper wires using conductive silver paste (Plano). Humidity was adjusted by sending a ratio of dry air through a vaporizer filled with deionized water, providing 100 % r.h. (measured at 20 °C). To assess the sensor performance, a commercial humidity sensor (HYT939, IST AG) and a

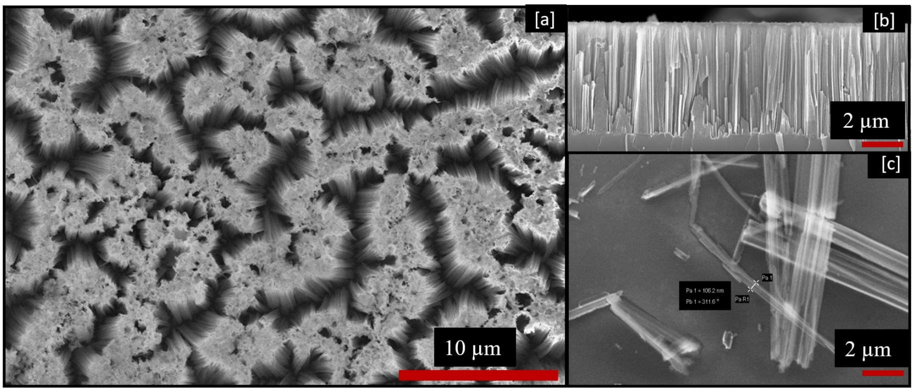

Figure 6: SEM micrographs of SiNWs obtained by MACE after 20 min etching. Image (a) is the top view of the SiNWs. Image (b) is the cross-sectional analysis. Image (c) shows individual wire configuration on a broken surface.

commercial air quality SMOX gas sensor (TGS2600, Figaro) were used.

Conclusions

Our experimental results show that p-doped silicon nanowires fabricated with the MACE method can be used as an inexpensive alternative to commercial humidity and NO_2 sensors. The lowest concentration of NO_2 detected under experimental control was 20 ppb. Unlike common NO_2 gas sensors, our SiNW gas sensors are able to operate at high humidity levels, allowing for more realistic applications. The construction of the sensor device, outlined in the experimental section, is simple and easily reproducible. The experimental results suggest a sensing mechanism that is based on the dynamic equilibrium of the oxygen at the SiNWs surface, in the presence of water molecules, which proves to be very sensitive to the charge transfer from NO_2.

Acknowledgement

This work was supported by the Reykjavik University Research Fund (grant no. 222018), National Power Company of Iceland (Landsvirkjun) via the Sustainability Institute Forum (SIF) of Reykjavik University (grant no. 221051), and the Icelandic Research Fund (grant no. 223033).

References

(1) USEPA, *Integrated Science Assessment for Oxides of Nitrogen – Health Criteria*; 2016.

(2) Raman, S.; Sankar, A. R.; Sindhuja, M. Advances in silicon nanowire applications in energy generation, storage, sensing, and electronics: a review. *Nanotechnology* **2023**, *34*, 182001.

(3) Plugaru, R.; Fakhri, E.; Romanitan, C.; Mihalache, I.; Craciun, G.; Plugaru, N.; Árnason, H.; Sultan, M.; Nemnes, G.; Ingvarsson, S.; Svavarsson, H.; Manolescu, A. Structure and electrical behavior of silicon nanowires prepared by MACE process. *Surfaces and Interfaces* **2022**, *33*, 102167.

(4) Huo, C.; Wang, J.; Fu, H.; Li, X.; Yang, Y.; Wang, H.; Mateen, A.; Farid, G.; Peng, K.-Q. Metal-Assisted Chemical Etching of Silicon in Oxidizing HF Solutions: Origin, Mechanism, Development, and Black Silicon Solar Cell Application. *Advanced Functional Materials* **2020**, *30*, 2005744, _eprint: https://onlinelibrary.wiley.com/doi/pdf/10.1002/adfm.202005744.

(5) Leonardi, A. A.; Faro, M. J. L.; Irrera, A. Silicon Nanowires Synthesis by Metal-Assisted Chemical Etching: A Review. *Nanomaterials* **2021**, *11*, 383.

(6) Fakhri, E.; Plugaru, R.; Sultan, M. T.; Kristinsson, T. H.; Árnason, H. O.; Plugaru, N.;

Manolescu, A.; Ingvarsson, S.; Svavarsson, H. G. Piezoresistance Characterization of Silicon Nanowires in Uniaxial and Isostatic Pressure Variation. *Sensors* **2022**, *22*, 6340.

(7) Svavarsson, H. G.; Hallgrimsson, B. H.; Niraula, M.; Lee, K. J.; Magnusson, R. Large arrays of ultra-high aspect ratio periodic silicon nanowires obtained via top–down route. *Applied Physics A* **2016**, *122*, 52.

(8) Ghosh, R.; Song, M. S.; Park, J. B.; Tchoe, Y.; Guha, P.; Lee, W.; Lim, Y.; Kim, B.; Kim, S. W.; Kim, M.; Yi, G. C. Fabrication of piezoresistive Si nanorod-based pressure sensor arrays: A promising candidate for portable breath monitoring devices. *Nano Energy* **2021**, *80*, 105537.

(9) Fakhri, E.; Sultan, M. T.; Manolescu, A.; Ingvarsson, S.; Svavarsson, H. G. Germanium coated silicon nanowires as human respiratory sensing device. 2022 International Semiconductor Conference (CAS). 2022; pp 163–166, ISSN: 2377-0678.

(10) In, H. J.; Field, C. R.; Pehrsson, P. E. Periodically porous top electrodes on vertical nanowire arrays for highly sensitive gas detection. *Nanotechnology* **2011**, *22*, 355501, Number: 35.

(11) Kwon, Y. J.; Mirzaei, A.; Na, H. G.; Kang, S. Y.; Choi, M. S.; Bang, J. H.; Oum, W.; Kim, S. S.; Kim, H. W. Porous Si nanowires for highly selective room-temperature NO $_2$ gas sensing. *Nanotechnology* **2018**, *29*, 294001, Number: 29.

(12) Qin, Y.; Jiang, Y.; Zhao, L. Enhanced humidity resistance of porous SiNWs via OTS functionalization for rarefied NO_2 detection. *Sensors and Actuators B: Chemical* **2019**, *283*, 61–68.

(13) Li, H.; Zhang, J.; Tao, B.; Wan, L.; Gong, W. Investigation of capacitive humidity sensing behavior of silicon nanowires. *Physica E: Low-dimensional Systems and Nanostructures* **2009**, *41*, 600–604.

(14) Taghinejad, H.; Taghinejad, M.; Abdolahad, M.; Saeidi, A.; Mohajerzadeh, S. Fabrication and modeling of high sensitivity humidity sensors based on doped silicon nanowires. *Sensors and Actuators B: Chemical* **2013**, *176*, 413–419.

(15) Massoud, H. Z. The onset of the thermal oxidation of silicon from room temperature to 1000°C. *Microelectronic Engineering* **1995**, *28*, 109–116.

(16) Huang, Y.-H.; Yen, T.-Y.; Shi, M.-T.; Hung, Y.-H.; Chen, W.-T.; Wu, C.-H.; Hung, K.-M.; Lo, K.-Y. Competition between oxygen and water molecules on SiO2/P-doped Si surface: The electrical dipole evolution on water/oxygen-adsorbed oxide surface. *Sensors and Actuators B: Chemical* **2023**, *376*, 133011.

(17) Morimoto, T.; Nagao, M.; Imai, J. The Adsorption of Water on SiO2, Al2O3, and SiO2 · Al2O3. The Relation between the Amounts of Physisorbed and Chemisorbed Water. *Bulletin of the Chemical Society of Japan* **1971**, *44*, 1282–1288, Publisher: The Chemical Society of Japan.

(18) Konstantinova, E. A.; Osminkina, L. A.; Sharov, C. S.; Timoshenko, V. Y.; Kashkarov, P. K. Influence of NO $_2$ molecule adsorption on free charge carriers and spin centers in porous silicon. *physica status solidi (a)* **2005**, *202*, 1592–1596.

(19) Boarino, L.; Baratto, C.; Geobaldo, F.; Amato, G.; Comini, E.; Rossi, A.; Faglia, G.; Lérondel, G.; Sberveglieri, G. NO2 monitoring at room temperature by a porous silicon gas sensor. *Materials Science and Engineering: B* **2000**, *69-70*, 210–214.

B.2 Fabrication and application of SiNWs based PANI:MOx Heterostructures for Human Respiratory Monitoring

Muhammad Taha Sultan, Anca Dumitru, Elham Aghabalaei Fakhri, **Rachel Elizabeth Brophy**, Snorri Thor Ingvarsson, Andrei Manolescu, H Svavarsson, Fabrication and application of SiNWs based PANI:MO$_x$ Heterostructures for Human Respiratory Monitoring, Journal of Semiconductors (2024). link here

Fabrication and application of SiNWs based PANI:MO$_x$ heterostructures for human respiratory monitoring

Muhammad Taha Sultan,[*,†] Anca Dumitru,[‡] Elham Fakhri,[†] Rachel Brophy,[†]
Snorri Thorgeir Ingvarsson,[¶] Andrei Manolescu,[†] and Halldor Gudfinur Svavarsson[†]

†*Reykjavik University, Department of Engineering, Menntavegur 1, 101, Reykjavik, Iceland*
‡*University of Bucharest, Faculty of Physics, PO Box MG-11, 077125, Magurele, Romania*
¶*University of Iceland, Saemundargata 2, 102 Reykjavík, Iceland*

E-mail: muhammads@ru.is
Phone: +354 (0) 7664317

Abstract

In this study, we investigate an innovative hybrid structure of silicon nanowires (SiNWs) coated with polyaniline (PANI):metal oxide (MO$_x$) nanoparticles, i.e., WO$_3$ and TiO$_2$, for respiratory sensing. To date, few attempts have been made to utilize such hybrid structures for that application. The SiNWs were fabricated using metal-assisted chemical etching (MACE), whereas PANI:MO$_x$ was deposited using chemical oxidative polymerization. The structures were characterized using Raman spectroscopy, X-ray diffraction, and scanning electron microscopy. The sensing characteristics revealed that the hybrid sensor exhibited a considerably better response than pure SiNWs:MO$_x$ and SiNWs:PANI. Such an enhancement in sensitivity is attributed to the formation of a *p*-*n* heterojunction between PANI and MO$_x$, the wider conduction channel provided by PANI, increased porosity in SiNWs/PANI:WO_3 hybrid structures, which creates active sites, increased oxygen vacancies, and the large surface area compared to that available in pure MO_x nanoparticles. Furthermore, less baseline drift and increased sensor stability were established for the SiNWs structure coated with PANI:WO_3, as compared to PANI:TiO_2.

Introduction

Breathing is a vital physiological process in living organisms. For humans, this process involves inhaling air containing oxygen into the lungs, where gas exchange occurs across the alveolar-capillary membrane. Carbon dioxide is excreted during exhalation, released through the nose or mouth. The entire process, from inhalation to exhalation, is known as the breathing or respiration cycle. Respiratory rate, a key vital sign, is used to monitor the progression of illness, with abnormal rates serving as critical markers of serious conditions.

Continuous monitoring of respiratory rate is crucial in various medical settings. Substantial evidence indicates that alterations in respiratory rate can predict potentially serious clinical events, such as cardiac arrest or admission to intensive care units. Studies have shown that respiratory rate is a more reliable indicator than other vital measurements, such as pulse and blood pressure, in differentiating between stable patients and those at risk[1,2]. Changes in respiratory rate can identify high-risk patients up to 24 hours before an event, with a specificity of 95%. Additionally, in the context of COVID-19, respiratory monitoring is critical for evaluating pulmonary function.

Another important area of study is sleep apnea-hypopnea syndrome (SAHS), a prevalent and potentially serious disorder characterized by at least 30 apneas during a typical 7-hour sleep period, where each apnea lasts at least 10 seconds. SAHS leads to sleep interruptions, resulting in various pathophysiological changes, including complications such as hypertension and stroke. SAHS has become the second leading cause of stroke. Therefore, respiratory monitoring of individuals with SAHS is particularly important and urgent[3].

One effective strategy for respiratory monitoring involves using the moisture content in exhaled human breath, where the relative humidity ranges from 60 to 88%[4]. In this context, devices with active materials at the nanoscale have emerged as promising candidates for gas sensing applications due to their high surface-to-volume ratio and small physical dimensions, which are comparable to the charge screening length. A good gas sensor must exhibit high sensitivity and selectivity toward specific gases. Additionally, the sensor should offer long-term stability, repeatability, a low operating temperature, and consequently low power consumption. Furthermore, a cost-effective fabrication process is essential from an industrial perspective.

In this context nanostructures, with their high surface area-to-volume ratio, play a crucial role in advancing sensor performance. Their enhanced surface area provides more active sites for gas adsorption, directly boosting sensor sensitivity. In nanostructured sensors, the small scale of the materials provides stronger interactions with gas molecules, allowing for detectable changes in electrical properties when specific gases are present. For example, one-dimensional nanostructures with particle sizes near twice the Debye length, exhibit enhanced responses due to quantum confinement and the formation of space-charge regions[5]. These unique properties of nanomaterials enable numerous advantages, such as low power consumption, exceptional sensitivity at trace gas concentrations, high accuracy, rapid response times, abundant surface-active sites, and effective operation at room temperature—leading to more efficient and sensitive gas detection compared to their bulk counterparts[6,7].

Nanostructures, such as nanotubes[8], nanoparticles[9,10], nanosheets[11,12], and nanowires[1,13,14], have demonstrated good sensitivity to different gases. Among these nanostructures, silicon nanowires (SiNWs) have have been shown to have substantial advantages[1]. SiNWs can be processed using relatively standard techniques, allowing for integration with complementary metal-oxide-semiconductor (CMOS) processes for large-scale production. Additionally, SiNWs offer flexible doping concentrations and can be chemically functionalized for the selective detection of gas-phase molecules, making them particularly suitable for advanced gas sensing applications. Of several methods to synthesize SiNWs, metal assisted chemical etching provides a simple, cost effective means to fabricate SiNWs while giving control over various parameters for instance length, shape, orientation and doping level[15–17].

Incorporating semiconductor metal oxides (MO_x) provides high electron mobility, high sensitivity, fast response/recovery times, long-term stability, and stable chemical properties[18–20]. Additionally, these materials allow easy adjustment of surface properties. In recent years, n-type semiconducting metal oxides, such as iron oxide, zinc oxide, titanium oxide, tin oxide, tungsten oxide, and indium oxide[9,19–24], have become pivotal in gas sensing due to their low cost, high sensitivity, simplicity, and ease of integration into electronics[18,20]. However, gas sensors based on metal oxides (MO_x) face drawbacks such as high resistance, high operating temperatures, and low selectivity[18–20,25]. The operation of these devices at high temperature tends to alter the properties of nanoparticles over time, thereby causing reduced stability and shorter lifetime. Further the requiring temperature controlled system for these devices requires additional power consumption induces additional cost and complexity. Several work were proposed to improve the metal oxide based sensors performance, such as surface structuring to increase the number of adsorption sites, for instance using porous Si[26].

Another vastly employed approach[27,28] to address these issues, is the use of conducting polymers such as polyacetylene, polypyrrole, polyaniline (PANI), and poly-diacetylene which have been explored[29–32]. These materials offer high conductivity, low-temperature operation, and low power consumption. Among them, PANI has been extensively studied and widely applied[18] due to its efficiency in gas sensing, low cost, easy synthesis, room-temperature operation, and low power consumption. However, conducting polymer-based gas sensors suffer from poor stability, selectivity, and long response times[24,25,30,33].

Hybrid nanocomposites of metal oxides and conducting polymers present a promising solution to enhance the gas-sensing properties of the individual components while maintaining their unique desirable properties. Recent advancements have led to the successful development of PANI-based hybrid nanocomposites by several research groups for detecting various target gases[18,20–22,33,34].

Therefore, we propose an innovative approach: the synthesis of SiNW-based PANI:metal-oxide hybrid nanocomposite structures for respiratory sensing. In this work, SiNWs were synthesized using metal-assisted chemical etching, followed by coating with an organic-inorganic sensing layer comprising PANI and MO_x nanoparticles (MO_x-NPs). The breath sensor operates on a chemisorption-based mechanism, where the target gases (such as those in exhaled breath) interact with the sensor surface, causing a measurable change in resistance. This chemisorption involves the chemical interaction of gas molecules with the active surface of the sensor, leading to electron exchange, which modifies the overall conductivity of the material. When exposed to exhaled gases, each component of the sensor (metal oxide, PANI, and SiNWs) plays a unique role in enhancing the sensitivity, stability, and selectivity of the sensor. The metal oxides nanoparticles provides high sensitivity to gas molecules, particularly oxidizing and reducing gases, due to its natural tendency to interact with oxygen and other gas species. When exposed to gases like CO_2, O_2, or volatile organic gases (VOCs) in the breath, the MO_x surface adsorbs these molecules, leading to electron transfer reactions that alter the material's resistance. The incorporated PANI, which is is known for its high sensitivity to changes in the environment, particularly to acidic and basic gases enhances sensitivity and provides additional active sites for gas interaction[27]. The SiNWs contributuion is a high surface-to-volume ratio[26], increasing the overall surface area available for gas interactions. The SiNW provides structural support and stable electrical conductivity, ensuring a robust signal even under varied respiratory conditions. This approach aims to leverage the combined advantages of both materials, potentially leading to significant improvements in respiratory sensing capabilities.

Experimental

Synthesis of SiNWs

Synthesis of arrays of random SiNWs were carried out by applying metal (silver, Ag) assisted chemical etching (MACE) on *p*-type 10×10 mm^2 single-side polished Si-substrate of 525 µm thick, with the resistivity ρ of 0.1-0.5 Ωcm and 0.009 Ωcm. The process steps of the synthesis (shown schematically in Figure 1) are as follows:

- Deposition of Ag-NPs by immersing Si-substrates in a solution of 3 M HF and 1.5 mM $AgNO_3$ for 60 s, followed by rinsing in DI-water.

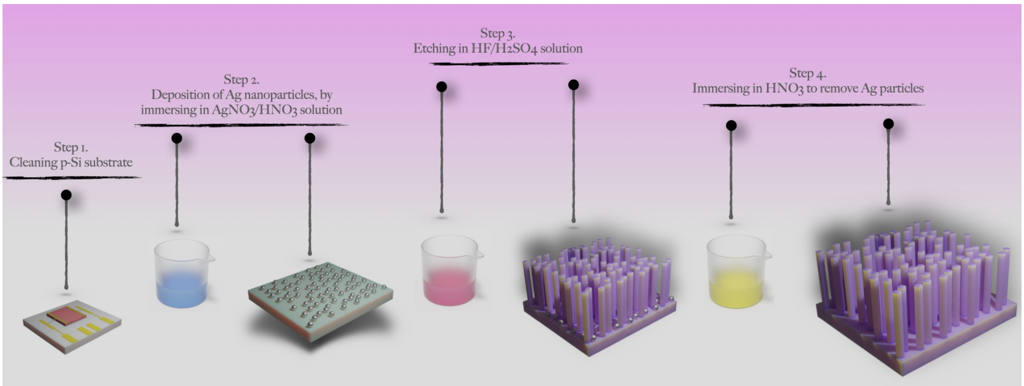

Figure 1: Schematic representation of randomly aligned vertical SiNWs using MACE.

- Etching the resulting sample from the previous step in HF:H_2O_2 (5M:0.4M) solution for 20 min to obtain vertically aligned SiNWs. The etching was abrupted by immersing the sample in DI-water.
- The resulting structure is immersed for few seconds in 60% of nitric acid to remove residual Ag-NPs, and rinsed afterwards with DI-water.

Various schemes of structures are considered in this study (see Figure 2(a-c) for schematics), one in which SiNWs are coated with PANI, polyaniline MO_x hybrid nanocomposite and spin-caoted MO_x-NPs, respectively.

SiNWs decorated with MO_x-NPs

TiO_2 (a mixture of anatase and rutile phases, with particle size < 100 nm) and WO_3 (particle size of ≈ 100 nm) nanopowders from Sigma Aldrich were used for deposition of MO_x-NPs onto SiNWs structures. Initially the nanopowders were dispersed in dimethylformamide (DMF) solvent (0.01 g/ml) and then the solution was sonicated for an hour. A spin coater was used to coat the SiNWs with prepared nanoparticles suspension. The coated sample was placed on a hot-plate at 90°C for 10 min to evaporate the solvent.

SiNWs decorated with PANI:MO_x hybrid nanocomposite - heterostructure

PANI and PANI:MO_x nanocomposites were deposited on SiNWs by suspending the substrate in the polymerization solution, during chemical oxidative polymerization of aniline with ammonium persulfate (APS) in acidic medium[35]. For PANI deposition, SiNWs were immersed in the solution containing 0.1 M aniline in 0.1 M H_2SO_4 and kept for 30 min under continuous stirring conditions. A pre-cooled solution of 0.1 M APS in 0.1 M H_2SO_4 was added, drop by drop, to the above obtained previous solution containing the monomer. The polymerization solution was allowed to react for 24 h at room temperature under continuous stirring condition. The resulting precipitate, and SiNWs, were collected and washed several times with deionized water and methanol. The collected powder was dried at 60 C overnight while the SiNWs decorated with PANI was dried at room atmosphere. Similar procedure was used for deposition of PANI:MO_x nanocomposites on SiNWs with the addition of 0.28 g of TiO_2 or 2.31 g of WO_3 in the monomer solution. An additional glass substrate was placed alongside the sample, for Raman spectroscopy and XRD analysis.

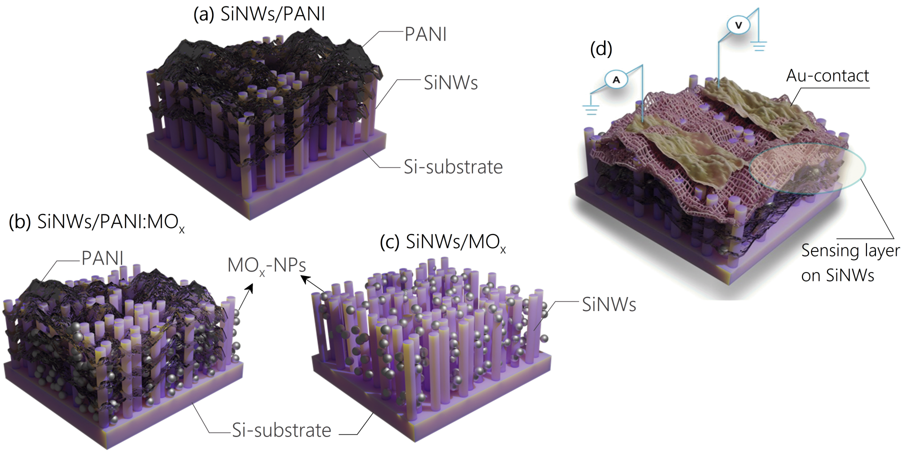

Figure 2: Representation of structural schemes considered for respiratory sensing mechanism, i.e., (a) SiNWs with PANI, (b) SiNWs with MO$_x$ particles and (c) SiNWs coated with hybrid PANI:MO$_x$ nanocomposite.

Characterization

Structural and elemental characterization of the films was conducted using X-ray diffraction Raman spectroscopy (Horiba LabRam Evolution) and scanning electron microscopy (SEM) (Zeiss Supra 35). Empyrean diffractometer by Panalytical was utilised for XRD in a parallel beam geometry with a line-focused copper anode source operating at 45 kV and 40 mA with radiation Cu-Kα (wavelength of 1.54 Å). A parabolic x-ray mirror was used with a $1/2°$ divergence slit to limit the x-ray spot size on the sample. A parallel plate collimator slit (0.27°) was used in the diffracted beam path followed by a PIXcel detector operating in open-detector mode for XRD and in frame-based mode for reciprocal space mapping (RSM). The X-ray diffraction measurement was performed for 2θ selected scanning range i.e., 10 ° - 50° for PANI coated structures and 20° - 80° for PANI:MO$_x$ structures. Where as, ω:2θ with scanning range of 4° was performed for RSM measurements. Raman spectroscopy analysis was made using an air-cooled frequency-doubled Nd:Yag (100 mW / 1 MHz) with 532 nm excitation line along with an 1800 mm high resolution grating. Each Raman measurement was composed of 20 integrated spectra with an acquisition time of 10 s each. The laser power setting was adjusted to 10% in order to avoid any heating effects during measurements. For sensing characterization the samples were coated with Au-contacts (120 nm thick) in co-planar configuration of 2 × 10 mm^2 using electron beam deposition method. A schematic representation of structure with metal contacts is shown in Figure 2(d). The electrical characterization setup contains a source meter (Keithley 2400), a controlled sample stage with a micro-manipulator, vacuum suction and stainless-steel contact arms connected to source meter.

Results and discussion

Structure characterization

Prior to deposition, MO_x nanoparticles (Sigma Aldrich) were characterized by Raman spectroscopy (see Figure 3). The Raman spectra of WO_3 nanoparticles showed well-resolved peaks at 248 and 310 cm^{-1}, ascribed to O-W-O bending, and at 695.8 and 789.5 cm^{-1}, attributed to O-W-O stretching[36]. As expected, the Raman spectra of TiO_2 nanoparticles consist of a mixture of rutile and anatase phases, as indicated by the solid and dashed lines, respectively. Three characteristic active modes, i.e., E_g, B_{1G}, and A_{1G}, for both a-TiO_2 and r-TiO_2, were observed and are in line with other studies[37,38].

A room-temperature Raman spectra of PANI, PANI:WO_3, and PANI:TiO_2 structures are presented in Figure 4. The representative Raman spectra of the structures were deconvoluted using Gaussian fitting to determine the characteristic Raman shifts. For PANI, the vibration modes observed at 1574 cm^{-1} correspond to C=C stretching vibration of the quinoid ring, while 1494 cm^{-1} is assigned to the C-N stretching vibration, and 1330 cm^{-1} is associated with C–N stretching vibration of semiquinone radicals, indicating the synthesis of the conductive form of PANI[35,39]. The room-temperature Raman spectra of PANI:MO_x structures are shown in the same figure. The characteristic peaks associated with WO_3 and TiO_2 were clearly observed, in relation to those shown in Figure 3, along with the simultane-

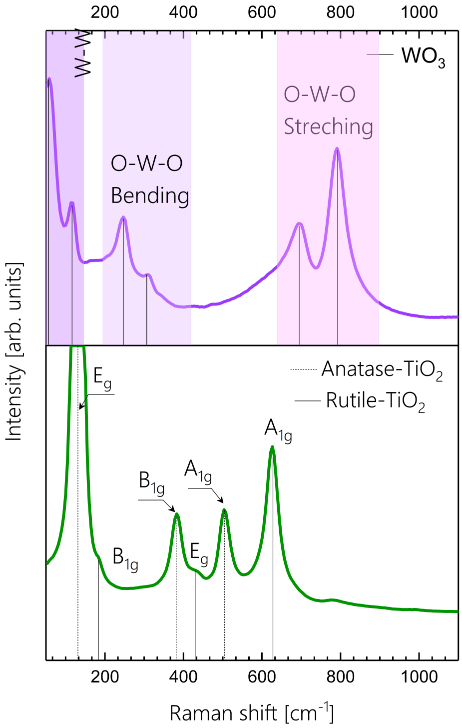

Figure 3: Room temperature Raman spectra of WO_3 and TiO_2 nanopowder. The respetive peaks are marked for both WO_3 and TiO_2, respectively. In (b) the dotted line represents the Raman modes of anatase TiO_2 whereas the solid line represents rutile TiO_2.

ous presence of peaks attributed to PANI. Raman spectra of the obtained hybrid composite showed slight alteration in peaks corresponding to vibration modes in PANI, with no evident formation of new phase, due to the interaction of PANI with MO_x nanoparticles, confirming the polymerization and successful formation of composite structure. Further, an overlap of the PANI vibration modes to that from WO_3 can be identified in the Figures.

The structural analysis of SiNWs/PANI, SiNWs/PANI:WO_3, and SiNWs/PANI:TiO_2 was further conducted using grazing incidence X-ray diffraction (GIXRD), and the results are shown in Figure 5. Due to the perpendicular and parallel periodicity of PANI chains, the XRD pattern of PANI exhibits two broad peaks located at 19.4° and 25.47° 2θ values, attributed to (020) and (200) crystallographic planes of PANI[35]. For WO_3 and r- and a-TiO_2, the peaks are positioned at standard tabulated values according to JCPDS nos. 98-007-1692, 00-021-1276, and 00-021-1272, respectively[37,38,40], with higher peak intensities indicating the preferred crystallographic orientations. As an example, for WO_3, the peak around $2\theta \sim 29°$ corresponding to (120) plane is attributed to monoclinic phase. The broadening of peaks observed in case of MO_x nanoparticles, is attributedto the presence of small nanoparticles with mixed crystal grains and the presence of defects in the nanoparticles[41,42].

Additionally, to investigate the structural features of SiNWs, X-ray reciprocal space maps (RSMs) around the Si (004) reciprocal lattice point were performed, providing information regarding the out-of-plane lattice, strain, and crystal imperfections[43]. The X-ray RSMs along (q_z, q_x) coordinates for SiNWs alone and those coated with PANI are presented in Figure 6(a, b). The q_x and q_z coordinates are the projections of the scattering vector along [100] and [001] directions, given by: $q_x = 2\sin(\omega - \theta)/\lambda$ and $q_z = 2\sin(\theta)/\lambda$.

For SiNWs, an intense peak is located around $q_z \in (0.7360 - 0.7365)$ Å^{-1}. For a cubic crystal, the lattice constant a can be expressed as $a = 4/q_z$[44], and is calculated to be 5.43 Å, which corresponds to the lattice parameter of bulk Si. This confirms that the MACE

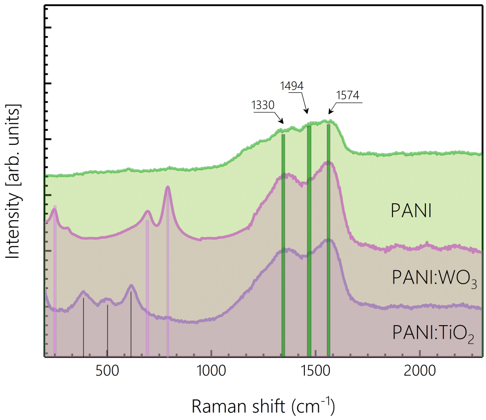

Figure 4: Room temperature Raman spectra of SiNWs structure coated with PANI, PANI:WO_3 and PANI:TiO_2. The Raman peaks are marked for PANI and that for WO_3 and TiO_2, respectively.

process used to obtain SiNWs does not affect the lattice parameter. For SiNWs coated with PANI, the spot broadening increases in both the q_z and q_x directions, which can be ascribed to bending and torsion acting on the SiNWs due to higher surface energy. Furthermore, the elongation of the q_x area in the RSM for these structures, which is related to diffuse scattering, is observed and can be associated with crystal imperfections. A wider angular dispersion for SiNWs/PANI is also observed.

The q_x and q_z coordinates are the projections of the scattering vector along [100] and [001] directions, and are given by: $q_x = 2\sin(\omega - \theta)/\lambda$ and $q_z = 2\sin\theta/\lambda$.

Scanning electron microscopy analysis

Figure 7 shows the top and cross-sectional views of the SiNWs structures, both uncoated and those coated with PANI, PANI:MO$_x$, and spin-coated with MO$_x$ nanoparticles (MO$_x$-NPs). The length of the nanowires was measured to be approximately 6.5 μm, with diameters ranging between 20 and 50 nm (Figure 7(a)), depending on the size distribution of Ag particles obtained during deposition using $AgNO_3$. For SiNWs (Figure 7(a, b)), the SEM images revealed vertically aligned, randomly distributed nanowires bundled together due to the capillary effect induced by wetting, as is evident in Figure 7(b). For structures coated with PANI (Figure. 7(c)), the top view showed a cauliflower-like morphology of PANI, similar to that obtained in the study by Lascu *et al.*[35].

Figure 7(d, e, f) shows cross-sectional and top views of PANI:TiO_2 and PANI:WO_3 structures. It was observed that compared to PANI:WO_3, SiNWs coated with PANI:TiO_2 showed agglomeration of TiO_2 nanoparticles over the surface of PANI. Furthermore, the deposition of PANI:MO$_x$ on SiNWs resulted in increased surface coverage, i.e., a possible increase in nanowire bundling, as supported by the RSM plot showing an increased q_x value.

For SiNWs structures spin-coated with WO_3 nanoparticles, SEM images are shown in Figure 7(g, h). Agglomerated WO_3 nanoparticles can be seen on the SiNWs surface, while the top view reveals smaller particles that infiltrated the nanowires.

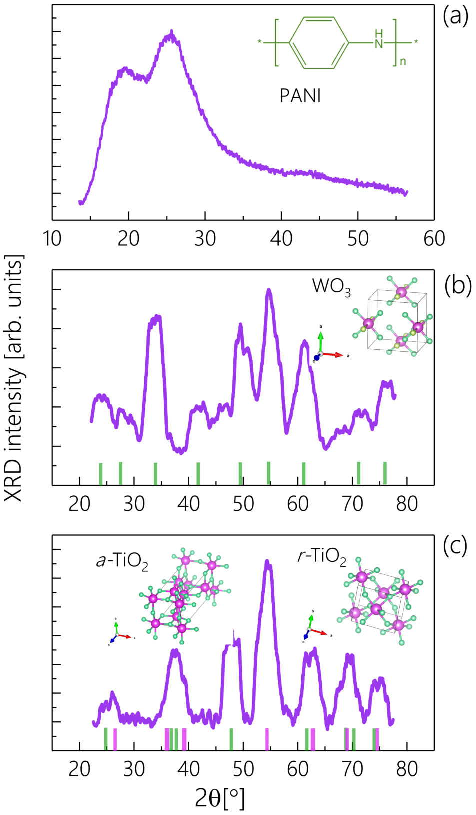

Figure 5: XRD diffractogram for (a) polyaniline (b) WO_3 nanopowder and TiO_2 nanopowder. The green indicated line in (b, c) represents the standard tabulated position of WO_3 and anatase (a-TiO_2) and the red indicated line in (c) represents the standard tabulated position for rutile(r)-TiO_2, according to JCPDS no. 98-007-1692,00-021-1272 and 00-021-1276, respectively.

Electrical Characterization

Human respiration involves a complex mixture of gases, including nitrogen, oxygen, carbon dioxide, and water vapor, which can cause minor variations in temperature and pressure[45,46]. Silicon nanowires (SiNWs) have demonstrated a significant piezoresistive (PZR) effect, particularly in low-pressure environments, making them highly suitable for bio-compatible ap-

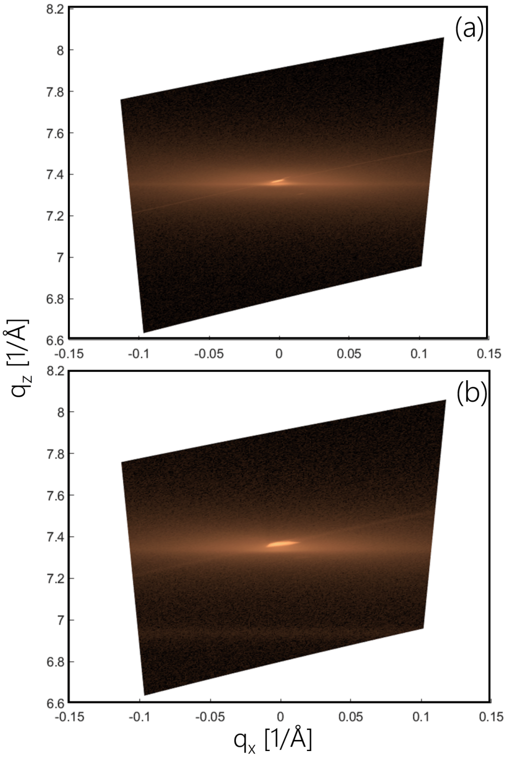

Figure 6: Reciprocal space map of SiNWs and SiNs with PANI along (0 0 4) crystallographic plane.

plications like breath sensors[47–49]. This suggests that the sensing mechanism in breath sensors is likely influenced by both piezoresistive responses and humidity effects. For instance, Gosh *et al.*[50] developed a breath sensor using arrays of n-type silicon nanorods, attributing its functionality to the PZR effect. According to PZR theory, pressure changes, such as those caused by airflow over the SiNW surface, can deform the nanowires, leading to changes in their electrical resistance[47]. In this study, however, the focus is on analyzing the breath-sensing mechanism with respect to chemisorption on the sensing materials, without considering the effects of pressure changes. Additionally, while the structure conceptually targets respiratory gases like oxygen, carbon dioxide, and VOCs, the primary objective was not to examine the effect of these individual gases or VOCs on sensor performance. How-

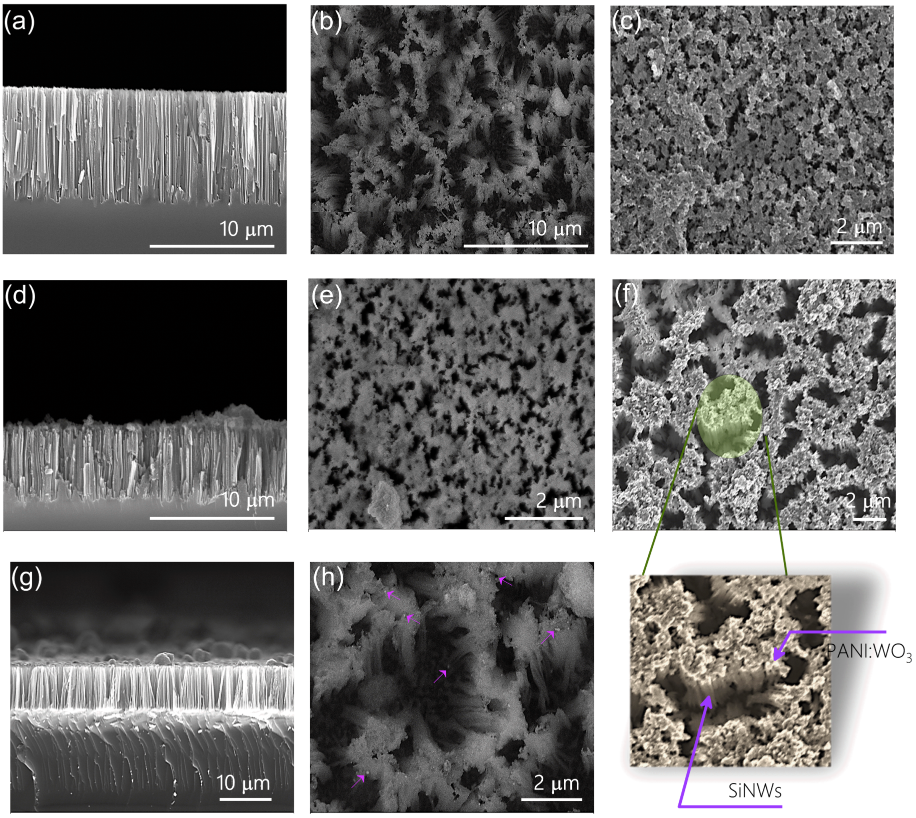

Figure 7: SEM microgrpahs (a,b) cross-sectional and top-view of SiNWs structures obtained by MACE, (c) top-view of SiNWs coated with PANI, (d, e) cross-sectional and top-view of SiNWs coated with PANI:TiO_2, (f) top-view of SiNWs coated with PANI:WO_3, along with a magnified image showing the presence of NWs and (g, h)cross-sectional and top-view of SiNWs spin-coated with WO_3, respectively. The scale bars are provided along with each figure.

ever, the primary parameter monitored and controlled during measurement and profiling of breath includes resistance which correlated the interaction between the sensor surface and the fluctuating composition of the inhaled and exhaled breath, i.e., the sensor's ability to detect variations in respiratory patterns (inhalation, exhalation, and pauses in breathing) and establish the sensor's response to different breathing modes. Other parameters considered are the humidity level and the operation temperature. Thus, during the measurements, the humidity level was kept constant to ensure that variations in resistance could be attributed solely to breath detection rather than fluctuations in environmental humidity as PANI and MO_x-based sensors are often highly sensitive to moisture and can introduce noise in the resistance measurements. Further, by maintaining room temperature($\sim 23.5°C$), the study excludes temperature fluctuations as a variable, ensuring that any changes in resistance are due to respiratory interactions and not temperature shifts. It should be mentioned here that the effect of different gases and VOC's are underway to determine the effect and sensitivity of sensor towards specific gases during respiration. For instance in our recent work we have investigated the detection of NH_3, NO_2 gases and the humidity using SiNWs with further exploration aim to study the effect of similar structure presented in this study on selectivity and sensitivity towards VOCs and gases. To facilitate the understanding and effect of humidity, supplementary information provided show effect of varying relative humidity and sensor response for case of SiNWs/WO_3 structure.

Before we delve into the electrical characterization of SiNWs, it is important to understand the sensing mechanism of interconnected silicon nanowires (SiNWs), which operates as follows: to detect respiration, there must be an interaction between moisture and the SiNWs, leading to moisture absorption onto the surface of the SiNWs, facilitated by their highly hydrophilic nature[1,51]. This phenomenon induces changes in the width of the SiNWs' hole accumulation layer (HAL) and surface potential, consequently altering the conductance of the SiNWs (Figure. 8). Since moisture itself is not inherently oxidizing or reducing in this context, in the presence of an oxidizing gas, the gas extracts electrons from the SiNWs' conduction band, narrowing the HAL width[52,53]. Conversely, in the presence of a reducing agent, electrons are released and trapped by oxygen molecules, resulting in a widening of the HAL width[52].

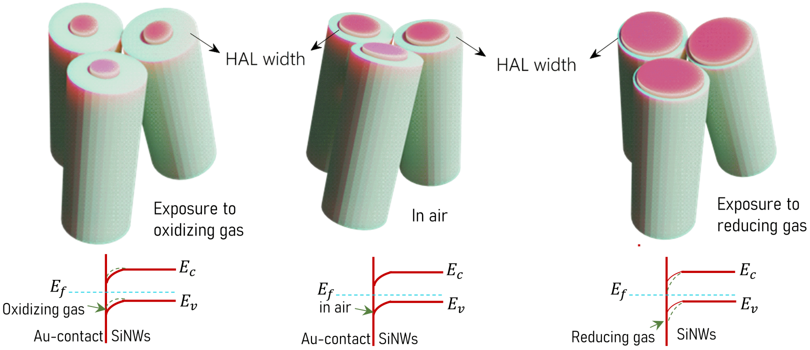

Figure 8: A schematic illustration of SiNWs sensing mechanism based on the bundling with NW-NW junction, demonstrating the modulation in potential barrier in air and during exposure to oxidizing and reducing analyte, respectively.

Expanding on this, moisture in the breath ionizes into hydronium and hydroxide ions, establishing an electric double layer between the moisture and the SiNWs[1,51]. As moisture permeates the nanochannels, it induces electron accumulation in the silicon, causing the electrons to migrate towards the anode, in association with holes generated at the cathode. The unique forest-like morphology of SiNWs, coupled with their large surface area, significantly influences the sensor's response[1]. In our previous work, we studied respiratory sensing using SiNWs obtained by MACE, which demonstrated a reasonable response to human breath. In this study, we aimed to enhance respiratory sensing properties by using SiNWs decorated with PANI and PANI:MO$_x$ hybrid nanocomposites.

The electrical characterization of the structures was carried out using a custom-built setup. For respiratory sensing, the distance between the sample and the human nose was ∼3 mm. Three common respiratory profiles—normal breathing (NB), tachypnea (TB, usually more than 20 breaths per minute[54]), and deep breathing (DB)—were monitored. The data acquisition speed was set to ∼1 ms, limited by the equipment. Figure 9 shows the sensitivity

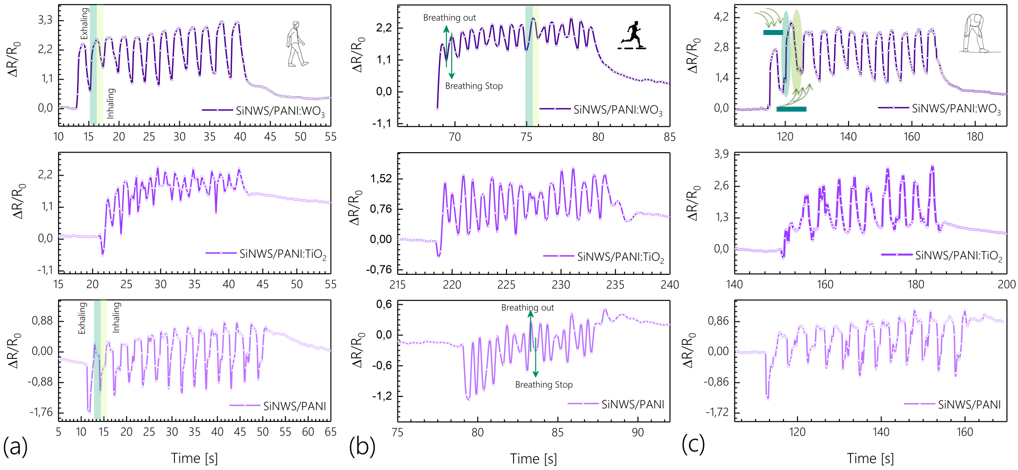

Figure 9: Respiratory sensing for three different breathing patterns i.e., (a-c) normal, rapid and deep breathing, respectively, using SiNWs structures decorated with PANI and PANI:MO$_x$, respectively. The highlighted regions represents the exhaling and inhaling stimulus characteristics.

of the structures by the change in resistance under various respiratory patterns for SiNWs structures coated with PANI, PANI:WO$_3$, and PANI:TiO$_2$. The sensitivity and response time of the structures increased with the introduction of MO$_x$ nanoparticles into PANI, following the order PANI < PANI:TiO$_2$ < PANI:WO$_3$. The response time R_t is defined as:

$$R_t = t_{90\%} - t_{10\%}, \tag{1}$$

where $t_{90\%}$ and $t_{10\%}$ are the times when the change due to external stimuli reaches 90% and 10%, respectively. The calculated R_t values are tabulated in Table 1 and represent average values calculated over several waveform recordings. Moreover, compared to SiNWs structures coated with PANI:WO$_3$, the structures coated with PANI and PANI:TiO$_2$ exhibited distorted features and significant baseline drift, indicating that SiNWs coated with PANI:WO$_3$ possess enhanced sensitivity for respiratory sensing. Notably, the profiles observed for SiNWs coated with PANI exhibited a decrease in resistance during exhalation, contrary to the increase in resistance observed for PANI:MO$_x$ coated structures. This behavior can be understood by the different sensing mechanisms in each structure, which will be discussed later. For better visualization, the exhalation and inhalation phases are highlighted in Figure 9.

The study of breath waveform visualization determines the respiration rate/ frequency, however the effect of flow rate variation during different breath modes might also effect the response of these sensor. Since respiratory rate and flow rate are closely connected because different breathing modes generally involve varying lung activity, which affects both the frequency and flow rate of exhaled gases. In general, the respiratory frequency refers to the number of breaths taken per minute. In our study, the three breathing modes—Normal Breathing (NB), Tidal Breathing (TB), and Deep Breathing (DB)—are characterized by distinct frequencies, with DB generally having a slower frequency than NB and TB, which are higher. For instance in case of SiNW/PANI:WO_3 the frequencies obtained by Fast Fourier transform(FFT) for NB, TB and DB is $\sim$ 0.41, 1.43 ad 0.23 Hz, which is in agreement with previous reports[2,55,56]. Whereas considering flow rate, as the breathing mode changes the lung expansion and contraction dynamics also change, affecting how much air is inhaled and exhaled per breath. For example, deep breathing typically involves a higher tidal volume (volume per breath), which often translates into a higher flow rate during exhalation, even if the respiratory frequency is slower. In case of NB and TB they involve smaller lung volumes and, consequently, lower flow rates per exhalation compared to deep breathing. As the flow rates are not take in to account this study, it is challenging to separate the exact contribution of respiration frequency and flow rate to sensor response. Therefore, the context of their relationship can provide an useful understanding to changes in flow rate likely contributing to differences in sensor response time observed in Table 1. For instance a higher flow rate generally increases the concentration of exhaled gases that reach the sensor per unit time, potentially causing a quicker and stronger resistance change. In contrast, higher respiratory frequency may increase the frequency of resistance fluctuations in response to the breath cycle.

In contrast, a different sensing mechanism occurs in hybrid PANI/MO_x coated SiNWs

Table 1: Response time calculated from Figure 9 for respective structures.

Structures	R_t[s]		
	NB	**TB**	**DB**
SiNWs/PANI	1.32	0.18	1.63
SiNWs/PANI:TiO_2	0.44	0.21	0.68
SiNWs/PANI:WO_3	0.37	0.15	0.45
SiNWs/WO_3	0.45	0.3	1.18
SiNWs	0.72	0.37	1.45

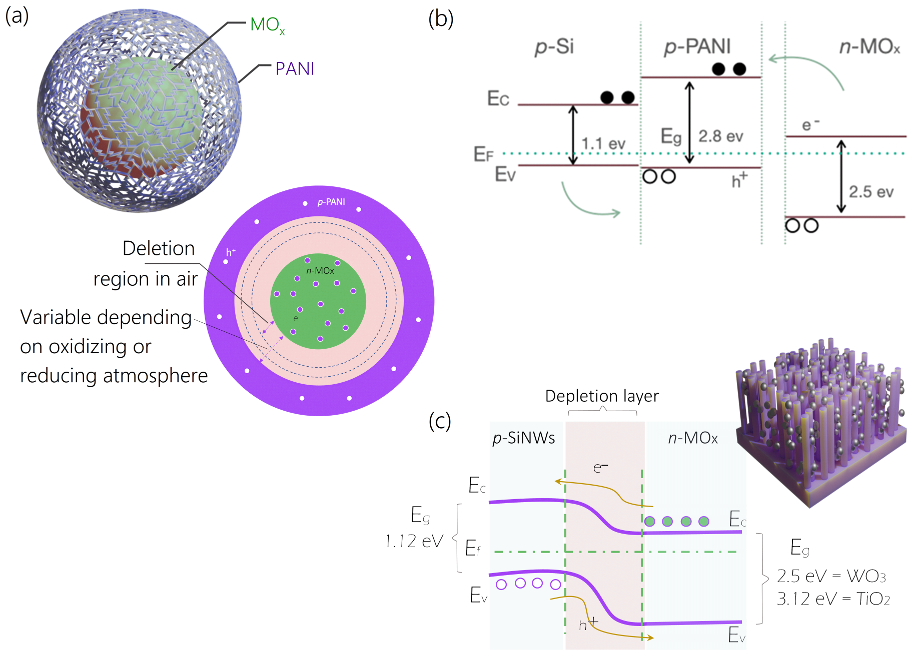

Figure 10: Schematic illustration of (a) $p-n$ junction formation in (a) hybrid $p-$type PANI encapsulating $n-$type MO_x nanoparticles. The Figure demonstrate the depletion layer width alteration in air and in presence of oxidizing or reducing agent. (b) Potential band alignment and charge transfer in p-type SiNWS coated with hybrid of p-PANI:n-WO_3. (c) Energy band with $p-n$ junction formed between $p-$type SiNWs spin coated with $n-$type MO_x nanoparticles.

structures. In this case, the sensing is predominantly based on moisture trapping within the hybrid nanocomposite, leading to changes in surface resistance when molecular species adsorb and react with the material. While pure metal oxide-coated SiNWs exhibit high sensitivity, PANI/MO_x coated structures are more porous due to the presence of MO_x nanoparticles within the PANI matrix. This porosity provides active centers that enable localized donor and acceptor states[20]. An interesting aspect of these structures is the formation of $p-n$ heterojunctions between p-type PANI and n-type MO_x particles[20,24]. When exposed to moisture, electron and hole transfer between PANI and WO_3 or TiO_2[57] forms a depletion layer at the PANI/WO_3 interface, resulting in the creation of a heterojunction barrier[18,20] (illustrated in Figure 10). PANI, being a p-type material, has holes as majority charge carriers. Upon moisture exposure, free electrons neutralize the holes, reducing the hole concentration in PANI that increases the heterojunction potential barrier, leading to a rise in resistance in the hybrid structure[20,24]. As a consequence, this is increasing the overall resistance of the structure. Further, since the conduction band of WO_3 is at higher energy level than that of PANI and Si, the electron will transport form high energy to lower energy region, that is the p-type Si will interact p-type PANI, while the hybrid sensing layer, potentially influencing carrier redistribution and overall device characteristics.

The increased sensitivity observed in PANI:WO_3 can be attributed to WO_3's high sensitivity to gas molecules, such as oxygen, ammonia, nitrogen oxides (NO_x), and other volatile organic compounds (VOCs) present in exhaled breath. WO_3's ability to detect low concentrations of these gases enhances its effectiveness for respiratory sensing applications. In contrast, while TiO_2 is also sensitive to gas molecules, it generally performs better under UV light due to its photocatalytic properties[57–60]. WO_3 has a larger surface area and more active sites for gas interaction compared to TiO_2, which has fewer active sites for gas interaction under room temperature and normal light conditions[59,61].

For comparison, a room-temperature dR/dt vs. time plot for SiNWs/PANI:WO_3 and bare SiNWs is shown in Figure 11(a). The hybrid structures demonstrate a higher rate of change over time, suggesting greater sensitivity to breath profile variations than bare SiNWs. In addition, bare SiNWs show baseline drift (inset), implying reduced stability compared to hybrid structures, which display minimal drift. The response times are tabulated in Table 1. It is important to note that for bare SiNWs, physical deformation due to inhalation or exhalation pressure could influence resistance through the piezoresistive effect[47,50]. In contrast, the hybrid layer stabilizes the nanowires, preventing deformation and ensuring that changes in resistance are mainly due to chemisorption rather than physical pressure effects, unlike in the bare SiNWs where both factors may influence the resistance.

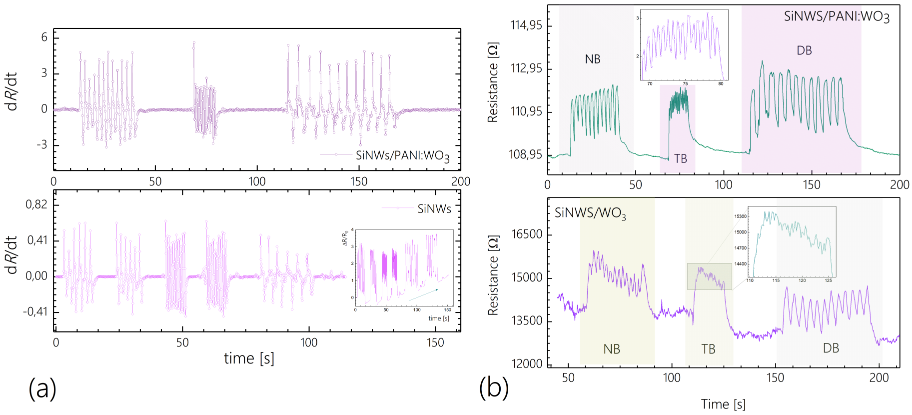

Figure 11: (a)Room temperature plot of dR/dt for SiNWs structure with and without hybrid PANI:WO$_3$ deposition, respectively. The inset in shows the resistance vs time plot of SiNWs with arrow representing a drift in baseline.(b)Plot for room temperature change in resistance as a function of time under varying breathing stimulus using SiNWs structures decorated with (top) PANI:WO$_3$ using electroless deposition and (bottom) WO$_3$ nanoparticles using spin-coating, respectively. The insets show magnified pattern under rapid breathing.

A further comparison between SiNWs decorated with PANI:WO$_3$ and those spin-coated with WO$_3$ nanoparticles (Figure 11(b)) reveals that the introduction of a semiconducting polymer composite with WO$_3$ leads to lower resistance and faster response times. The R_t values for SiNWs structures decorated with PANI:WO$_3$ and WO$_3$-NPs are approximately 0.37 s, 0.15 s, and 0.45 s for NB, TB, and DB respiratory patterns, respectively, compared to 0.43 s, 0.30 s, and 1.18 s for the spin-coated WO$_3$ structure. The enhanced response time is attributed to the uniform distribution and adherence of PANI:WO$_3$ between interconnected nanowires, unlike the agglomerated WO$_3$ particles seen in spin-coated structures, which have less adherence and functionalization.

To explain the sensing mechanism in n-type WO$_3$ and TiO$_2$ metal oxides, the adsorption

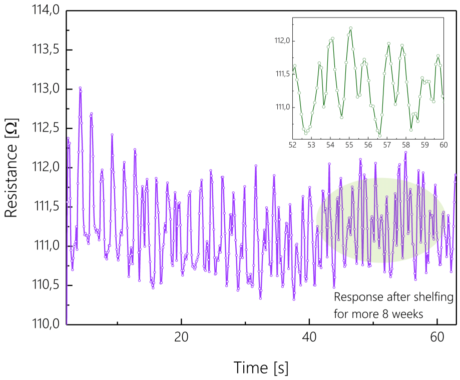

Figure 12: Response of the structure (SiNWs/ PANI: WO_3) after shelving for more than two-months.

and desorption of molecules on the sensor surface lead to changes in resistance. Oxygen molecules in the air react with surface electrons, decreasing electron concentration on the WO_3 surface and increasing the width of the depletion regions[18,19], thereby increasing sensor resistance (Figure 10).

In the case of SiNWs/MO_x structures, the sensing mechanism involves the formation of a junction between p-type SiNWs and n-type MO_x nanoparticles, modulating the sensing behavior of the nanowires. As documented by[1], the dominant conductive path is the interconnected SiNWs, with charge carrier diffusion occurring at the interface between the SiNWs and MO_x nanoparticles due to differences in the Fermi levels[62]. This leads to the formation of a depletion region with an internal electric field at the interface. When O_2 molecules are adsorbed on the surface, electrons are extracted, increasing the hole concentration in p-type SiNWs and disrupting the balance in the depletion layer. This results in a positive charge layer that impedes hole diffusion from p-type SiNWs to MO_x, thus reducing the thickness of the depletion layer[62,63].

Returning to the comparison between the hybrid and MO_x SiNWs structures, as observed in Figure 11, the hybrid structure, which combines cauliflower-like PANI with WO_3 nanoparticles, demonstrated an increased response with more detailed features. This improvement

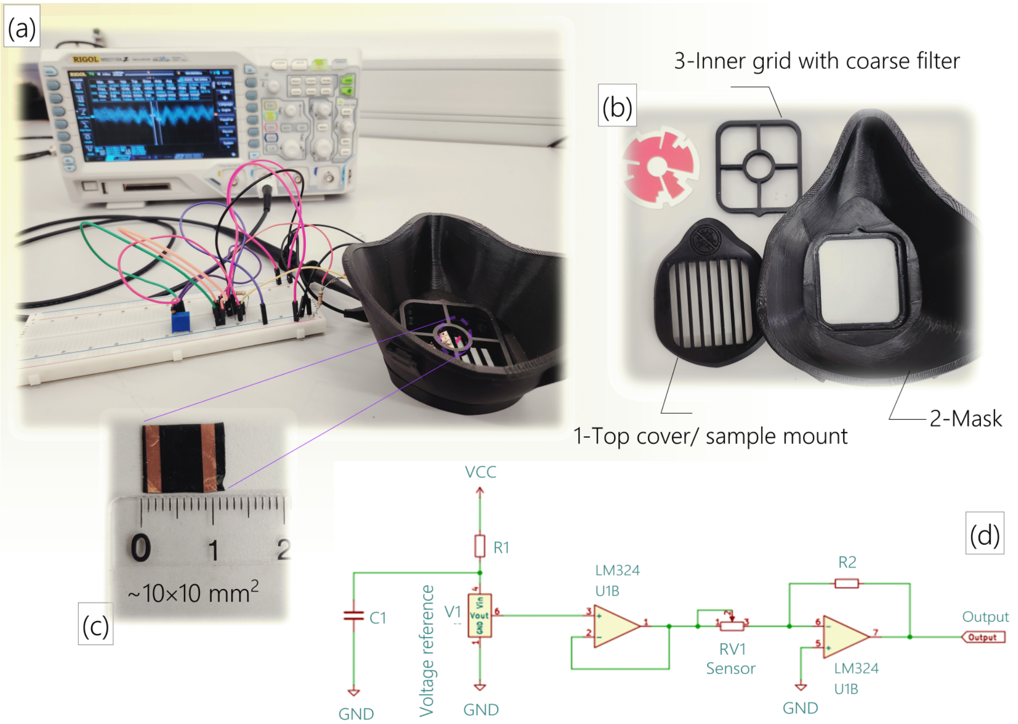

Figure 13: (a) Photograph of data acquisition electronics, utilizing an oscilloscope, assisted with Arduino microcontroller board(not shown here). (b) 3D printed mask with a outer cover for mounting sample and an inner grid which can can integrated with course filter for damage protection. (c) Sample before mounting with size $\sim$10$\times$10 mm^2. (d)Circuit diagram of breath sensor.

can be attributed to the larger surface area of the PANI:WO_3 composite compared to pure WO_3, allowing for greater molecule adsorption and enhanced sensitivity. Additionally, the acidified PANI, a conductive polymer, has a wider conduction channel, leading to lower resistance in the hybrid structure compared to SiNWs/MO_x, as illustrated by the plots in Figure 11 and consistent with observations from He *et al.*[18]. The hybrid structure also contains more oxygen vacancies than pure WO_3, which facilitates the adsorption of gas molecules. Moreover, as noted by Staerz *et al.*[64], nanoparticle agglomeration (as seen in Figure 7) can reduce sensitivity. This issue has been addressed through the use of templates[65] and will be further explored by adjusting the concentration of nanoparticles in solution, the length and density of SiNWs, and the parameters of the spin-coating process. The structure presented in the current study, especially SiNWs coated with hybrid PANI:WO_3, showed increased rate of change in resistance compared to those observed in other works[55,66]. The encapsulation of MO_x nanoparticles in PANI resulted in much lower resistance for instance as observed for hybrid structure i.e., SiNW/ZnO/rGO[55], and to mention that the voltage applied i.e, translating to the power consumption is much lower than those observed in previous works[2,55,56].

To investigate the stability of the sensor, the structure was stored for more than 2 months in an ambient atmosphere with a variation in relative humidity between 36±3%, while the temperature during that period did not change significantly i.e., 23.5°C. It is well acknowledged that PANI is chemically stable[66–68] and that the incorporation of WO_3 nanoparticle along with PANI (both of which posses minimal toxicity[68,69]) on to SiNWs forming a immobilized solid state device ensures sensing materials remain in place, providing stable and reliable sensing performance while reducing health risks associated with airborne particles or degradation products. After this period, measurements showed negligible changes in resistance or deterioration in the observed respiratory profile (see Figure 12). In efforts to develop practical solutions for real-time monitoring of breathing patterns, we designed a breath sensor (see Figure 13). This device features a mask equipped with the sensor and shielded by a grid for optimal performance and protection against potential damage. A photograph of the circuit and the circuit diagram are included in the Figure Data acquisition is conducted using an oscilloscope and an Arduino microcontroller board (not shown here) for recording the data. Additionally, the sensors will be encapsulated and/or coated for instance with polyamide coating to prevent possibility of (if any) airborne particles or flakes from the structures, as also conducted in work by Ghosh *et. al.*[50]

Outlook

We have successfully demonstrated the synthesis of a hybrid PANI:MO$_x$ structure decorated on SiNWs, using a cost-effective and straightforward chemical oxidative polymerization method for respiratory sensing applications. The structure was characterized using Raman spectroscopy, X-ray diffraction (XRD), and reflection spectroscopy microscopy (RSM), which confirmed the presence of PANI encapsulating metal oxide nanoparticles, specifically WO$_3$ and TiO$_2$. SEM micrographs revealed the formation of vertically aligned, randomly distributed silicon nanowires covered with a porous PANI:MO$_x$ structure.

Comparative analysis of SiNWs structures coated with PANI or WO$_3$ alone showed that those coated with PANI:MO$_x$ hybrid composite exhibited superior performance in respiratory sensing across various breathing profiles at room temperature. In particular, the PANI:WO$_3$-coated structures demonstrated enhanced sensitivity and response time with minimal to no baseline drift. These findings underscore the promising potential of hybrid PANI-based sensors for both research and industrial applications. Their low fabrication cost, scalability, and ease of manufacture make them a viable option for developing efficient respiratory sensing technologies.

Acknowledgement

This work was supported by the Icelandic research fund, grant no. 239987-051, and Landsvirkjun-The Energy Research Fund grant no.: NÝR-29-2024. The authors thanks Hannes Pall Thordarson for his assistance and guidance in developing a circuit for the respiratory sensing device.

References

(1) Akbari-Saatlu, M.; Procek, M.; Mattsson, C.; Thungström, G.; Nilsson, H. E.; Xiong, W.; Xu, B.; Li, Y.; Radamson, H. H. Silicon Nanowires for Gas Sensing: A Review. Nanomaterials 2020, Vol. 10, Page 2215 **2020**, 10, 2215.

(2) Yu, S.; Zhang, H.; Zhang, J.; Hu, Z. High-sensitivity RGO-TiO_2 Humidity Sensor Driven by Triboelectric Nanogenerators for Non-Contact Monitoring of Human Respiration. Journal of Alloys and Compounds **2023**, 935, 168006.

(3) Andreozzi, E.; Centracchio, J.; Punzo, V.; Esposito, D.; Polley, C.; Gargiulo, G. D.; Bifulco, P. Respiration Monitoring via Forcecardiography Sensors. Sensors 2021, Vol. 21, Page 3996 **2021**, 21, 3996.

(4) Mansour, E.; Vishinkin, R.; Rihet, S.; Saliba, W.; Fish, F.; Sarfati, P.; Haick, H. Measurement of Temperature and Relative Humidity in Exhaled Breath. Sensors and Actuators B: Chemical **2020**, 304, 127371.

(5) C, W.; L, Y.; L, Z.; D, X.; R, G. Metal Oxide Gas Sensors: Sensitivity and Influencing Factors. Sensors **2010**, 10, 2088–2106.

(6) Liu, X.; Cheng, S.; Liu, H.; Hu, S.; Zhang, D.; Ning, H. A Survey on Gas Sensing Technology. Sensors **2012**, 12, 9635–9665, Author to whom correspondence should be addressed.

(7) PK, P.; B, C.; N, P. Recent Advances in Nanostructured Materials for Application as Gas Sensors. ACS Omega **2024**, 9, 3092–3122.

(8) Guo, S. Y.; Hou, P. X.; Zhang, F.; Liu, C.; Cheng, H. M. Gas Sensors Based on Single-Wall Carbon Nanotubes. Molecules 2022, Vol. 27, Page 5381 **2022**, 27, 5381.

(9) Kong, Y.; Li, Y.; Cui, X.; Su, L.; Ma, D.; Lai, T.; Yao, L.; Xiao, X.; Wang, Y. SnO_2

Nanostructured Materials Used as Gas Sensors for the Detection of Hazardous and Flammable Gases: A Review. Nano Materials Science **2022**, 4, 339–350.

(10) Sun, Y. F.; Liu, S. B.; Meng, F. L.; Liu, J. Y.; Jin, Z.; Kong, L. T.; Liu, J. H. Metal Oxide Nanostructures and Their Gas Sensing Properties: A Review. Sensors (Basel, Switzerland) **2012**, 12, 2610.

(11) Ji, F.; Ren, X.; Zheng, X.; Liu, Y.; Pang, L.; Jiang, J.; Liu, S. 2D-MoO_3 Nanosheets for Superior Gas Sensors. Nanoscale **2016**, 8, 8696–8703.

(12) Umar, A.; Alshahrani, A. A.; Algarni, H.; Kumar, R. CuO Nanosheets as Potential Scaffolds for Gas Sensing Applications. Sensors and Actuators B: Chemical **2017**, 250, 24–31.

(13) Comini, E. Metal Oxides Nanowires Chemical/Gas Sensors: Recent Advances. Materials Today Advances **2020**, 7, 100099.

(14) Fakhri, E.; Sultan, M. T.; Manolescu, A.; Ingvarsson, S.; Svavarsson, H. G. Application of p and n-Type Silicon Nanowires as Human Respiratory Sensing Device. Sensors 2023, Vol. 23, Page 9901 **2023**, 23, 9901.

(15) Kale, P.; Sahoo, M. Removal of Ag remanence and improvement in structural attributes of silicon nanowires array via sintering. Scientific Reports **2021**, 11, 24189.

(16) Huang, Z.; Geyer, N.; Werner, P.; de Boor, J.; Gösele, U. Metal-Assisted Chemical Etching of Silicon: A Review. Advanced Materials **2011**, 23, 285–308.

(17) Fakhri, E.; others Synthesis and photoluminescence study of silicon nanowires obtained by metal assisted chemical etching. 2021 International Semiconductor Conference (CAS). 2021; pp 147–150.

(18) He, W.; Zhao, Y.; Xiong, Y. Bilayer Polyaniline-WO_3 Thin-Film Sensors Sensitive to NO_2. ACS Omega **2020**, 5, 9744–9751.

(19) Masuda, Y.; Uozumi, A. Highly Responsive Diabetes and Asthma Sensors with WO_3 Nanoneedle Films for the Detection of Biogases with Low Concentrations. NPG Asia Materials 2023 15:1 **2023**, 15, 1–18.

(20) Kulkarni, S. B.; Navale, Y. H.; Navale, S. T.; Stadler, F. J.; Ramgir, N. S.; Patil, V. B. Hybrid polyaniline-WO_3 Flexible Sensor: A Room Temperature Competence Towards NH_3 Gas. Sensors and Actuators B: Chemical **2019**, 288, 279–288.

(21) Bandgar, D. K.; Navale, S. T.; Naushad, M.; Mane, R. S.; Stadler, F. J.; Patil, V. B. Ultra-Sensitive Polyaniline–Iron Oxide Nanocomposite Room Temperature Flexible Ammonia Sensor. RSC Advances **2015**, 5, 68964–68971.

(22) Bonyani, M.; Zebarjad, S. M.; Janghorban, K.; Kim, J. Y.; Kim, H. W.; Kim, S. S. Enhanced NO_2 Gas Sensing Properties of ZnO-PANI Composite Nanofibers. Ceramics International **2023**, 49, 1238–1249.

(23) Pippara, R. K.; Chauhan, P. S.; Yadav, A.; Kishnani, V.; Gupta, A. Room temperature Hydrogen Sensing with Polyaniline/SnO_2/Pd Nanocomposites. Micro and Nano Engineering **2021**, 12, 100086.

(24) Tian, J.; Yang, G.; Jiang, D.; Su, F.; Zhang, Z. A Hybrid Material Consisting of Bulk-reduced TiO_2, Graphene Oxide and Polyaniline for Resistance Based Sensing of Gaseous Ammonia at Room Temperature. Microchimica Acta **2016**, 183, 2871–2878.

(25) Kumar, R.; Yadav, B. C. Fabrication of Polyaniline (PANI)—Tungsten oxide (WO_3) Composite for Humidity Sensing Application. Journal of Inorganic and Organometallic Polymers and Materials **2016**, 26, 1421–1427.

(26) Mhamdi, H.; Zaghouani, R.; Fiorido, T. e. a. Study of n-WO3/p-porous silicon structures for gas-sensing applications. J Mater Sci: Mater Electron **2020**, 31, 7862–7870.

(27) Chaudhary, V.; Kaur, A. Enhanced room temperature sulfur dioxide sensing behaviour of in situ polymerized polyaniline–tungsten oxide nanocomposite possessing honeycomb morphology. RSC Adv. **2015**, 5, 73535–73544.

(28) Wang, Z.; Lan, K.; Wang, Z.; Wei, J.; Chen, R.; Qin, G. High-performance PANI sensor on silicon nanowire arrays for sub-ppb NH3 detection. Talanta **2025**, 282, 127086.

(29) Jain, A.; Nabeel, A. N.; Bhagwat, S.; Kumar, R.; Sharma, S.; Kozak, D.; Hunjet, A.; Kumar, A.; Singh, R. Fabrication of Polypyrrole Gas Sensor for Detection of NH_3 using an Oxidizing Agent and Pyrrole Combinations: Studies and Characterizations. Heliyon **2023**, 9, e17611.

(30) Khuspe, G. D.; Bandgar, D. K.; Sen, S.; Patil, V. B. Fussy Nanofibrous Network of Polyaniline (PANi) for NH_3 Detection. Synthetic Metals **2012**, 162, 1822–1827.

(31) Huang, J.; Yang, T.; Kang, Y.; Wang, Y.; Wang, S. Gas Sensing Performance of Polyaniline/ZnO Organic-Inorganic Hybrids for Detecting VOCs at Low Temperature. Journal of Natural Gas Chemistry **2011**, 20, 515–519.

(32) Fratoddi, I.; Venditti, I.; Cametti, C.; Russo, M. V. Chemiresistive Polyaniline-Based Gas Sensors: A Mini Review. Sensors and Actuators B: Chemical **2015**, 220, 534–548.

(33) Huyen, D. N.; Tung, N. T.; Thien, N. D.; Thanh, H. L. Effect of TiO_2 on the Gas Sensing Features of TiO_2/PANI Nanocomposites. Sensors (Basel, Switzerland) **2011**, 11, 1924.

(34) Li, S.; Lin, P.; Zhao, L.; Wang, C.; Liu, D.; Liu, F.; Sun, P.; Liang, X.; Liu, F.; Yan, X.; Gao, Y.; Lu, G. The Room Temperature Gas Sensor Based on Polyaniline Flower-Like WO_3 Nanocomposites and Flexible PET Substrate for NH_3 Detection. Sensors and Actuators B: Chemical **2018**, 259, 505–513.

(35) Lascu, I.; Locovei, C.; Bradu, C.; Gheorghiu, C.; Tanase, A. M.; Dumitru, A. Polyaniline-Derived Nitrogen-Containing Carbon Nanostructures with Different Morphologies as Anode Modifier in Microbial Fuel Cells. International Journal of Molecular Sciences 2022, Vol. 23, Page 11230 **2022**, 23, 11230.

(36) Xu, L.; Yin, M. L.; Liu, S. Agx@WO_3 Core-Shell Nanostructure for LSP Enhanced Chemical Sensors. Scientific Reports 2014 4:1 **2014**, 4, 1–7.

(37) Challagulla, S.; Tarafder, K.; Ganesan, R.; Roy, S. Structure Sensitive Photocatalytic Reduction of Nitroarenes over TiO_2. Scientific Reports 2017 7:1 **2017**, 7, 1–11.

(38) Hardcastle, F. D. Raman Spectroscopy of Titania (TiO_2) Nanotubular Water-Splitting Catalysts. Journal of the Arkansas Academy of Science **2011**, 65.

(39) Mousli, F.; Chaouchi, A.; Hocine, S.; Lamouri, A.; Rei Vilar, M.; Kadri, A.; Chehimi, M. M. Diazonium-modified TiO2/polyaniline core/shell nanoparticles. Structural characterization, interfacial aspects and photocatalytic performances. Applied Surface Science **2019**, 465, 1078–1095.

(40) Pakdel, H.; Galstyan, V.; D'Arco, A.; Mancini, T.; Lupi, S.; Moumen, A.; Borsi, M.; Comini, E. Synthesis of WO3 nanopowder using a green surfactant for efficient gas sensing applications. Ceramics International **2023**, 49, 30501–30509.

(41) Pakdel, H.; Galstyan, V.; D'Arco, A.; Mancini, T.; Lupi, S.; Moumen, A.; Borsi, M.; Comini, E. Synthesis of WO3 nanopowder using a green surfactant for efficient gas sensing applications. Ceramics International **2023**, 49, 30501–30509.

(42) Ishida, Y.; Motono, S.; Doshin, W.; Tokunaga, T.; Tsukamoto, H.; Yonezawa, T. Small Nanosized Oxygen-Deficient Tungsten Oxide Particles: Mechanistic Investigation with Controlled Plasma Generation in Water for Their Preparation. ACS Omega **2017**, 2, 5104–5110.

(43) Fewster, P. F. Reciprocal Space Mapping. Critical Reviews in Solid State and Material Sciences **1997**, 22, 69–110.

(44) Stanchu, H. V.; Kuchuk, A. V.; Barchuk, M.; Mazur, Y. I.; Kladko, V. P.; Wang, Z. M.; Rafaja, D.; Salamo, G. J. Asymmetrical Reciprocal Space Mapping using X-ray Diffraction: A Technique for Structural Characterization of GaN/AlN Superlattices. CrystEngComm **2017**, 19, 2977 – 2982.

(45) Tai, H.; Wang, S.; Duan, Z.; Jiang, Y. Evolution of breath analysis based on humidity and gas sensors: Potential and challenges. Sensors and actuators B: chemical **2020**, 318, 128104.

(46) Ates, H. C.; Dincer, C. Wearable breath analysis. Nature Reviews Bioengineering **2023**, 1, 80–82.

(47) Fakhri, E.; Plugaru, R.; Sultan, M. T.; Hanning Kristinsson, T.; Örn Árnason, H.; Plugaru, N.; Manolescu, A.; Ingvarsson, S.; Svavarsson, H. G. Piezoresistance characterization of silicon nanowires in uniaxial and isostatic pressure variation. Sensors **2022**, 22, 6340.

(48) Zhang, S.; Lou, L.; Lee, C. Piezoresistive silicon nanowire based nanoelectromechanical system cantilever air flow sensor. Applied Physics Letters **2012**, 100, 023111.

(49) Kim, C.; Ahn, H.; Ji, T. Flexible Pressure Sensors Based on Silicon Nanowire Array Built by Metal-Assisted Chemical Etching. IEEE Electron Device Letters **2020**, 41, 1233–1236.

(50) Ghosh, R.; Song, M. S.; Park, J.; Tchoe, Y.; Guha, P.; Lee, W.; Lim, Y.; Kim, B.; Kim, S.-W.; Kim, M.; others Fabrication of piezoresistive Si nanorod-based pressure sensor arrays: A promising candidate for portable breath monitoring devices. Nano Energy **2021**, 80, 105537.

(51) Song, Y.; Shu, C.; Song, Z.; Zeng, X.; Yuan, X.; Wang, Y.; Xu, J.; Feng, Q.; Song, T.; Shao, B.; Wang, Y.; Sun, B. Self-Powered Health Monitoring with Ultrafast Response and Recovery Enabled by Nanostructured Silicon Moisture-Electric Generator. Chemical Engineering Journal **2023**, 468, 143797.

(52) Qin, Y.; Jiang, Y.; Zhao, L. Modulation of Agglomeration of Vertical Porous Silicon Nanowires and the Effect on Gas-Sensing Response. Advanced Engineering Materials **2018**, 20, 1700893.

(53) Morganti, D.; Leonardi, A. A.; Faro, M. J. L.; Leonardi, G.; Salvato, G.; Fazio, B.; Musumeci, P.; Livreri, P.; Conoci, S.; Neri, G.; Irrera, A. Ultrathin Silicon Nanowires for Optical and Electrical Nitrogen Dioxide Detection. Nanomaterials 2021, Vol. 11, Page 1767 **2021**, 11, 1767.

(54) Park, S. B.; Khattar, D. Tachypnea. Emergency and Office Pediatrics **2024**, 8, 33.

(55) Lou, C.; Hou, K.; Zhu, W.; Wang, X.; Yang, X.; Dong, R.; Chen, H.; Guo, L.; Liu, X. Human Respiratory Monitoring Based on Schottky Resistance Humidity Sensors. Materials 2020, Vol. 13, Page 430 **2020**, 13, 430.

(56) Kundu, S.; Majumder, R.; Ghosh, R.; Pradhan, M.; Roy, S.; Singha, P.; Ghosh, D.; Banerjee, A.; Banerjee, D.; Chowdhury, M. P. Relative Humidity Sensing Properties of Doped Polyaniline-Encased Multiwall Carbon Nanotubes: Wearable and Flexible Human Respiration Monitoring Application. Journal of Materials Science **2020**, 55, 3884–3901.

(57) Ekande, O. S.; Kumar, M. Review on polyaniline as reductive photocatalyst for the construction of the visible light active heterojunction for the generation of reactive oxygen species. Journal of Environmental Chemical Engineering **2021**, 9, 105725.

(58) Xie, H.; Li, N.; Chen, X.; Jiang, J.; Zhao, X. Surface oxygen vacancies promoted photodegradation of benzene on TiO2 film. Applied Surface Science **2020**, 511, 145597.

(59) Chen, H.; Liu, Y.; Xie, C.; Wu, J.; Zeng, D.; Liao, Y. A comparative study on UV light activated porous TiO2 and ZnO film sensors for gas sensing at room temperature. Ceramics International **2012**, 38, 503–509.

(60) Rahman, K. H.; Kar, A. K. Effect of band gap variation and sensitization process of polyaniline (PANI)-TiO2 p-n heterojunction photocatalysts on the enhancement of photocatalytic degradation of toxic methylene blue with UV irradiation. Journal of Environmental Chemical Engineering **2020**, 8, 104181.

(61) Nunes, D.; Fortunato, E.; Martins, R. Flexible nanostructured TiO2-based gas and UV sensors: a review. Discover Materials **2022**, 2, 2.

(62) Liu, D.; Lin, L.; Chen, Q.; Zhou, H.; Wu, J. Low Power Consumption Gas Sensor Created from Silicon Nanowires/TiO_2 Core-Shell Heterojunctions. ACS Sensors **2017**, 2, 1491–1497.

(63) Qin, Y.; Wang, Z.; Liu, D.; Wang, K. Dendritic Composite Array of Silicon Nanowires/WO_3 Nanowires for Sensitive Detection of NO_2 at Room Temperature. Materials Letters **2017**, 207, 29–32.

(64) Staerz, A.; Weimar, U.; Barsan, N. Understanding the Potential of WO_3 Based Sensors for Breath Analysis. Sensors **2016**, 16.

(65) Kim, S.-J.; Choi, S.-J.; Jang, J.-S.; Kim, N.-H.; Hakim, M.; Tuller, H. L.; Kim, I.-D. Mesoporous WO_3 Nanofibers with Protein-Templated Nanoscale Catalysts for Detection of Trace Biomarkers in Exhaled Breath. ACS Nano **2016**, 10, 5891–5899, PMID: 27166639.

(66) Xu, M.; Wang, Y.; Chen, F.; Wang, J.; Dai, F.; Li, Z. Breathable Nanomesh pressure sensor with layered polyaniline grown at Gas-liquid interface. Chemical Engineering Journal **2022**, 445, 136717.

(67) Wang, X.; Zhang, D.; Zhang, H.; Gong, L.; Yang, Y.; Zhao, W.; Yu, S.; Yin, Y.; Sun, D. In situ polymerized polyaniline/MXene (V2C) as building blocks of supercapacitor and ammonia sensor self-powered by electromagnetic-triboelectric hybrid generator. Nano Energy **2021**, 88, 106242.

(68) Beygisangchin, M.; Baghdadi, A. H.; Kamarudin, S. K.; Rashid, S. A.; Jakmunee, J.; Shaari, N. Recent progress in polyaniline and its composites; Synthesis, properties, and applications. European Polymer Journal **2024**, 210, 112948.

(69) Han, B.; Popov, A. L.; Shekunova, T. O.; Kozlov, D. A.; Ivanova, O. S.; Rumyantsev, A. A.; Shcherbakov, A. B.; Popova, N. R.; Baranchikov, A. E.; Ivanov, V. K. Highly Crystalline WO3 Nanoparticles Are Nontoxic to Stem Cells and Cancer Cells. Journal of Nanomaterials **2019**, 5384132.

Bibliography

[1] S. Bhattacharya and S. John, “30% conversion efficiency in silicon solar cells: A numerical demonstration,” *Sci Rep*, 2009.

[2] S. E. Basics, Tech. Rep., 2024.

[3] L. Fraas, “Solar cells, single-crystal semiconductors, and high efficiency,” *Solar Cells and their Applications*, 2010.

[4] M. G. M. S.R Wenham, *Applied Photovoltaics*. Earthscan, 2011.

[5] A. Hadipour, B. De-Boer, and P. W. M. Blom, “Organic tandem and multi-junction solar cells,” *Advanced Functional Materials*, 2008.

[6] A. VR, “The ultimate guide to semiconductor junctions,” Republic Of Solar, Tech. Rep., 2022.

[7] A. M. Bagher, “Types of solar cells and application,” *American Journal of Optics and Photonics*, 2015.

[8] E. F. Asrori Asrori Fatur Fatur, “The design and performance investigation of solar e-bike using flexible solar panel by different battery charging controlle,” *International Journal of Mechanical and Production*, 2020.

[9] M. T. Adil Baiju, “Status and challenges of multi-junction solar cells,” *Frontiers in Energy Research*, 2022.

[10] K. Ali, A. Khalid, M. R. Ahmad, H. M. Khan, I. Ali, and S. K. Sharma, “Multi-junction (iii–v) solar cells: From basics to advanced materials choices,” *Solar Cells*, 2020.

[11] S. E. T. Office, *Multijunction iii-v photovoltaics reseach*, U.S. Department of Energy.

[12] M. A. Green, “Thin-film solar cells: Review of materials, technologies, and commercial status,” *J. Mater Sci: Mater Electron*, 2007.

[13] Principle and application of solar PV cell, *Amorphous silicon thin film deposition technology*, 2022.

[14] A. Kojima, K. Teshima, Y. Shirai, and T. Miyasaka, “Organometal halide perovskites as visible-light sensitizers for photovoltaic cells,” *Journal of the American Chemical Society*, 2009.

[15] “Monocrystalline vs. polycrystalline solar panels (what’s best?) (2024),” EcoWatch. (2023).

[16] Z. Song, C. L. McElvany, A. B. Phillips, *et al.*, “A technoeconomic analysis of perovskite solar module manufacturing with low-cost materials and techniques,” *Energy & Environmental Science*, 2017.

[17] L. Meng, J. You, and Y. Yang, “Addressing the stability issue of perovskite solar cells for commercial applications,” *Nature Communications*, 2018.

[18] A. Baiju and M. Yarema, “Status and challenges of multi-junction solar cell technology,” *Frontiers in Energy Research*, 2022.

[19] K. Zweibel, “Thin film PV manufacturing: Materials costs and their optimization,” *Solar Energy Materials and Solar Cells*, 2000.

[20] I. Mathews, S. Sofia, E. Ma, *et al.*, “Economically sustainable growth of perovskite photovoltaics manufacturing,” *Joule*, 2020.

[21] J. M. Frost and A. Walsh, “Molecular motion and dynamic crystal structures of hybrid halide perovskites,” *Organic-Inorganic Halide Perovskite Photovoltaics*, 2016.

[22] C. Goehry, G. A. Nemnes, and A. Manolescu, “Collective behavior of molecular dipoles in ch3nh3pbi3,” *The Journal of Physical Chemistry C*, 2015.

[23] Y. Rakita, O. Bar-Elli, and E. Meirzadeh, “Tetragonal ch3nh3pbi3 is ferroelectric,” *Proceedings of the National Academy of Sciences*, 2017.

[24] A. Ndiaye, A. Charki, and A. Kobi, “Degradations of silicon photovoltaic modules: A literature review,” *Solar Energy*, 2013.

[25] J. Lindroos and H. Savin, “Review of light-induced degradation in crystalline solar cells,” *Solar Energy Materials and Solar Cells*, 2016.

[26] F. Kersten, P. Engelhart, and H.-C. Ploigt, “Degradation of multicrystalline silicon solar cells and modules after illumination at elevated temperature,” *Solar Energy Materials and Solar Cells*, 2015.

[27] D. Wang, M. Wright, N. K. Elumalai, and A. Uddin, “Stability of perovskite solar cells,” *Solar Energy Materials and Solar Cells*, vol. 147, pp. 255–275, 2016. DOI: `10.1016/j.solmat.2015.12.025`.

[28] J. J. Gutierrez-Sevillano, S. Ahmad, S. Calero, and J. A. Anta, “Molecular dynamics simulations of organohalide perovskite precursors: Solvent effects in the formation of perovskite solar cells,” *Physical Chemistry Chemical Physics*, 2015.

[29] T. L. Mitrana, R. E. Brophy, and et al., *Low-Dimensional Halide Perovskites: Structure, Synthesis, and Applications - 5. Ab Initio Studies*. Elsevier, 2021.

[30] L. Cojocaru, S. Uchida, Y. Sanehira, *et al.*, "Temperature effects on the photovoltaic performance of planar structure perovskite solar cells," *Chemistry Letters*, 2015.

[31] G. Divitini, S. Cacovich, F. Matteocci, *et al.*, "In situ observation of heat-induced degradation of perovskite solar cells," *European Microscopy Congress 2016: Proceedings*, 2016.

[32] C. Besleaga, L. E. Abramiuc, V. Stancu, *et al.*, "Iodine migration and degradation of perovskite solar cells enhanced by metallic electrodes," *J. Phys. Chem. Lett.*, 2016.

[33] E. Mosconi, D. Meggiolaro, H. J. Snaith, S. D. Stranks, and F. De Angelis, "Light-induced annihilation of frenkel defects in organo-lead halide perovskites," *Energy & Environmental Science*, 2016.

[34] C. Eames, J. M. Frost, P. R. F. Barnes, B. C. O'Regan, A. Walsh, and M. S. Islam, "Ionic transport in hybrid lead iodide perovskite solar cells," *Nature Communications*, 2015.

[35] G. A. Nemnes, C. Besleaga, V. Stancu, *et al.*, "Normal and inverted hysteresis in perovskite solar cells," *J. Phys. Chem. C*, 2017.

[36] G. A. Nemnes, C. Besleaga, A. G. Tomulescu, *et al.*, "Dynamic electrical behavior of halide perovskite based solar cells," *Sol. Energy Mater. Sol. Cells*, vol. 159, pp. 197–203, 2017.

[37] N. Filipoiu, A. T. Preda, D.-V. Anghel, *et al.*, "Capacitive and inductive effects in perovskite solar cells: The different roles of ionic current and ionic charge accumulation," *Phys. Rev. Appl.*, 2022.

[38] A. Mattoni, A. Filippetti, M. I. Saba, and P. Delugas, "Methylammonium rotational dynamics in lead halide perovskite by classical molecular dynamics: The role of temperature," *The Journal of Physical Chemistry C*, vol. 119, no. 30, pp. 17 421–17 428, 2015. DOI: `10.1021/acs.jpcc.5b04283`.

[39] D. Shakthivel, W. NAcaraj, S. Champet, D. H. Gregory, and R. Dahiya, "Propagation of amorphous oxide nanowires via the vls mechanism: Growth kinetics," *Nanosclae Advances*, 2019.

[40] C. HJ, *Vapor–Liquid–Solid Growth of Semiconductor Nanowires.* Springer, Berlin, Heidelberg, 2011.

[41] A. Solanki and H. Um, *Top-Down Etching of Si Nanowires*. Elsevier, 2018.

[42] A. N. Celik, B. Tuncel, N. Avishan, S. N. Shah, and N. Hussain, "Bottom-up and top-down strategies for fabrication of silicon nanowires," *Materials Innovations*, 2022.

[43] M. Kateb and K. Dehghani, "Comparison of fracture behavior of sharp with blunt crack tip in nanocrystalline materials by molecular dynamics simulation," *International Journal of Modern Physics: Conference Series*, vol. 5, pp. 410–417, 2012, ISSN: 2010-1945.

[44] T. Schlick, *Molecular Modeling and Simulation: An Interdisciplinary Guide*. Springer, 2010.

[45] A. P. Thompson, H. M. Aktulga, R. Berger, *et al.*, "'lammps' - a flexible simulation tool for particle-based materials modeling at the atomic, meso, and continuum scales," *Comp. Phys. Comm.*, 2022.

[46] I. R. McNab, "Rotational spectroscopy, theory," in *Encyclopedia of Spectroscopy and Spectrometry*, J. C. Lindon, G. E. Tranter, and D. W. Koppenaal, Eds., 2017.

[47] A. Mattoni, A. Filippetti, and C. Caddeo, "Modeling hybrid perovskites by molecular dynamics," *Journal of Physics: Condensed Matter*, 2016.

[48] R. Iftimie, P. Minary, and M. E. Tuckerman, "Ab initio molecular dynamics: Concepts, recent developments, and future trends," *Proceedings of the National Academy of Sciences*, 2005.

[49] C. I. Bayly, P. Cieplak, W. Cornell, and P. A. Kollman, "A well-behaved electrostatic potential based method using charge restraints for deriving atomic charges: The resp model," *The Journal of Physical Chemistry*, 1993.

[50] A. Jakalian, B. L. Bush, D. B. Jack, and C. I. Bayly, "Fast, efficient generation of high-quality atomic charges. am1-bcc model: I. method," *Journal of computational chemistry*, 2000.

[51] A. Jakalian, D. B. Jack, and C. I. Bayly, "Fast, efficient generation of high-quality atomic charges. am1-bcc model: Ii. parameterization and validation," *Journal of computational chemistry*, 2002.

[52] R. Brophy, "Computer simulations of ionic diffusion," M.S. thesis, Reykjavík Univeristy, 2021.

[53] G. Lui, L. Kong, and J. Gong, "Pressure-induced bandgap optimization in lead-based perovskite with prolonged carrier lifetime and ambient retainability," *Advanced Functional Materials*, 2017.

[54] A. Jaffe and Y. Lin, "Halide perovskite under pressure: Accessing new properties through lattice compression," *ACS Energy Letters*, 2017.

[55] C. Peng, J. Chen, H. Wang, and P. Hu, "First-principles insight into the degradation mechanism of ch3nh3pbi3 perovskite: Light-induced defect formation and water dissociation," *The Journal of Physical Chemistry C*, 2018.

[56] R. Brophy, M. Keteb, and I.-M. Ghitiu, "Oh− ions can reduce the iodide migration in mapi," *International Semiconductor Conference (CAS)*, 2023.

[57] S. Mariotti and M. A. Turkestani, "Direct silicon heterostructures with methylammonium lead iodide perovskite for photovoltaic applications," *IEEE Journal of Photovoltaics*, 2020.

[58] X. Wang, C. Tang, J. Yang, and D. Y. snd Wenli Lv, *NAnotechnology 35 495201*, 2024.

[59] A. Sitek, L. Serra, V. Gudmundsson, and A. Manolescu, "Electron localization and optical absorption of polygonal quantum rings," *Phys. Rev. B*, 2015.

[60] A. Sitek, M. Urbaneja Torres, K. Torfason, V. Gudmundsson, A. Bertoni, and A. Manolescu, "Excitons in core–shell nanowires with polygonal cross sections," *Nano Letters*, 2018.

[61] H. In, C. Field, and P. E. Pehrsson, "Periodically porous top electrodes on vertical nanowire arrays for highly sensitive gas detection," *Nanotechnology*, 2011.

[62] K. Y. J. and M. A., "Porous si nanowires for highly selective room-temperature no2 gas sensing," *Nanotechnology*, 2018.

[63] Q. Y., J. Y., and Z. L, "Enhanced humidity resistance of porous sinws via ots functionalization for rarefied no2 detection," *Sensors and Actuators B: Chemical*, 2019.

[64] R. Ghosh, M. S. Song, J. Park, *et al.*, "Fabrication of piezoresistive si nanorod-based pressure sensor arrays: A promising candidate for portable breath monitoring devices," *Nano Energy*, vol. 80, p. 105 537, 2021, ISSN: 2211-2855. DOI: `https://doi.org/10.1016/j.nanoen.2020.105537`. [Online]. Available: `https://www.sciencedirect.com/science/article/pii/S2211285520311113`.

[65] E. Fakhri, M. T. Sultan, A. Manolescu, S. Ingvarsson, and H. G. Svavarsson, "Application of p and n-type silicon nanowires as human respiratory sensing device," *Sensors*, vol. 23, no. 24, 2023, ISSN: 1424-8220. DOI: `10.3390/s23249901`. [Online]. Available: `https://www.mdpi.com/1424-8220/23/24/9901`.

Appendix A

Code

You can put code in your document using the `listings` package, which is loaded. Be aware that the `listings` package does not put code in your document if you are in draft mode unless you give it the `final` option.

There is an example java (Listing A.1) and XML file (Listing A.2). Thanks to the `url` package, you can typeset OSX and unix paths like this: `/afs/rnd.ru.is/project/thesis-template`. Windows paths: `C:\windows\temp\` . Note: The `menukey` package has similar functionality but may cause problems.

If you are trying to include multiple different languages, you should go read the documentation and set these up as below. You will save yourself a lot of effort, especially if you have to fix anything.

Listing A.1: Data_Bus.java: Setting up the class.

```
package com.example.mycoolapp;

import android.app.Activity;
import android.content.Intent;
import android.os.Bundle;
import android.view.View;
import android.widget.Button;
import android.widget.TextView;

// I am creating a comment that is very very long to demonstrate how the line ↩
    ↪wrapping system works. You should see a symbol to annotate that it has ↩
    ↪been wrapped to the next line.
public class Data_Bus extends Activity {
    Button Next;
    TextView textdisplay1, textdisplay2;
```

```
    @Override
    protected void onCreate(Bundle savedInstanceState) {
        // TODO Auto−generated method stub
        super.onCreate(savedInstanceState);
        setContentView(R.layout.adc_databustest);
        Next = (Button) findViewById (R.id.checkButton);
        textdisplay1 = (TextView) findViewById (R.id.tvTop);
        textdisplay2 = (TextView) findViewById (R.id.tvBottom);

    }
}
```

Listing A.2: AndroidManifest.xml: Configuration for the Android UI.

```
<?xml version="1.0" encoding="utf−8"?>
<manifest xmlns:android="http://schemas.android.com/apk/res/android"
    package="com.example.mycoolapp"
    android:versionCode="1"
    android:versionName="1.0" >

    <uses−sdk
        android:minSdkVersion="13"
        android:targetSdkVersion="13" />

    <application
        android:allowBackup="true"
        android:icon="@drawable/ic_launcher"
        android:label="@string/app_name"
        android:theme="@style/AppTheme" >

        <activity
            android:name=".MainActivity"
            android:label="@string/app_name" >
            <intent−filter>
```